Nonlinear Integrated Photonics in the Visible Spectrum

Based on III-N Material Platform

by

Hong Chen

A Dissertation Presented in Partial Fulfillment
of the Requirements for the Degree
Doctor of Philosophy

Approved May 2020 by the
Graduate Supervisory Committee:

Yuji Zhao, Chair
Yu Yao
Liping Wang
Cun-Zheng Ning

ARIZONA STATE UNIVERSITY

August 2020

ABSTRACT

Photonic integrated circuit (PIC) in the visible spectrum opens up new opportunities for frequency metrology, neurophotonics, and quantum technologies. Group III nitride (III-N) compound semiconductor is a new emerging material platform for PIC in visible spectrum. The ultra-wide bandgap of aluminum nitride (AlN) allows broadband transparency. The high quantum efficiency of indium gallium nitride (InGaN) quantum well is the major enabler for solid-state lighting and provides the opportunities for active photonic integration. Additionally, the two-dimensional electron gas induced by spontaneous and polarization charges within III-N materials exhibit large electron mobility, which is promising for the development of high frequency transistors. Moreover, the noncentrosymmetric crystalline structure gives nonzero second order susceptibility, beneficial for the application of second harmonic generation and entangled photon generation in nonlinear and quantum optical technologies. Despite the promising features of III-N materials, the investigations on the III-N based PICs are still primitive, mainly due to the difficulties in material growth and the lack of knowledge on fundamental material parameters. In this work, firstly, the fundamental nonlinear optical properties of III-N materials will be characterized. Then, the fabrication process flow of III-N materials will be established. Thirdly, the waveguide performance will be theoretically and experimentally evaluated. At last, the supercontinuum generation from visible to infrared will be demonstrated by utilizing soliton dynamics in high order guided modes. The outcome from this work paves the way towards fully integrated optical comb in UV and visible spectrum.

DEDICATION

This work is dedicated to my parents, my fiancée Wenyi Gu, and her parents.

ACKNOWLEDGMENTS

It's really a great pleasure to work on my project under the advisory of Professor Zhao in the past 5 years. Prof. Zhao provides me the opportunities to pursue interesting topics and guided me navigating the world of III-N. Without his knowledge, inspiration, education, and support, it's impossible to finish this thesis. I also need to acknowledge to my committee members: Prof. Yu Yao, Prof. Liping Wang, and Prof. Cun-Zheng Ning, for their helpful suggestions during my research.

I also need to thank colleagues for their assistance during this project: Dr.Houqiang Fu, Dr. Zhijian Lv, Dr. Xuanqi Huang, Xiaodong Zhang, Jossue Montes, Tsung-Han Yang, Dr. Kai Fu, Chen Yang, Jingan Zhou, Xuguang Deng and Xin Qi. And many of my friend in my homeland for their emotional support: Sidong Fu, Jian Wen, and Dr. Shi Chen.

The fabrication processes were performed within ASU nanoFab facilities and received a great help from all staff members. Dr. Shirong Zhao and Dr. Wenwen Li kindly shared their knowledge on device fabrications in the initial stage of this research.

The initial testing of optical device was performed within the ASU ultra-fast laser facilities lead by Dr. Su Lin and Dr. Doulas Daniel. Many thanks to them for the helpful suggestions on instrumental setups. Late devices of this research were characterized in Prof. Cun-Zheng Ning's nanophotonics lab, and I do received great help from Prof. Ning's PhD student Dongying Li.

Without the help from Dr. Karl Weiss, the polishing of sapphire would take me forever. I need to greatly acknowledge the ASU Eyring Materials Center for the sample preparation.

Finally, I would like to thank our sponsor, Army Research Office, and the program manager Dr. Michael Gerhold for the support.

TABLE OF CONTENTS

Page

CHAPTER Page

LIST OF TABLES

Table Page

LIST OF FIGURES

Figure Page

Figure Page

Figure Page

CHAPTER 1

INTRODUCTION

1.1 III-nitrides and integrated optics

III-nitride semiconductors including AlN, GaN, InN and their alloys have enabled a wide variety of opto-electronic applications [1-5]. The highly efficient light emitting properties of GaN/InGaN materials have attracted numerous of research efforts and have entry into the mass market of solid-state lighting [6]. By choosing the proper crystal planes of wurtzite GaN, namely the polar, nonpolar, and semipolar planes, the internal quantum efficiency of InGaN quantum wells (QWs) can be further increased, which leads to the development of low-droop blue/green LEDs [2] and green lasers [4]. Besides the light-emitting devices, III-N materials are also considered as a strong candidate in the applications of power electronics [7], RF amplifiers [3], photo-detectors [5], communication [8], and photovoltaics [9].

One of the III-N based applications that haven't been comprehensively investigated is the photonic integration within visible spectrum. The nitrogen-vacancy (N-V) centers within diamond has been widely exploited as single photon emitter [10,11] for the investigations on quantum optical technologies, and the emission wavelength of N-V center is 637 nm within the visible spectrum [11]. Furthermore, the autonomous driving relies on optical hardware that can actively steer the beam in the far-field and reconstruct the space information, and the typical operation wavelengths are in the infrared (IR). While for the submarine scenario, IR light exhibits strong decay and the visible light provides long travel distance [12], which is promising for submarine 3D sensing applications.

Moreover, recent advances on biological science opens up new opportunities in the optogenetics, which provides a flexible way to control neurons [13]. To realize the aforementioned potential applications, photonic integrated micro systems operating in visible spectrum are of high demand.

In this research, we explore the possibility of utilizing the III-N materials for photonic integration, especially for the applications within the visible spectrum. As shown in the Figure 1-1 [14], the bandgap energy of III-N materials covered a wide range of photon energies from deep UV to infrared.

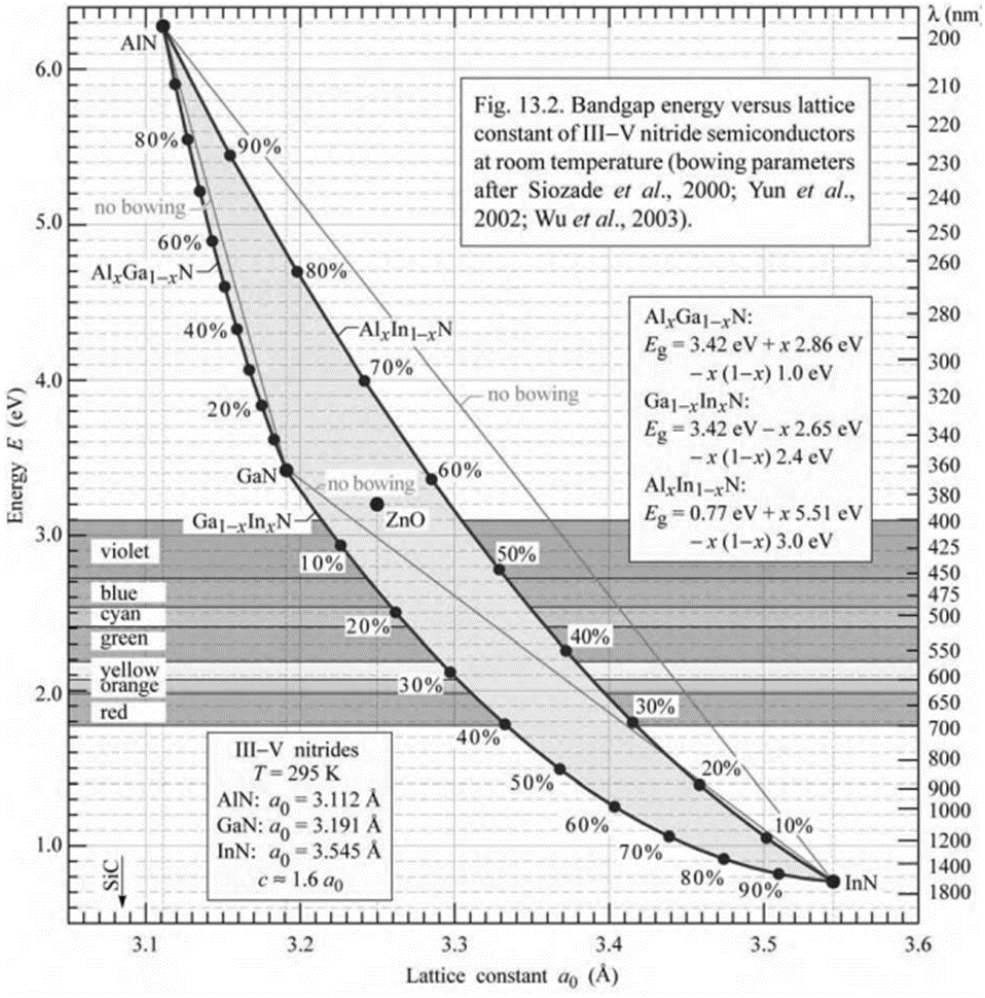

Figure 1-1. Bandgap energy of III-N materials versus lattice constant. Plot adapted from [14].

In addition to the wide tunability of bandgap energies, the III-N semiconductors and their alloys also possess devices of different functionalities, this is promising for system level integration: AlN and GaN possess broadband transparency due to their relative large bandgap energies [15,16], which is beneficial for low loss wave guiding. The ultra-wide bandgap of AlN also provides low material dispersion, its noncentrosymmetric crystalline structure provides non-zero second order susceptibility $^{(2)}$, those are advantageous for nonlinear optical applications. The Al_xGa_yN exhibits spontaneous and polarization charge [17] in its AlGaN/GaN heterostructures, where two-dimensional electron gases (2DEG) are induced. The high mobility of 2DEG enabled high performance RF transistors and can be actively integrated into the photonic system for frequency/phase locking [18,19]. Successful developments on InGaN based visible LEDs and lasers also provides capabilities on active integration. The several potential applications via III-N platform are shown in Figure 1-2.

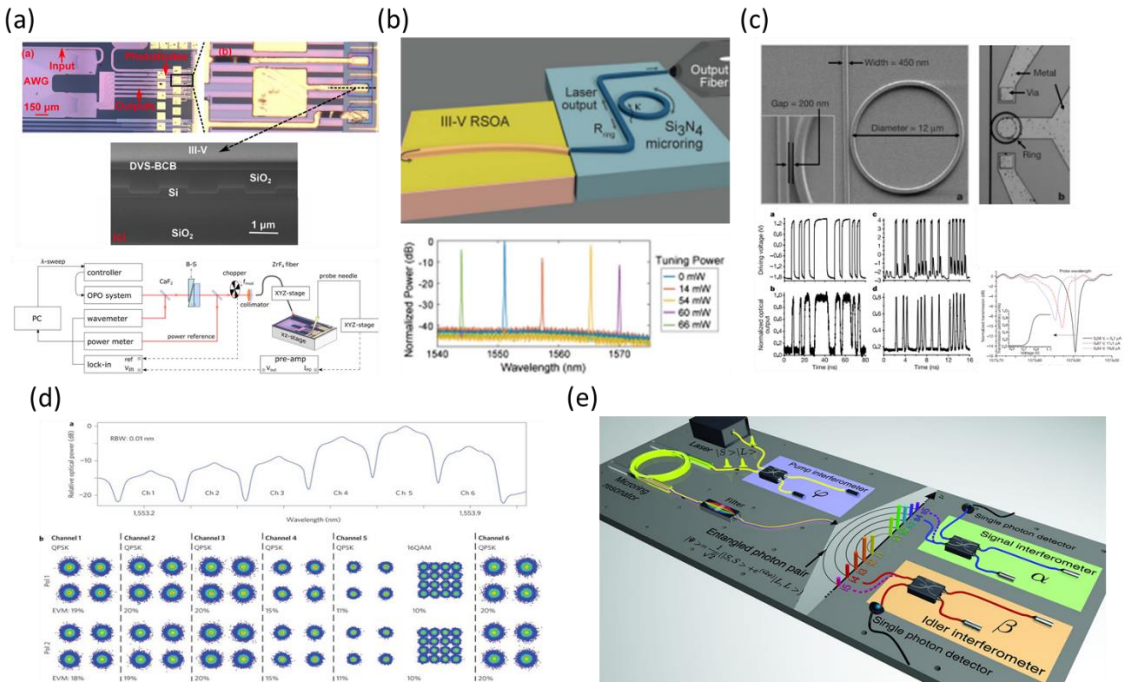

Figure 1-2. Potential applications using III-N material platform. (a) Integrated spectrometer [20]. (b) Narrow linewidth tunable lasers [21]. (c) Modulators [22]. (d) On-chip high speed interconnections [23]. (e) Generation of entangled quantum states [24].

Although the III-N material system is beneficial for visible spectrum integrated optics, the investigations on this topic still remains on a preliminary stage, and it's very challenging in leveraging all electro-optical parts (lasers, detectors, transistors, modulators, etc) into one chip. A good starting point would be the investigations on passive components and play with the physics of nonlinear optics and keep the lasers and detectors off-chip to reduce the complexity of system. In visible spectrum, due to the large photon energy, strong material dispersion is expected, which leads to normal group velocity dispersion (GVD). It is this normal GVD that hindered the development of Kerr frequency comb within visible spectrum. The goal of this thesis is to figure out the way for dispersion management in this highly dispersive spectrum (UV-visible spectrum), by which the optical frequencies can be coherently transferred through IR/near-visible to UV/visible. It should be noted that the

methods demonstrated in this research is not only limited in dispersion management but also in material characterization, device layout/fabrication, and optical testing, so that the outcome of this research could potentially be beneficial to nonlinear optics, photonic integration, and III-N material sciences.

1.2 Review of integrated optics in the visible spectrum

As we mentioned in the previous section, the research interests on integrated optics within visible spectrum still remains on very preliminary stage, and the research efforts are mainly focusing on the developing of low loss waveguides [25,26] or high quality-factor resonators [26,27]. Other developments on this topics are mainly focusing on the nonlinear optical applications such as second harmonic generation (SHG), third harmonic generation (THG), parametric up/down conversion, supercontinuum generation (SCG), and frequency comb generation.

For the development of low loss waveguides, diverse of materials are being investigated: Cavin West et al. demonstrated low loss platform based on atomic layer deposition (ALD) aluminum oxide, the waveguide exhibit propagation loss less than 3 dB/cm at the wavelength of 371 nm [26]. Wesley Sacher et al. developed the silicon nitride waveguides with single mode propagation loss below 2.8 dB/cm and 1.9 dB/cm in the wavelength ranges of 466-550 nm and 552-648 nm, respectively, the platform was adopted for implantable neuronphotonic probes [25]. The development on AlN microrings by Xianwen Liu et al. has achieved a high quality factor of 2.1×10^5 at 390 nm, which corresponds to the optical loss ~8 dB/cm [27]. Some recent preliminary investigations on beta-phase gallium oxide based waveguides also gives promising results of 3.76 dB/cm at

the wavelength of 810 nm [28]. It's worth noting that all material platforms exhibit their own "Pros." and "Cons.". The aluminum oxide waveguide exhibit extreme low loss in the UV spectrum, while the weak confinement hindered its application in nonlinear optics, where moderate modal confinement are required to compensate material dispersion. Silicon nitride waveguides possess excellent compatibility with CMOS technologies while the lack of $^{(2)}$ nonlinearity and the material damage under UV illumination [29] place the major drawbacks to this platform. AlN exhibit excellent compatibility with III-N material system and possess nonzero $\chi^{(2)}$ nonlinearity, however, due to the lattice mismatch during epitaxial growth on foreign substrate, large density of threading dislocations are observed, which also degrade the performance in short wavelengths.

While for the nonlinear optical applications, initial investigations were focusing on second harmonic generations from IR to near-visible using GaN [30] and AlN [31], further investigations demonstrate frequency combs within visible spectrum mainly via phase matched second harmonic and third harmonic frequency conversion [32,33]. To overcome the huge material dispersion in visible spectrum, the soliton dynamics has emerged as a new method for coherent generation in short wavelengths [34-36], by which frequency comb was achieved in the UV spectrum from ridge silica waveguide. Alternatively, recent development of periodically tapered waveguides achieved relative broad phase match within UV spectrum [37], and the frequency comb was achieved via $^{(2)}$ process.

This thesis contributes the previously mentioned researches in the followed aspects. First, the fundamental nonlinear optical properties (two photon absorption coefficient, Kerr nonlinear refractive index) of several emerging materials (GaN, beta-phase gallium oxide) are characterized in this research. The fabrication processes for GaN and AlN were also

established and shared to the community. In order to achieve coherent generation, the solitons were intentionally launched into the high order guided mode, by properly engineering the GVD and high order dispersions, soliton fission is achieved from near visible to visible spectrum with record low pulse energy required. This is controversial to the "common sense" as usually the high order modes are accompanied with strong loss and would degrade the nonlinear conversion efficiency. The findings obtained within this research paves the way towards chip integrated UV-visible frequency combs based on III-N.

1.3 Structure of this thesis

In this thesis, we perform comprehensive investigations on the III-N materials as a photonic integrated circuit (PIC) platform for nonlinear optical applications in the visible spectrum. Part of this thesis has been previously published in several journals [38-42].

In Chapter 2, we show the experimental characterizations on the nonlinear optical properties of GaN, beta-phase gallium oxide, and gives theoretical predictions on the nonlinear optical properties of AlN. Those physical parameters will be served as fundamental knowledge for the rest of this thesis.

In Chapter 3, we experimentally investigated and optimized the fabrication processes of GaN/AlN waveguides. The processes developed within this Chapter is used throughout the rest of this thesis. Customized lithography/deposition/etching/polishing recipes are provided for reference.

In Chapter 4, waveguide performances are evaluated both theoretically and experimentally. The theoretical calculation predicts that the free carrier loss within GaN

waveguides is the major limiting factor in achieving high quality resonators, while the large two photon absorption coefficient also hindered its usage in high optical power scenario. AlN does not exhibit n-type conductivity, which result in excellent waveguide performance and lead to high quality factor of resonators. Our micro-photonic waveguides exhibit less than 2 dB/cm propagation loss at 800 nm. The intrinsic *Q* factor of GaN micro-disk resonators were characterized to be on order of 10^4, and the intrinsic *Q* of AlN micro-ring resonator were identified to be on order of 10^5 (approaching 10^6). Those results agree well with theoretical predictions.

In Chapter 5, we firstly present our observations of nonlinear phenomenon within III-N waveguides. By properly manage the dispersion profiles of AlN waveguide, supercontinuum generation via soliton dynamics within high order guided mode can be achieved, and the generated dispersive wave was located in the green region. Simulation further reveals the physical insight and predicts the good coherence. Further optimizations on the dispersive wave generation employees the periodically modulated waveguide, by which quasi-phase match can potentially be achieved. Second harmonic generation from AlN waveguide was also investigated within this Chapter.

Finally, we conclude in Chapter 6, and provide future directions including auto-correlators and high quality factor UV resonators.

In addition to the main contents, an Appendix is attached at the end of this thesis. It includes basic Matlab codes used in this research.

CHAPTER 2

CHARACTERIZATIONS ON THE NONLINER OPTICAL PROPERTIES OF III-N

2.1. A brief introduction on the Z-scan method

The cubic nonlinearity of semiconductor materials plays an important role in a wide variety of nonlinear processes such as soliton dynamics [34-36], four-wave mixing [43], and self-steepening [44]. The cubic nonlinearities are usually identified in the form of Kerr nonlinear refractive index (n_{kerr}) and two photon absorption (TPA) coefficients using Z-scan method as proposed by M. Sheik-Bahae et al. [45]. The Z-scan setup is analogous to typical transmission measurements and the setup schematic is shown in Fig. 2-1. Light sources used in this research is Ti:Sapphire laser operating near the wavelength of 800 nm. The $\chi^{(2)}$ crystal was utilized for characterizations near 400 nm wavelengths. Input optical power and polarization of the beam were controlled by the attenuator and half-wavelength plate, respectively. Beam waist of the initial Gaussian beam was expanded by lenses L1 and L2 before launching into objectives to minimize the focused beam size. The transmitted optical power is collected by lens L3 and measured by power meter after an aperture. The sample under measurement is scanning along the beam propagation direction (z-direction), and the transmitted power was recorded at different sample location.

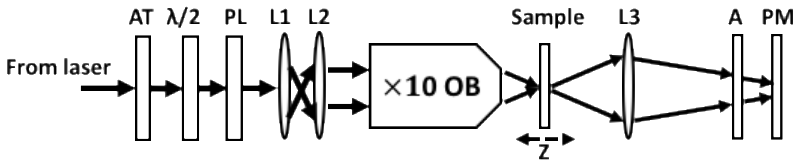

Figure 2-1. Typical Z-scan setup used in this research. AT: attenuator. λ/2: half-wavelength plate. PL: polarizer. OB: optical objective lens. A: aperture. PM: power meter. L1, L2, L3: lenses.

Since the Gaussian beam is tightly focused. Maximum power density is achieved at focal point, where the nonlinear response of material is maximized. For the characterization on TPA, aperture maintains open thus 100% of transmitted light is collected by power meter. Since the absorption is proportional to optical power density, a dip at focal point is expected during the scan as shown in Fig. 2-2(a). This is the so-called open aperture scan. For the characterization on Kerr nonlinear refractive index, the aperture is partially closed and only allows 20%-40% of light collected. Since the Kerr effect is influential to the refractive index of material, self-focusing or self-defocusing of the Gaussian beam is expected [45], by which the transmission exhibits maximum/minimum before or after the focal point as shown in Figs. 2-2(b) and 2-2(c). This is called closed aperture scan. It's also worth noting that some other physical processes may also impact the transmission such as saturated free carrier absorption [46] and three-photon absorption [47], advanced modified models that taking those processes into account is studied in [47].

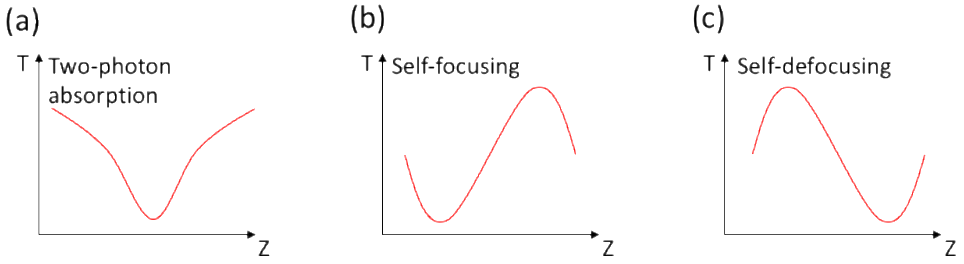

Figure 2-2. Signatures of some typical nonlinear processes that may happen during the scan of sample along Z-direction. (a) Two photon absorption (b) Kerr effect induced self-focusing (c) Kerr effect induced self-defocusing.

After obtaining the transmission, fittings can be applied to both open and closed aperture scanned transmissions. The open aperture scanning curve should be fitted by the followed equation:

$$T \approx 1 - \frac{\beta I_0 L_{eff}}{2\sqrt{2}} \times \frac{1}{1 + Z^2/Z_0^2} \tag{2-1a}$$

$$Z_0 = \frac{n\pi\omega_0^2}{\lambda} \tag{2-1b}$$

where T is the normalized transmission, I_0 is the peak beam power density, L_{eff} is the effective sample length, Z_0 is the Rayleigh range of the beam, n is the refractive index, ω_0 is the beam size at the focal plane, and λ is the wavelength. L is the sample thickness. And the transmission differences of peak and valley during closed aperture scanning follows:

$$\Delta T_{p-v} \approx 0.406(1 - S)^{0.25}|\Delta\phi_0| \tag{2-2}$$

where S indicates percentage of light that propagates through aperture, $\Delta\phi_0$ the phase change of light due to Kerr effect, ΔT_{p-v} is the peak and valley transmission difference. The Rayleigh range obtained from Eqs. (2-1a) and (2-1b) is lined to the peak-valley distance obtained in Eq. (2-2) by the followed equation:

$$Z_{pv} \approx 1.7Z_0 \tag{2-3}$$

In reality, it's impractical that measures the nonlinear of materials in all wavelengths/frequencies. M. Sheik-Bahae et al. provide a reliable estimation on the TPA

coefficient [48] using two band theory. The photon energy dependence of TPA coefficient is

$$\beta(\omega) = K\frac{\sqrt{E_p}}{n_0^2 E_g^3} F_2\left(\frac{\hbar\omega}{E_g}\right) \tag{2-4}$$

in which K is material related constant, n_0 is the refractive index, $E_p = 2|P_{vc}|^2/m_0$, obtained by the $k \cdot p$ model, which is a material-independent parameter for direct bandgap semiconductors, Eg is the bandgap energy, F_2 is the fitting function with the form of $F_2(x) = (2x-1)^{1.5}/(2x)^5$ that is invariant to material properties [48], ω is the angular frequency that of interest.

The wavelength dependence of Kerr nonlinear refractive index can be further obtained by applying Kramers-Kronig integral (K-K integral) and treating the TPA as perturbation to the imaginary part of refractive index [48].

$$\Delta n(\omega; P) = \frac{c}{\pi}\int_0^\infty \frac{\Delta\alpha(\omega'; P)}{\omega'^2 - \omega^2} d\omega' \tag{2-5}$$

Equations (3-4) and (3-5) provide good estimations on the nonlinear parameters in all wavelengths within the optical frequency.

2.2 Experimental characterization on GaN

Recent studies on III-nitride based waveguides have opened new opportunities due to their wide bandgap, low material dispersion, and active integration capability [49], which are particularly attractive for applications in nonlinear optics [35-37,43]. Despite their importance, there have been only very few reports on the basic nonlinear properties

of III-nitride materials, e.g., the two photon absorption (TPA) coefficient (β), Kerr refractive index (n_{kerr}), and three photon absorption (3PA) coefficient (γ) [50-53]. Sun *et al.* studied TPA coefficients above half-bandgap photon energy for polar *c*-plane GaN, where the TPA coefficients β were reported to be 17 ± 7 and 14 ± 6 cm/GW at 387 and 391 nm, respectively, and 3 ± 1.5 and 7 ± 3 cm/GW at 720 and 690 nm, respectively [50]. Furthermore, Fang *et al.* showed $n_{kerr} = 1.15 \times 10^{-14}$ cm^2/W ($E \perp c$) and 1.4×10^{-14} cm^2/W ($E \parallel c$) at 800 nm for *c*-plane bulk GaN [53]. These results, however, have been almost exclusively focused on conventional polar *c*-plane III-nitrides. Recent advances on hydride vapor phase epitaxy (HVPE) growth of GaN brings significant reduction on threading dislocations, which in turn results in different material properties comparing with the characterizations in early days. Additionally, a new class of III-nitride materials, namely nonpolar and semipolar III-nitrides, have emerged with very different material and optical properties, leading to distinct device performance for light-emitting devices and solar cells [2,9]. In this section, we perform a comprehensive characterization on the TPA coefficient β, n_{kerr}, and 3PA coefficient γ, for bulk GaN in polar, nonpolar, and semipolar orientations, which have never been fully studied.

Commercial double polished bulk GaN substrates on polar *c*-plane, nonpolar *m*-plane, and semipolar $(20\overline{2}1)$ plane were used for the study. The substrates were grown using HVPE method with dislocation density in the range of 2×10^5-2×10^6 cm^{-2}. A typical Z-scan method [45] was used for the optical characterization and the schematic of the setup is similar to that shown in Fig. 2-1. A femtosecond Ti:Sapphire laser was tuned from 724 nm to 840 nm in the femtosecond pulsed mode, and the typical spectrum of the laser used in this research is shown in Fig. 2-3(a). The light beam was focused using a $\times 20$

microscope objective, and the Rayleigh range and beam size were extracted from the fitting of experimental data [shown in Fig. 2-3(b)] using Eqs. (2-1a) and (2-1b).

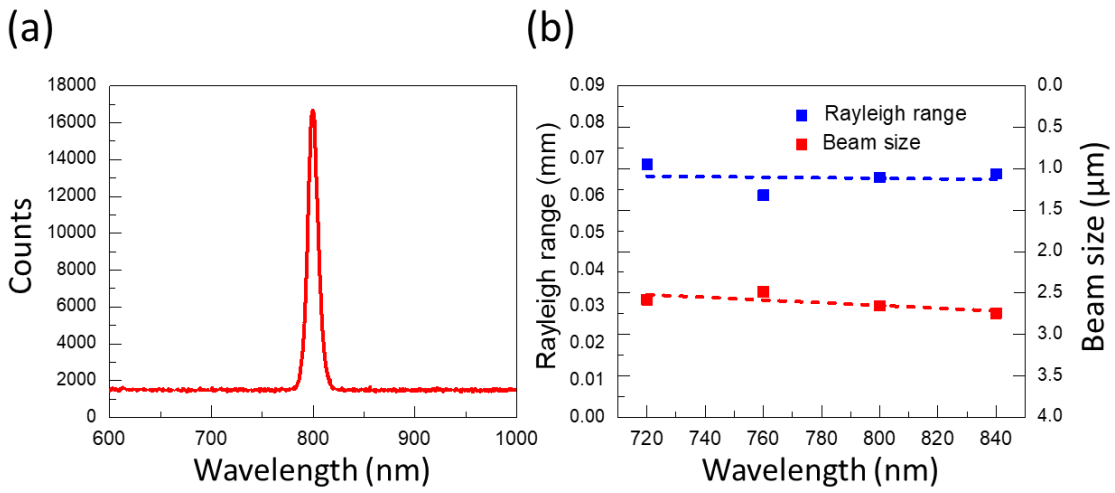

Figure 2-3. (a) Typical output spectrum of Ti:S laser (b) The measured Rayleigh range and beam size at different wavelengths.

The effective sample thickness in this work is 500 μm. The samples are sufficiently thick such that the Fabry–Pérot(FP) resonance does not influence the results. Fig. 2-3(b) shows the Rayleigh range and the beam size vs. wavelength for the measurement where the Rayleigh range remains constant within the spectrum, which indicates invariant beam size during the measurement. For the open aperture measurement, all of the lights were collected by the power meter. For the closed aperture measurement, the aperture was tuned to allow 36% of the total power to pass through. The output power of the laser was kept stable in pulsed mode, therefore a feedback loop was not required in this experiment to stabilize the incident power. It's worth noting that since unintentionally doped GaN possess *n*-type conductivity [54] with free carrier concentration around 10^{17} cm^{-3}, using the analytical Drude model [55], the free carrier absorption at this carrier density is estimated to be ~0.09 dB/cm at 800 nm, indicating ~0.25% total optical power loss when propagating

through the GaN slab. This loss is relative small comparing with multi-photon absorption induced optical loss shown in this work.

Figures 2-4(a) to 2-4(c) show the open aperture and closed aperture plots for samples on polar *c*-plane, nonpolar *m*-plane, and semipolar $(20\overline{2}\overline{1})$ plane, respectively. The peak beam power density was kept around 9 GW/cm^2. For the characterization on the *m*- and $(20\overline{2}\overline{1})$-plane GaN, light is polarized along the *c* (E ∥ *c*) and $[1\overline{2}1\overline{4}]$ (*c* projection, E ∥ c') direction, respectively, while for *c*-plane, light is polarized on *m* axis (E ∥ *m*). For photons with energy larger than half bandgap, the TPA process was considered when fitting the open aperture curve. While for photons with energy lower than half bandgap, the 3PA process was considered. The fitting results agree sufficiently well with the experimental data.

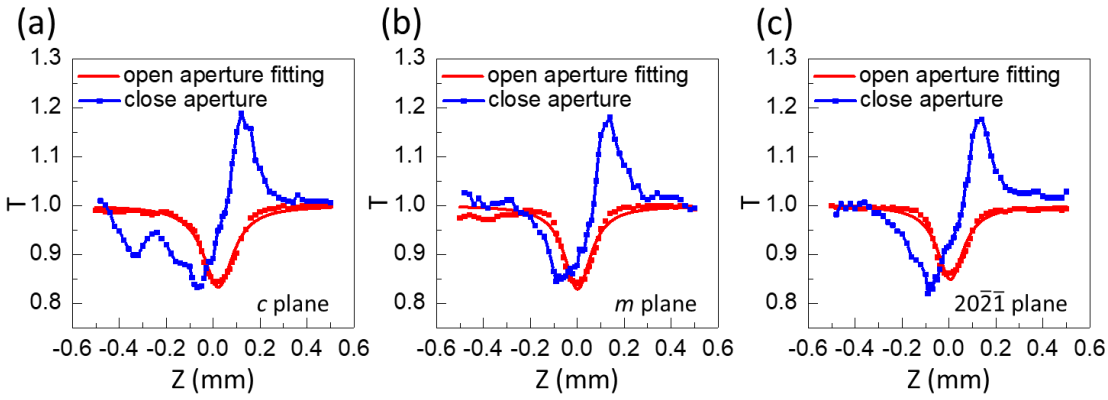

Figure 2-4. The open aperture and closed aperture plots for samples on (a) polar *c*-plane, (b) nonpolar *m*-plane, and (c) semipolar $(20\overline{2}\overline{1})$ plane. The results were measured at 724 nm incident light.

Figure 2-5(a) shows the TPA coefficient β vs. wavelength, where experimental results from previous studies were also plotted for comparison. The theoretical model developed by Sheik-Bahaewas as given in Eq. (2-4) was used to obtain the wavelength dependence [45]. The β obtained from this study agrees well with the theoretical fitting

and shows a consistent trend with the previous experimental results. The 3PA coefficient γ was estimated using the equation $\Delta\alpha = \gamma I_0^2$, and the results are summarized in Table 2-1.

Table 2-1. The three-photon absorption coefficient obtained in this research

Wavelength (nm)	Three-photon absorption coefficient γ (10^{-3} cm^3/GW^2)		
	c-plane	*m*-plane	$(20\overline{2}1)$-plane
740	7.60	8.09	8.04
760	4.58	4.47	4.46
840	2.10	2.48	2.48

The value of β of GaN we obtained in this work is found to be smaller than early characterizations [50], which can be attributed to reduced threading dislocation density. The relative low TPA coefficients make the III-nitride a very attractive material system for the fabrication of high quality second harmonic generators or entangled photon pair generators in the visible or even UV regions. Using the TPA and three-photon absorption coefficients obtained above, we can briefly evaluate the performance of GaN waveguide for nonlinear optics applications. For example, for a GaN waveguide with a mode area of 1 um^2, if the optical power inside the waveguide is 1 mW, considering the CW operation condition, the nonlinear loss contributed from TPA will be ~0.0004 dB/cm at 724 nm. If the optical power inside the waveguide is 100 mW, the nonlinear loss for the GaN waveguide will be ~0.04 dB/cm. Therefore, GaN is potentially promising for the fabrication of low loss waveguide in the near-infrared and visible spectrum region. With even higher bandgap photon energy, better performance can be expected on AlN waveguides.

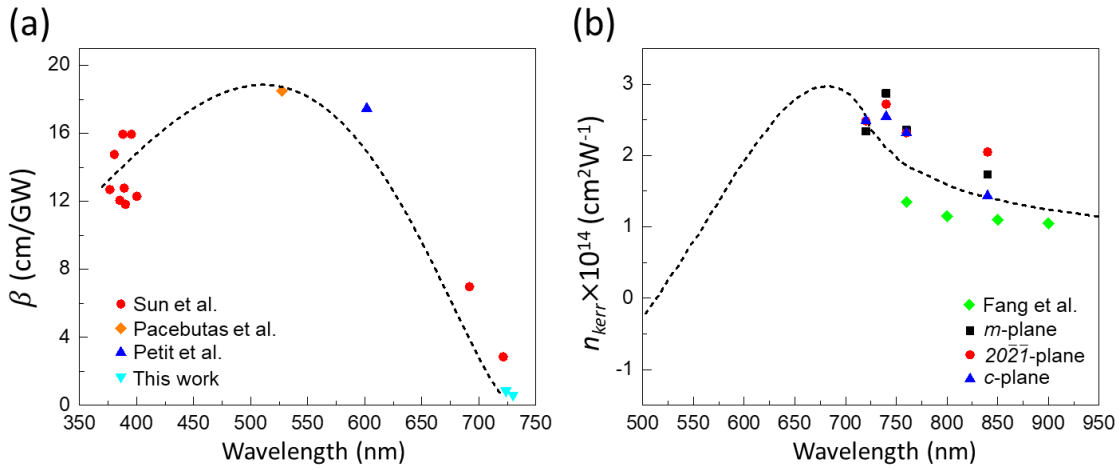

Figure 2-5. The measured TPA coefficient and Kerr nonlinear refractive index and their estimated wavelength dependence (dash line).

Finally, we also extracted the Kerr refractive index n_{kerr} from closed aperture measurement, and the results are shown in Fig. 2-5(b). n_{kerr} was identified to be ~2.50 × 10^{-14} cm^2/W for all three samples on polar, nonpolar, and semipolar orientations. In previous studies, self-defocusing due to two-photon absorption and the quadratic stark effect were observed in GaN at visible and near-UV region [51,56]. In this study, however, a positive phase shift is observed, which is predicted in [54] and recently also observed in [53]. The high n_{kerr} obtained in this work combined with the low β value makes GaN material a promising candidate for the fabrication of all optical bistable switching waveguides [57].

In a short summary, within this section, we studied the basic nonlinear optical properties including TPA, 3PA, and Kerr refractive index for GaN on polar *c*-plane, nonpolar *m*-plane, and semipolar (20 $\overline{21}$) plane bulk GaN crystals. No significant differences were observed for samples on these three orientations. Low TPA coefficients β (~0.90 cm/GW at 724 nm and 0.65 cm/GW at 730 nm) were observed for GaN samples,

which leads to very low nonlinear loss for GaN waveguide devices. For the Kerr refractive index, n_{kerr}~2.50× 10^{-14} cm^2/W was observed at 724 nm for all three samples. The results obtained in this work provide valuable information for the fabrication of high performance low loss GaN photonic devices and integrated photonic circuits, especially for the study of nonlinear processes inside high quality factor resonating structures (e.g., ring resonators, disk resonators).

2.3 Experimental characterization on beta-phase gallium oxide

Beta-phase gallium oxide (β-Ga_2O_3) is another emerging wide bandgap semiconductor material [58]. Due to its wide bandgap, β-Ga_2O_3 possesses a board transparent spectrum from UV to visible wavelength. Moreover, β-Ga_2O_3 is compatible with III-N material system [59]. It indicates that the β-Ga_2O_3 optical devices can actively be integrated with III-nitride based visible light sources and detectors [60]. Therefore, β-Ga_2O_3 is also a promising candidate for integrated photonics system, especially at UV and visible regime [28]. In order to understand and improve the performances of β-Ga_2O_3 devices, it's critical to carry out comprehensive investigations on its material properties, and intensive investigations have been reported on its electronic [61], optical [62-64], and thermal properties [65]. In terms of the optical properties of β-Ga_2O_3, previous researches mainly focused on the transmission [62], and refractive index [63,64]. However, the nonlinear optical properties of β-Ga_2O_3 have not been investigated yet, not to mention in UV and visible spectrum.

In UV and visible spectral range, under high optical power density, the performance of optical waveguides and resonators are mainly degraded by two-photon absorption (TPA)

process. For resonators that operate under critical coupling from bus waveguides, the refractive index shifting caused by Kerr nonlinear refractive index is influential to the coupling efficiency, especially in ultra-high quality factor resonators [66]. Therefore, in order to demonstrate high performance β-Ga_2O_3 based optical devices, it's critical to characterize the nonlinear optical properties of β-Ga_2O_3 including TPA coefficient and Kerr nonlinear refractive index.

To investigate and evaluate the nonlinear optical properties of β-Ga_2O_3 in visible spectral range, typical Z-scan characterization was performed. It's found that β-Ga_2O_3 has much smaller two-photon absorption coefficient (20 times smaller) and Kerr refractive index (4-5 times smaller) [38] than GaN, which is ideal for waveguides and resonators. Furthermore, due to the highly asymmetric crystalline structure of β-Ga_2O_3, the optical nonlinearity is highly anisotropic. Relative stronger nonlinear optical anisotropy was observed on $(\bar{2}01)$ plane than on (010) plane. These result can serve as references for the design of photonic devices based on β-Ga_2O_3.

This section is organized as the following: We firstly describe methods used in this work, then the experimental results are discussed mainly on its significance in integrated photonics system. At the end, we draw a short conclusion of this part of research.

The unintentionally doped (UID) β-Ga_2O_3 samples were provided by Tamura Corporation with the carrier concentration on the order of ~10^{17} cm^{-3} and the thickness of ~ 500 μm. The backside of the samples was polished by hand-grinding method with diamond lapping film of 0.5 μm grade. The polishing process was carefully controlled so

that the thickness of the samples after polishing was reduced by less than 100 μm. Figure 2-6 depicts the crystal structure of β-Ga_2O_3, the (010) and ($\bar{2}$01) planes are also indicated.

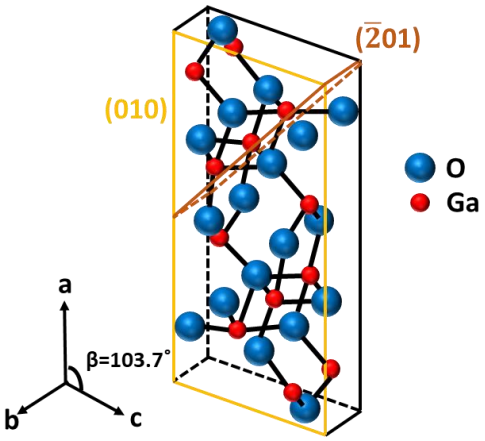

Figure 2-6. Crystalline structure of β-Ga_2O_3.

The experimental setup used in this study is similar to Fig. 2-1. Standard Ti:Sapphire laser was utilized as light source with 100 fs pulse width and 82 MHz repetition rate. A $\chi^{(2)}$ crystal was used to generate second harmonic wave at the wavelength of 404 nm. The average power of input second harmonic beam was kept at 12 mW, which corresponds to ~7×10^9 W/cm^3 peak power density and ~0.7 mJ/cm^3 single pulse energy density. Half wavelength plate working on 404 nm was placed after $^{(2)}$ crystal for light polarization tuning. During testing, the position of out-coupling objective was dynamically adjusted according to the position of the samples to ensure that the transmitted light is efficiently collected. An aperture was implemented in front of power meter to perform open and closed aperture testing.

To test the reliability of the setup, the beam size of the output light is used as an indicator. Based on Gaussian optics, with an incident beam diameter of 4 mm and a numerical aperture (NA) of 0.25, the calculated diameter of the output light is ~5 um (at

$1/e^2$). This value is consistent with the beam diameter we extracted from open aperture Z-scan measurement in the next section.

The TPA coefficient and Kerr refractive index can be obtained from open/closed aperture scanning based on Eqs. (2-1)–(2-3). The wavelength-dependence of the TPA coefficients can be estimated using Eq. (2-4).

It should be pointed out that although β-Ga_2O_3 exhibits indirect bandgap, the direct bandgap energy (4.9 eV) is close to its indirect bandgap (4.85eV) [58]. Therefore, in our theoretical analysis, we do not consider phonon assisted TPA because it only contributes optical nonlinearity at a narrow bandwidth.

Figure 2-7 shows the open/closed aperture scanning results for (010) and $(\bar{2}01)$ β-Ga_2O_3. Fitting the experimental data with Eqs. (2-1)–(2-3) yields the TPA coefficient and Kerr nonlinear refractive index, which was summarized in Table 2-2. It can be observed that the $(\bar{2}01)$ β-Ga_2O_3 has smaller TPA coefficient than (010) β-Ga_2O_3. This result indicates $(\bar{2}01)$ β-Ga_2O_3 waveguides and resonators exhibit less loss induced by TPA in visible spectral regime. On the other hand, $(\bar{2}01)$ β-Ga_2O_3 has larger Kerr nonlinear refractive index. The output beam diameters were also obtained, which were in good agree with theoretical calculations based on Gaussian optics.

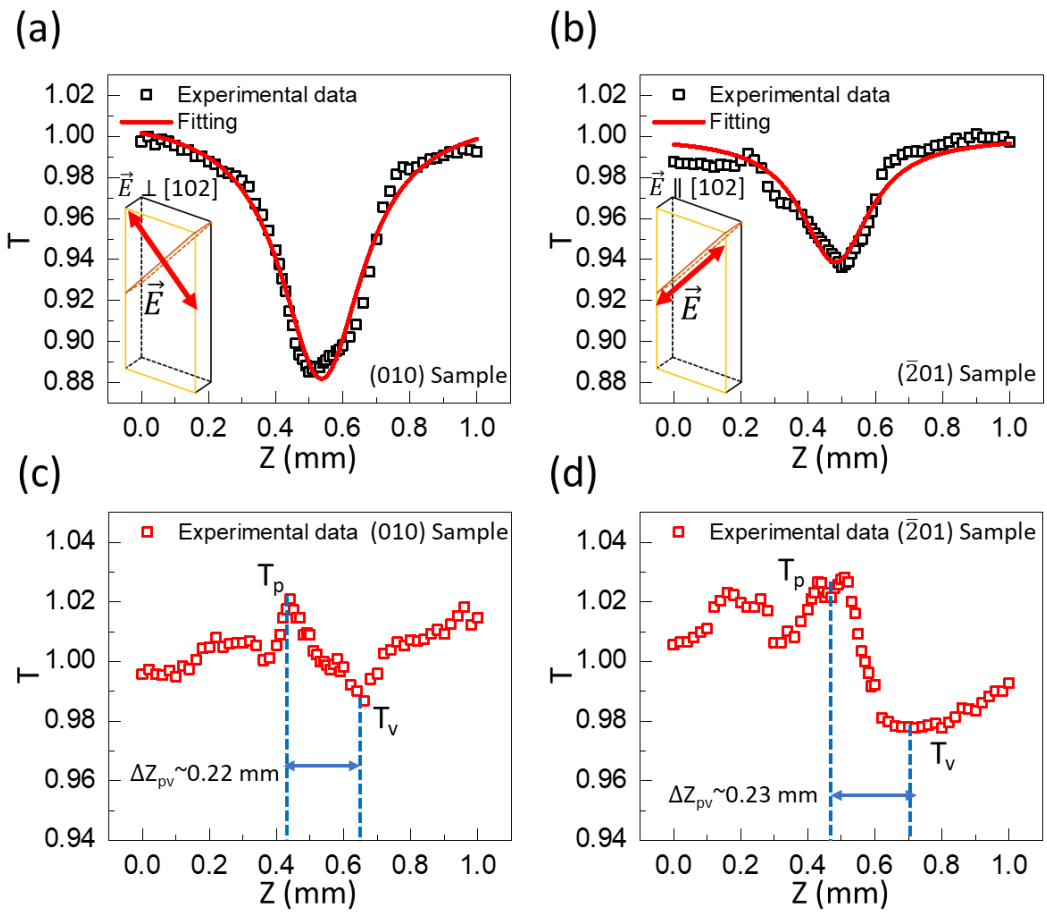

Figure 2-7. The open aperture and closed aperture plots obtained in this work. (a) Open aperture scan curve for (010) sample, (b) open aperture scan curve for ($\bar{2}$01) sample. (c) and (d), closed aperture Z-scan measurement of (010) and ($\bar{2}$01) samples, respectively.

Table 2-2. TPA coefficient, Kerr nonlinear refractive index obtained in this work for (010) and ($\bar{2}$01) samples. Beam diameter from fitting parameter is also shown.

(010), $\vec{E}$ ⊥ [102]			($\bar{2}$01), $\vec{E}$ ∥ [102]		
α_{TPA}(cm/GW)	n_{kerr}(cm^2/W)	R(μm)	α_{TPA}(cm/GW)	n_{kerr}(cm^2/W)	R(μm)
1.2	-2.1×10^{-15}	5.8	0.6	-2.9×10^{-15}	5.7

From Figs. 3-7(c) and 3-7(d), it can be clearly observed that closed aperture measurement exhibits more intense noise comparing with open aperture curve. This can be

mainly attributed to two reasons: firstly, the testing wavelength was located at 404 nm which is the second harmonic beam from Ti:Sapphire laser, therefore, comparing with our previous work, the laser power was more than 20 times lower. It is the low power that makes the noise from beam nonidealities more significant, which results in the "bump" and "dip" features in Fig. 2-7 at Z~0.2 mm. Secondly, according to [48], n_{kerr} is supposed to be zero near ~0.7E_g photon energy, which corresponds to 3.4 eV for β-Ga_2O_3, since the testing photon energy at 404 nm is ~3.1 eV, the n_{kerr} is supposed to be in a relative small magnitude, this also increase testing difficulties throughout the experiment. To verify the closed aperture data, relation $Z_{pv} \approx 1.7Z_0$ was implemented [45], the Z_{pv} represents peak-valley distance in closed aperture scan and Z_0 was obtained from Eqs. (2-1a) and Eq. (2-1b). Fitting of Figs. 2-7(a) and 2-7(b) yielded Z_0 of 0.15 mm and 0.13 mm, corresponding to Z_{pv} of 0.25 mm and 0.22 mm, respectively, which is consistent with the measured (0.22 mm and 0.23 mm) Z_{pv} shown in Figs. 2-7(c) and 2-7(d).

It also worth noting that below 3.4 eV photon energy, using the widely implemented fitting model [48] developed by M. Sheik-Bahae et al. the Kerr nonlinear refractive index is supposed to be positive, while the n_{kerr} obtained in this work is negative. Such negative n_{kerr} value has profound physics behind. As suggested in [48]. The Kerr nonlinear coefficient is contributed from TPA effect, Raman effect, linear stark effect, and quadratic stark effect. For n_{kerr} obtained at relative long wavelength, fitting model implementing only TPA effect is sufficient. However, at short wavelength (~0.7 E_g photon energy), contribution from TPA effect is approaching zero and quadratic stark effect contributes significant negative phase change which in turn gives negative Kerr nonlinear refractive

index. This explains why negative Kerr nonlinear refractive index was obtained in this work.

We previously estimated TPA coefficients and Kerr nonlinear refractive index for GaN [38] at same wavelength. The TPA coefficient of (010) and $(\bar{2}01)$ β-Ga_2O_3 are ~10 and ~20 times smaller than that of GaN at 404 nm, respectively. Since the bandgap energy of β-Ga_2O_3 and GaN are different, it also worth comparing their nonlinear optical coefficient at same relative photon energy which is defined as E_p/E_g (0.63 for β-Ga_2O_3 tested at 404 nm). At E_p/E_g = 0.63 relative photon energy, TPA coefficient of (010) and $(\bar{2}01)$ samples are ~15 and ~30 times smaller than that of GaN. The high TPA coefficient observed in GaN might due to its exciton effects [50]. This result implies that β-Ga_2O_3 material is more capable to handle high optical power density applications in visible wavelength spectral range. Furthermore, Kerr nonlinear refractive index of β-Ga_2O_3 are also 4–5 times smaller at 404 nm and 5–7 times smaller at same relative photon energy than that of GaN. Therefore, β-Ga_2O_3 based resonators are expected to exhibit extreme coupling stability under high power operation comparing with GaN based resonators.

Figure 2-8 represents the polarization dependences of transmission minimum of (010) and $(\bar{2}01)$ β-Ga_2O_3 during open aperture testing. Since β-Ga_2O_3 has a monoclinic crystal structure (Fig. 2-6), 41 independent nonzero elements are required to fully describe its third order nonlinearity d_{il}. Therefore, it is very difficult and inconvenient to find explicit expression for d_{eff} using polarization angle and individual nonlinear component d_{il} [45,50]. To describe the in-plane anisotropic nonlinearity clearly, we use $\Delta T_{max}/\Delta T_{min}$ in this work.

Relative higher in-plane nonlinear optical anisotropy was found on $(\bar{2}01)$ β-Ga_2O_3 with $\Delta T_{max}/\Delta T_{min}$ of 1.93 while (010) β-Ga_2O_3 had a $\Delta T_{max}/\Delta T_{min}$ of 1.29.

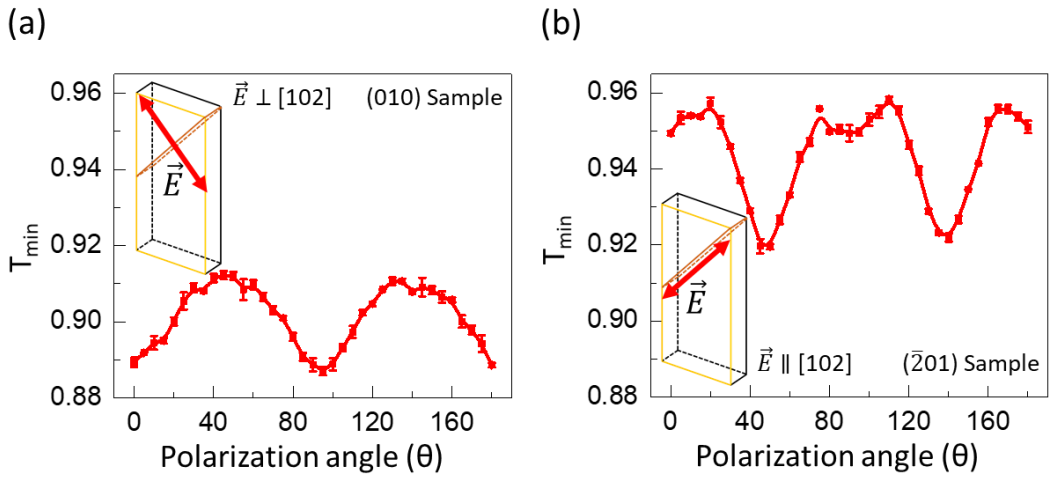

Figure 2-8. Polarization dependence of minimum transmittance obtained in this work. (a) Polarization dependence for (010) sample, (b) for $(\bar{2}01)$ sample.

Figure 2-9 shows the wavelength dependence of TPA coefficient using Eq. (3-4) for (010) and $(\bar{2}01)$ β-Ga_2O_3. For (010) β-Ga_2O_3, $E\perp$ has larger TPA coefficient that $E\parallel$. For $(\bar{2}01)$ β-Ga_2O_3, $E\perp$ has smaller TPA coefficient that $E\parallel$. Highest TPA absorption coefficient is observed in (010) β-Ga_2O_3 when electric field is perpendicular to [102] direction, while lowest TPA coefficient is obtained on $(\bar{2}01)$ β-Ga_2O_3 when electric field is parallel to [102] direction. For each plane, the polarization dependence of TPA coefficient is a function of multiple physical parameters [67] such as bond iconicity, covalent radii, etc. It is extremely difficult to give a quantitative explanation and out of the scope of this work. Future experimental and theoretical studies are undergoing to clarify its polarization dependence. For both samples, the maximum TPA absorption occurs at ~360 nm wavelength. For wavelength above 360 nm, TPA coefficient decreases as wavelength increases. It can be attributed to the decreased excitation energy with

increasing wavelength. While for wavelength below 360 nm, the TPA coefficient increase with increasing wavelength as the transition approaches its resonance wavelength.

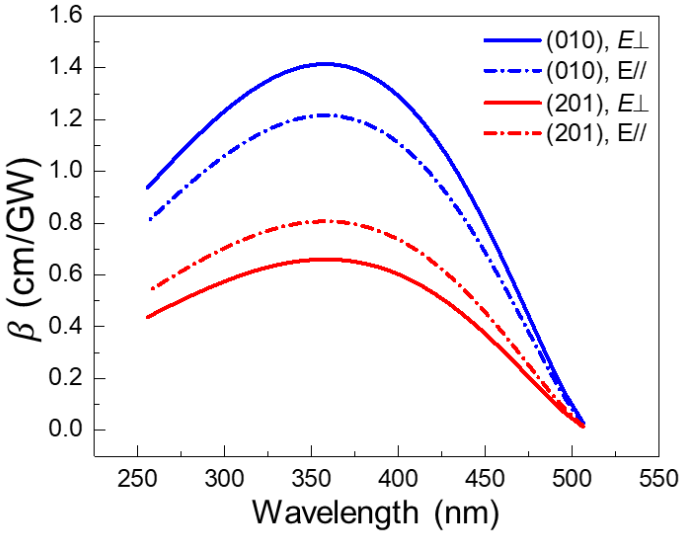

Figure 2-9. The estimated wavelength dependence of TPA coefficient for (010) and ($\bar{2}$01) samples. "E⊥" indicates that the electrical field intensity is perpendicular to [102] direction, while "E∥" indicates that field intensity is parallel to [102] direction.

In a short conclusion, we characterized the TPA coefficient and Kerr nonlinear refractive index of both (010) and ($\bar{2}$01) β-Ga_2O_3. TPA coefficient of Ga_2O_3 was found to be 10 to 20 times smaller than that of GaN at 404 nm. The Kerr nonlinear refractive index of Ga_2O_3 was 4 to 5 times lower than that of GaN. Therefore, due to its ultra-low TPA coefficient and its small Kerr nonlinear refractive index, β-Ga_2O_3 has the potential to serve as a more efficient platform for integrated photonic applications in UV and visible spectral range. Furthermore, the optical nonlinearities of β-Ga_2O_3 is highly anisotropic due to the asymmetric crystal structure of β-Ga_2O_3. These results can serve as guidelines for designing β-Ga_2O_3 based integrated photonics system.

2.4 Estimation on the Kerr nonlinear refractive index of AlN

Due to the difficulties in obtaining high quality bulk AlN and the large two-photon absorptive photon energy, direct Z-scan measurement on high quality AlN is still not reported. One exception is the report by M. Zhao et al. [68], in which the TPA coefficient and n_{kerr} at $\lambda = 355$ nm of AlN were measured to be 13 ± 3 cm/GW and $-1.91\pm0.38\times10^{-13}$ cm^2W^{-1}, respectively. Noting that the AlN sample used in [68] exhibits strong optical absorption below λ=300 nm, the crystalline quality is distant from high quality single crystalline.

Instead, one can adapt the derived n_{kerr} of $2.3\pm1.5\times10^{-15}$ cm^2W^{-1} at 1550 nm [69] and utilize the wavelength dependence fitting provided in [48] to roughly estimate the nonlinear optical performance in UV and visible spectrum. The estimated n_2 at 800 nm is 3×10^{-15} cm^2W^{-1} and 1×10^{-14} cm^2W^{-1} at 400 nm as shown in Fig. 2-10.

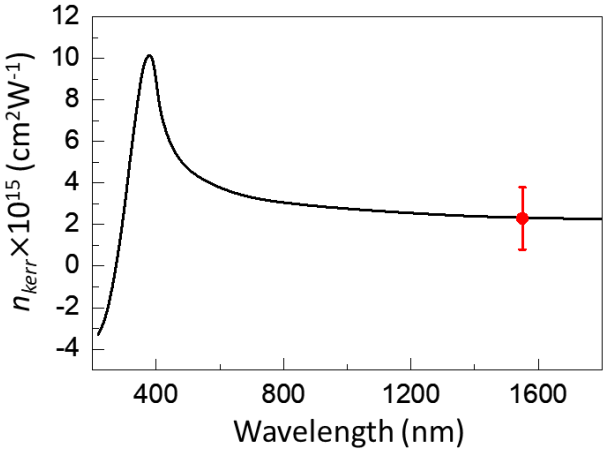

Figure 2-10. The estimated wavelength dependence of n_{kerr} for AlN.

CHAPTER 3

FABRICATION PROCESSES OF III-N PHOTONIC WAVEGUIDE

Nano/micro fabrication plays an important role in the research of photonic integration. The Rayleigh's law suggests that the scattered loss is proportional to λ^{-4} within a homogeneous medium, which implies that when scaling the wavelength from telecom to visible wavelengths, the scattering loss is expected to increase. More realistic modeling for scattering loss analysis should take waveguide confinement into account and is discussed in chapter 4. In this chapter, the main topic is to explore optimal fabrication processes for III-N based PICs.

3.1 A brief introduction on cleanroom facilities

Samples subjected to this research were mostly fabricated within the ASU nanoFab facilities. The fabrication processes include metal/dielectric deposition, photo/e-beam lithography, and dry/wet etching. The facilities involved within this research are summarized as followed:

1. **JEOL JBX-6000 FS/E Electron Beam Lithography**: This facility serves as the lithography tool for nanoscale fabrication.
2. **EVG 620 Aligner**: This facility serves as the photo-lithography tool for micro-fabrication.
3. **OAI 808 Aligner**: This is another facility that is utilized for photo-lithography similar to EVG.
4. **CEE Spin Coater**: This is a photoresist coating tool. The photoresist used in this research is ma-N 2403 (negative, E-beam), AZ4330 (positive, photo-lithography),

AZ 3312 (positive, photo-lithography), and LOR-3A (positive, photo-lithography, mainly for lift-off purposes).

5. **Lesker E-beam Evaporator**: The E-beam evaporator is used for metal deposition including Al, Au, Cr, Ni, and Ti. The Cr can be used for hardmask during dry etching within fluorine environment, while Al, Au, Ni, and Ti are common metal materials for Ohmic and Schottky contacts on III-N [70].
6. **Edwards2 Thermal Evaporator**: This tool shares similar functionality as Lesker E-beam evaporator.
7. **Oxford Plasma-enhanced Chemical Vapor Deposition (PECVD)**: This PECVD tool is employed for the deposition of SiO_2, SiN, and SiO_xN_y. The deposited SiO_2 can be served as hardmask and dielectric cladding for photonic waveguide. The oxide and nitride compositions of SiO_xN_y can be properly tuned to match the refractive index of sapphire substrate (~1.7) for cladding layers.
8. **Cambridge Savannah Atomic Layer Deposition (ALD)**: This tool is used for the deposition of high quality Al_2O_3, which has the potential to passivate the surface dangling bonds of etched III-N surface and reduce trap states.
9. **PlasmaLab M80 Plus – Chlorine**: This is a reactive-ion etching (RIE) tool with Chlorine based chemistries. It was mainly used for the etching of Cr in the early stage of this research.
10. **PlasmaLab M80 Plus – Fluorine**: This is another RIE tool with Fluorine based chemistries. It was mainly used for isotropic SiO_2 etching.

11. **PlasmaTherm 790 RIE – Fluorine**: This is the main RIE tool used within this research with F based chemistries. All anisotropic SiO_2 etching during this research was performed with this tool.
12. **STS AGE Inductively Coupled Plasma (ICP) Etching**: This tool provide Chlorine based etching environment and all etchings on GaN and AlN were performed in this tool.
13. **PlasmaTherm Apex ICP**: The etching chemistries used in this tool is Chlorine based. This tool is mainly used for Cr etching.
14. **Tegal 421**: This tool provides oxide plasma for the ashing of photoresists.

Some back-end processes were performed in the ASU Eyring Material Center. The facilities involved are:

1. **Multiprep – Allied**: This is a tool for the polishing of waveguide input/output facet.
2. **Other tools**: Some other tools including microscopes and wafer cutting machines were located within this lab.

3.2 Fabrication process for GaN waveguide

By leveraging the tools mentioned above, III-N PICs can be fabricated. The fabrication process for GaN based diode [71] was used as a starting point for this investigation, and the initial fabrication process is shown in Fig. 2-1. The samples grown by MOCVD were firstly coated with AZ4330 or AZ3312 resist, followed by the lithography and development in MIF300. The geometries of waveguides were defined by ICP etching and the residual resist were removed by acetone and isopropyl alcohol (IPA)

rinsing. Input and output facet of the device was defined by manual cutting using diamond blade.

Figure 3-1. The fabrication process of GaN waveguide in the initial stage of this research.

Several issues were found when using the fabrication recipes mentioned above. In the visible spectrum, device dimensions are scaling with wavelengths, and the optical lithography lacks enough resolution to define the device geometry. For example, to achieve critical coupling from bus waveguide to resonators with intrinsic Q factor on order of 10^5, the gap between bus and loaded resonator is below 300 nm. For fiber-chip coupling, grating couplers are required, and the period of gratings are also on the order of 100s of nanometers. The optical lithography tool (used in this research) fail to handle the dimensions mentioned above, and the e-beam lithography is required to achieve the aforementioned resolution. Moreover, in the initial stage of research, fast pace changing of layouts are expected, which leads to the frequent replacement of photo-mask, e-beam lithography provides the flexibility of layout changing.

In addition to the issues on lithography, the removal of photoresist is also problematic. The etching of GaN relies on chlorine based chemistries and the etching is biased above 150V. After etching, certain amount of chlorine related complex compounds are remaining within the photoresist, which makes the photoresist irremovable by simple

acetone + IPA rinsing. Figure 3-2 shows the fabricated GaN waveguide with photoresist remaining on the top.

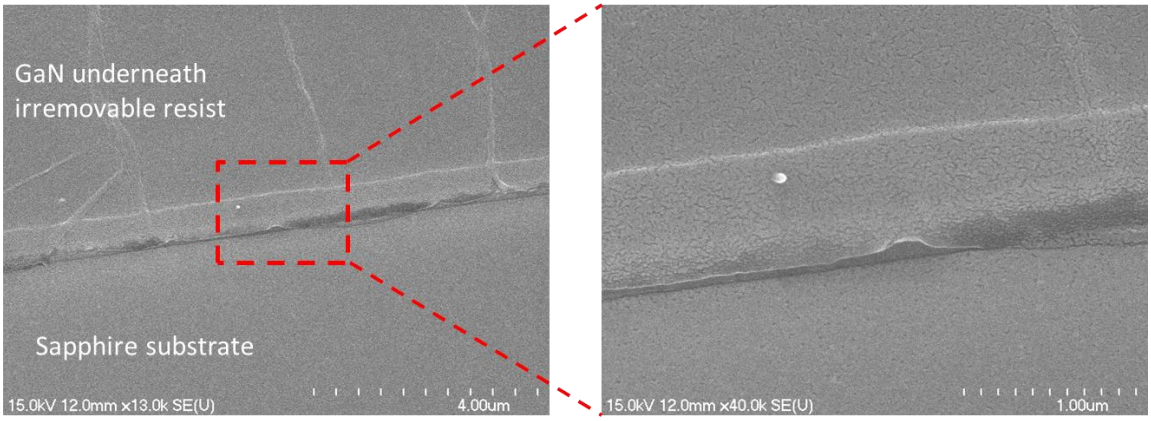

Figure 3-2. The SEM image of fabricated GaN waveguides in the initial stage of this research. The GaN ridge is underneath irremovable resist.

Some other issues were also arising in the initial stage, for example, due to the mechanical hardness of sapphire substrate, the manual cutting via diamond blade is challenging and would cause damages to the input/output facet. The line-edge roughness of photoresist after development is also very sensitive to development time duration and pattern geometry.

To tackle the obstacles mentioned above, new fabrication process flow is investigated within this research. The e-beam lithography is adopted, and the resist is replaced by ma-N 2403. The typical resist thickness of ma-N 2403 is 250 nm (5000 rms spinning). The normalized thickness versus dose relation was characterized as shown in Fig. 3-3. The dose of e-beam exposure is kept above 100 $\mu C/cm^{-2}$throughout this research.

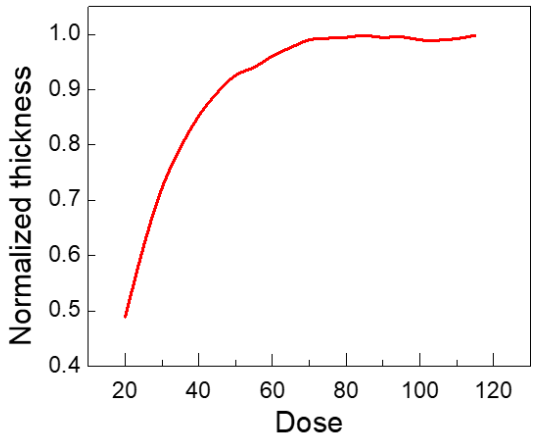

Figure 3-3. The normalized resist thickness versus dose of ma-N 2403 resist.

The ma-N 2403 is not selective in Chlorine based etching, which is commonly required in III-N etching [71]. Therefore, the pattern is firstly transferred to Cr hardmask, the Cr hardmask exhibit extreme slow etching speed within Fluorine based etching environment so that the pattern can be further transferred to SiO_2 via Fluorine based RIE. Finally, the pattern of GaN waveguide can be defined using ICP etching with SiO_2 hardmask.

To avoid the residual photoresist after acetone + IPA rinsing, the O_2 plasma ashing is adopted after Cr etching. The residual SiO_2 after ICP etching can be removed by buffered oxide etch (BOE). After fabrication, 3 μm of SiO_2 is deposited on the PICs as cladding layer. The quality of input/output facet is improved by polishing using silicon carbide and diamond lapping films. The established process flow is shown in Fig. 3-4.

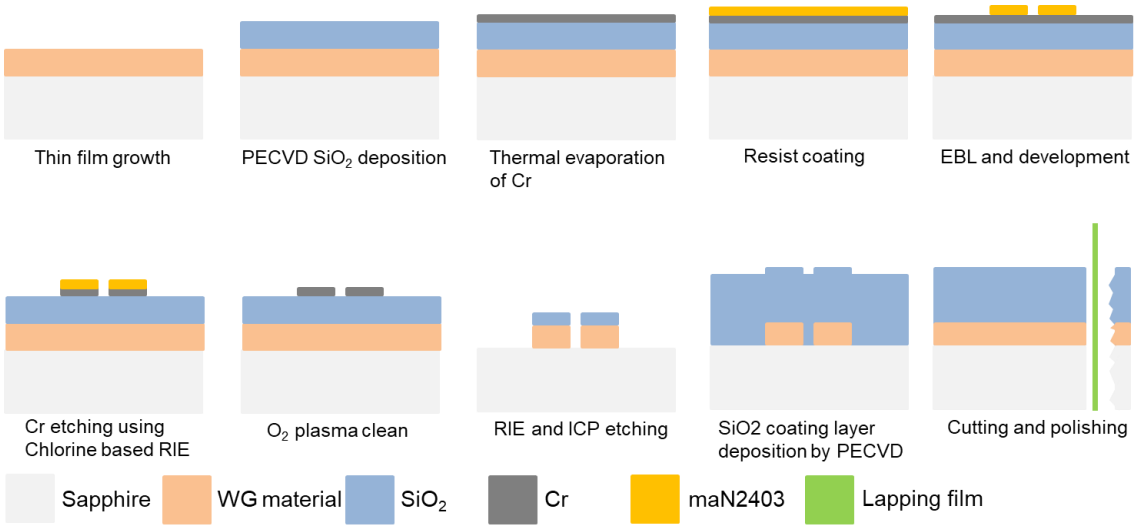

Figure 3-4. The established fabrication process flow for GaN PIC. The MOCVD grown thin film is firstly covered by SiO_2 and Cr hardmasks. The pattern is firstly defined by ma-N 2403 after exposure and development and then transferred to Cr and SiO_2 via RIE. The PIC geometry is finally defined by ICP etching. Thick layer of PECVD oxide is covered on the top of GaN as cladding layer. Mechanical cutting and polishing are performed to define input/output facet.

The ASU nanoFab kindly provides standard recipes for large portion of processes mentioned above. While several recipes were customized within this research for better yield and/or performance. The etching of Cr was initially performed using PlasmaLab M80 Plus – Chlorine RIE with Cl_2, O_2, and BCl_3 chemistries. This recipe is unstable as the Cr layer may be oxidized when placing outside chamber for certain amount of time. To stabilize this etching process, PlasmaTherm Apex ICP was utilized and 3 sccm of argon was added so that the moderate physical bombardment can remove oxidized Cr layer with stable speed. The customized recipe for Cr etching is 30 mTorr chamber pressure with 40/250 W RF/ICP power. The etching chemistry is 22/8/3 sccm for $Cl_2/O_2/Ar$.

Some examples of fabricated GaN patterns are given in Fig. 4-5. Some fabricated circular shapes are shown in Figs. 3-5(a) and 3-5(b). It can be easily observed that the residual resist is removed by O_2 plasma clean.

The ICP etching recipe of GaN is provided in [71], the etching speeds of GaN and the masking material are ~250 nm/min and ~100 nm/min. The waveguide performance is evaluated in Chapter 4. To summarize, the detailed fabrication process flow for GaN PICs is provided in Table 3-1.

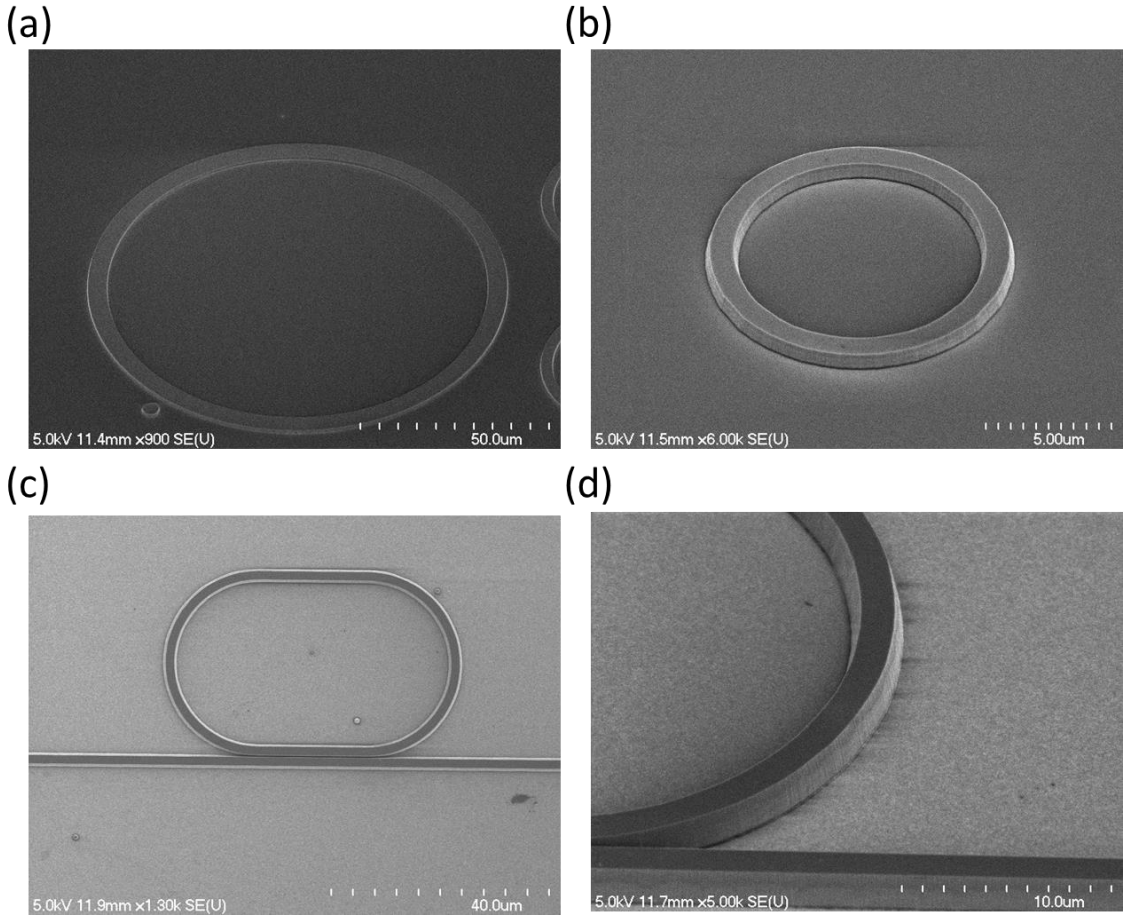

Figure 3-5. Some typical SEM images of fabricated patterns. (a), (b) Some circular shapes with different magnification. (c), (d) Bus waveguide and loaded resonator.

Table 3-1. Detailed fabrication process flow for GaN PIC.

Step	Process	Functionality	Recipe
1	PECVD	Deposit 300 nm SiO_2 hardmask on top of GaN	ASU standard SiO_2 PECVD recipe, deposition speed at 70 nm/min.
2	Thermal evaporation	Deposit 50 nm of Cr hardmask on top of resist	Deposition speed at ~1 nm/s. E-beam power kept at ~2%
3	Resist coating	Negative resist for e-beam lithography.	Spinning speed at 5000 rms. Thickness at 250 nm. Bake at 100 ˚C for 1 min.
4	E-beam lithography	Transfer the pattern to resist.	Dose at 120 μC/cm^{-2}.
5	Development	Remove the unexposed resist.	35 second within ma-D 525, no bake required.
6	ICP etching	Transfer pattern from resist to Cr.	30 mTorr pressure, 40/250 W of RF/ICP power. $Cl_2/O_2/Ar$ flow of 22/8/3 sccm. Typical etching speed ~50 nm/min.
7	O_2 plasma ashing	Remove residual resist (2-3 min).	400 mTorr pressure, 200 W RIE power.
8	RIE etching	Transfer pattern from Cr to SiO_2.	ASU standard SiO_2 RIE etching recipe, etching speed at 50 nm/min.
9	ICP etching	Transfer pattern from SiO_2 to GaN.	5 mTorr pressure, 80/400 W of RF/ICP power. $Cl_2/BCl_3/Ar$ flow of 30/8/5 sccm. Typical etching speed ~250 nm/min.

3.3 Fabrication process for AlN waveguide

To investigate the optimal fabrication process for AlN waveguide, the process flow shown in Fig. 3-4 was chosen as the starting point. Due to the strong bonding energy of AlN [72]. The etching bias used in GaN etching [71] cannot sufficiently remove the material and get reflected from sidewall, the reflected argon ions bombarded the substrate instead. The boundary of this ion bombarded region is clearly marked in Fig. 3-6(a).

To sufficiently bombard the sidewall of AlN, the ICP etching recipe was modified from GaN etching recipes developed in previous section. Due to the strong bonding energy, the etching bias should be increased, to achieve high etching bias, larger RF power at 250 W and lower chamber pressure at 2 mTorr is utilized. As a result, the etching bias is increased from 150 V to 250 V as shown in Fig. 3-6(d). Due to the increased bias voltage, the selectivity between AlN and SiO_2 is reduced from 1:4 (for GaN case) to 1:2.

(a)

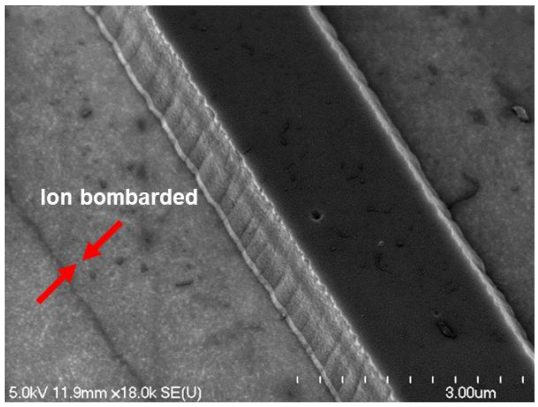

(b)

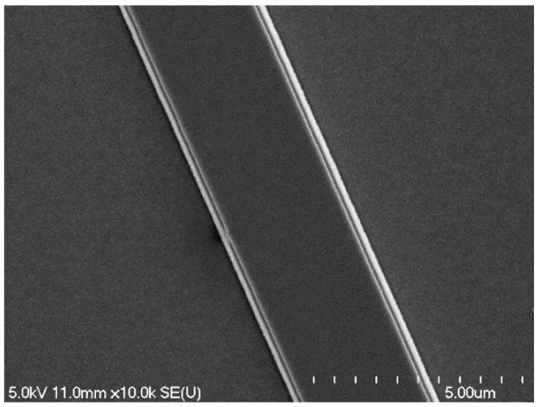

(c)

(d)

Material	GaN	AlN
Bonding energy	8.92 eV/atom	11.52 eV/atom
Etching bias	180V	280V
Etching rates	250 nm/s	250 nm/s

Figure 3-6. (a), (b) The ICP etched AlN waveguides before and after optimization. (c) The schematic that shows the bombardment on substrate from reflected argon ions. (d) The bonding energy, etching bias, and etching rates of GaN and AlN at the optimal point obtained in this research.

Another issue during this research is originated from the thermal evaporation of Cr. As indicated in [73], the optimal deposition speed of metals are related to its reactivity. For metals with higher reactivity such as aluminum, the optimal deposition speed can be around 10s of nanometers per second. While for the metals such as gold, silver and copper, the speed of deposition is relative slow. The reactivity of metal can be described by its standard electrode potential, and the Cr possesses electrode potential between aluminum and copper. This rule guides the optimization of Cr deposition speed, and the obtained results indicate that ~1 nm/s deposition speed of Cr provides good line-edge roughness as shown in Fig. 4-7.

(a)

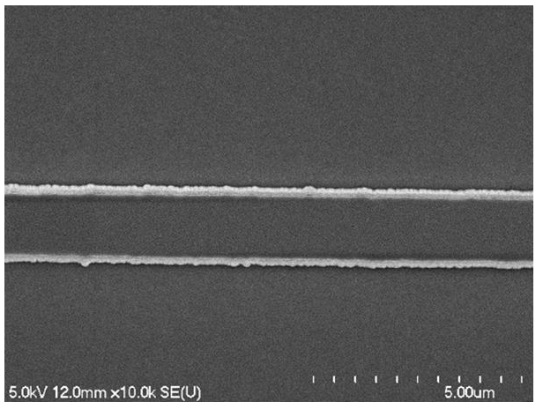

(b)

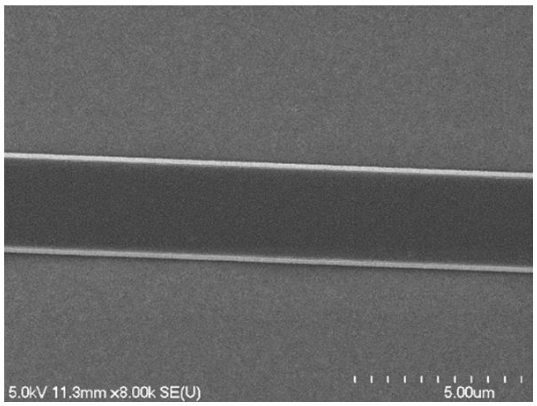

(c)

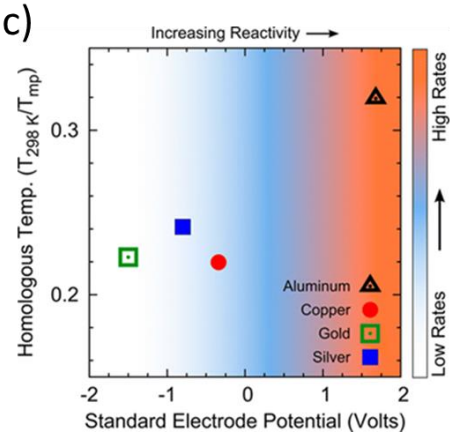

(d)

Material	Electrode potential
Gold	- 1.52 V
Silver	- 0.7996 V
Copper	- 0.52 V
Aluminum	+ 1.662 V
Chromium	+ 0.74 V

Figure 3-7. (a), (b) The ICP etched AlN waveguides before and after the optimization of Cr evaporation process. (c) The Homologous Temperature vs. Standard Electrode Potential for different materials. (d) The Electrode potential of Gold, Silver, Copper, Aluminum, and Chromium.

Another interesting finding during the investigation is that the GaN and AlN exhibit different response to BOE. For GaN, it's widely recorded that the HF within BOE does not etch GaN, therefore, the masking oxide and cladding oxide layers can be easily removed by BOE without influencing the PICs. However, for AlN, surface erosions were observed as shown in Fig. 3-8(a), which causes significant damage to waveguide layer. As a result, after ICP etching of AlN, the masking oxide are remaining on the top before further deposition of cladding layer as shown in Fig. 4-8(b).

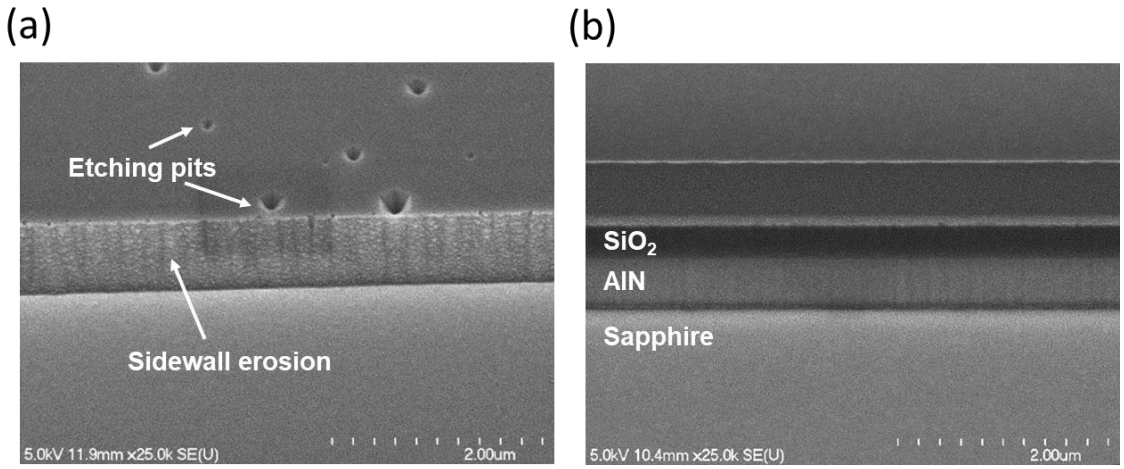

Figure 3-8. (a) The BOE treated AlN waveguides, etching pits and sidewall erosions can be easily observed. (b) AlN waveguides after ICP etching, no erosion was found.

To further improve the waveguide performance, several additional fabrication steps were involved when comparing with Fig. 3-4. First, after the ICP etching of AlN, a Al_2O_3 thin layer was deposited using ALD. Thanks to the excellent uniformity of ALD, this thin layer can provide full coverage on the etched sidewall, which passivates the dangling bonds and reduces the trap states at the surface. Second, the cladding material was changed from SiO_2 to SiO_xN_y. The refractive index of SiO_xN_y deposited by PECVD is shown in Fig. 3-9. When the PECVD recipe is properly selected, the index of SiO_xN_y can be matched with sapphire, this symmetric cladding index distribution is ideal for photonic crystal waveguides and resonators [74].

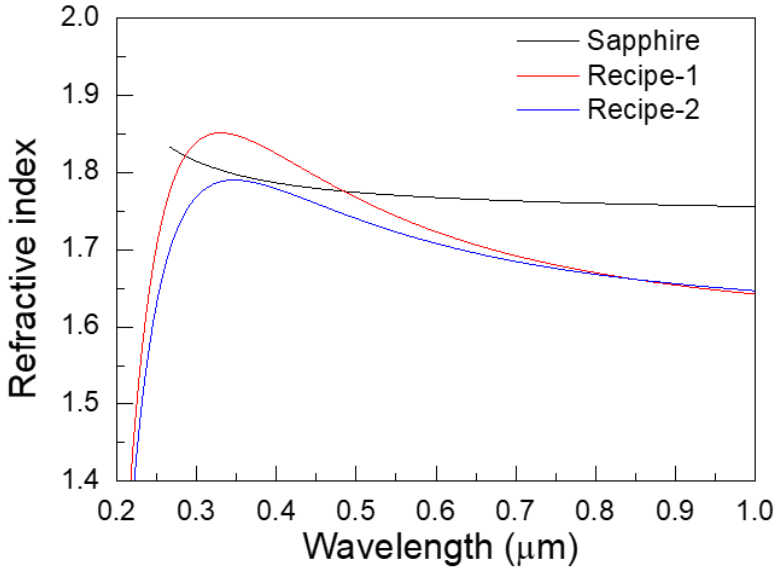

Figure 3-9. Refractive index of SiO_xN_y deposited by different recipes.

To summarize, the fabrication process of AlN with 1 μm height is summarized in Table 3-2. The developed recipes within this Chapter is used throughout the rest of Chapters.

Table 3-2. Detailed fabrication process flow for AlN PIC.

Step	Process	Functionality	Recipe
1	PECVD	Deposit 500 nm SiO_2 hardmask on top of AlN	ASU standard SiO_2 PECVD recipe, deposition speed at 70 nm/min.
2	Thermal evaporation	Deposit 80 nm of Cr hardmask on top of resist	Deposition speed at ~1 nm/s. E-beam power kept at ~2%
3	Resist coating	Negative resist for e-beam lithography.	Spinning speed at 5000 rms. Thickness at 250 nm. Bake at 100 ˚C for 1 min.
4	E-beam lithography	Transfer the pattern to resist.	Dose at 120 μC/cm^{-2}.

5	Development	Remove the unexposed resist.	35 second within ma-D 525, no bake required.
6	ICP etching	Transfer pattern from resist to Cr.	30 mTorr pressure, 40/250 W of RF/ICP power. $Cl_2/O_2/Ar$ flow of 22/8/3 sccm. Typical etching speed ~50 nm/min.
7	O_2 plasma ashing	Remove residual resist (2-3 min).	400 mTorr pressure, 200 W RIE power.
8	RIE etching	Transfer pattern from Cr to SiO_2.	ASU standard SiO_2 RIE etching recipe, etching speed at 50 nm/min.
9	ICP etching	Transfer pattern from SiO_2 to AlN.	2 mTorr pressure, 240/500 W of RF/ICP power. $Cl_2/BCl_3/Ar$ flow of 30/8/5 sccm. Typical etching speed ~250 nm/min.
10	ALD deposition (optional)	Thin layer of Al_2O_3 for passivation of AlN etched surface.	ASU standard ALD deposition recipe, deposition speed at 0.3 nm/min.
11	PECVD deposition	Thick SiO_2 or SiO_xN_y as cladding layer for waveguides.	ASU standard PECVD deposition recipe, deposition speed at 70 and 50 nm/min for SiO_2 and SiO_xN_y.
12	Cutting	Cut bare wafer into sample bars.	Using diamond blade for cutting.
13	Polishing	Polish the input and output facets to improve free-space to chip coupling efficiency.	Starting with silicon carbide lapping film in the grade of 30-100 μm. Followed by diamond lapping film from 12 μm down to 6 μm, 1 μm, and 0.5 nm grade.

CHAPTER 4

STUDY ON THE LOSS MECHANISMS OF III-N WAVEGUIDES

III-N based semiconductors have achieved great success in the fabrication of active optical devices such as light-emitting diodes (LEDs) [2] and lasers diodes [4], where they showed high radiative efficiency at the visible wavelengths, a spectral range that is unattainable using other materials [75]. For passive optical devices such as waveguides, resonators [27], and modulators [76], III-nitride materials are also expected to produce high performance devices especially at the visible and ultraviolet (UV) wavelengths due to their outstanding optical properties such as wide bandgaps (i.e., transparent at the visible and UV spectral range), low dispersion, active integration capability, and second order susceptibility [31]. Despite these advantages, however, the majority interests of the integrated photonics society have been focused on 1.55 μm wavelengths based on III-V or SiN materials for fiber optics applications, with only very limited experimental work on III-N passive optical devices such as photonic waveguides.

Recent progress on UV and visible integrated photonics [25-28] have opened up new opportunities for III-nitride photonics in applications such as biochemical sensing [25], Raman spectroscopy [77], beam steering [78], nonlinear optics [32], and quantum photonics [24]. For these applications, a high-power density pumping is typically required for various III-nitride waveguide structures. For example, applications such as stimulated Raman scattering, comb generation, and super continuum generation will require pumping power on the order of hundreds of milliwatts inside the waveguides. For other threshold-less process such as second harmonic generation and entangled photon generation, the power of the signals is typically proportional to the square of incident power, which could

be on the order of tens to hundreds of milliwatts [31]. These applications will therefore require high performance III-nitride waveguides with extremely low optical loss, which presents a major technical challenge. In contrast to traditional photonic waveguides (e.g., Si or III-V) at 1.55 μm where the optical loss is mainly due to the sidewall scattering effects, the performance of III-N waveguide at the visible spectral wavelength is dominated by several different loss mechanisms. First, under high power operation the optical loss of III-nitride waveguides is dominated by multi-photon absorption process [38]. Second, grain boundaries formed in III-N material grown on sapphire typically show different etching speeds during dry etching, which degrades the side wall roughness and hence introduces additional loss to III-N waveguides. Furthermore, due to the material epitaxial processes, some III-nitride materials (such as GaN) are intrinsically n-type doped, which will also lead to large free carrier loss to III-nitride waveguides. Since the free carrier loss is proportional to the inverse of carrier mobility [79], the material quality of III-nitride material (e.g., dislocation density) will have a strong impact on the waveguide performance. In this chapter, we performed comprehensive studies on the loss mechanisms in III-nitride waveguide devices from both theoretical and experimental aspects. Modeling on the sidewall scattering loss using 2D and 3D models were performed, and an original model was proposed for the analysis on defect induced scattering losses. Additionally, high performance GaN and AlN waveguides with extremely low optical loss of < 2 dB/cm was achieved, which can pave the way for various III-nitride integrated photonics applications. High quality GaN and AlN resonators were also demonstrated with state-of-the-art quality factors.

This chapter is organized as the following: We describe the theoretical analysis on the optical losses in III-nitride waveguides using III-N-on-sapphire as an example. Scattering loss, free carrier loss, and two-photon absorption (TPA) loss will be studied, and their contributions to the overall performance of waveguide devices will be discussed. Then, we described the experimental setups used in this study. The obtained results indicates different loss mechanisms. After the introduction of experimental results, a semi-analytical model is proposed for the estimation of defect induced scattering losses.

4.1 Modeling methods

In order to analyze scattering loss, free carrier loss, and TPA loss in III-nitride ridge waveguides, we first calculated the wave vectors and optical modes in the waveguides. A commercial software package by Lumerical Mode Solutions was implemented in this work, and the simulation setup is similar to our previous work [80]. The substrate of the simulation was chosen to be sapphire which is the most commonly used material for III-nitride epitaxial growth. Sapphire also provides sufficient optical confinement and is transparent at visible wavelengths. The schematic for the III-N-on-sapphire waveguide is shown in Fig 4-1(a), in which W and H indicate waveguide width and height, respectively. To simplify our discussion, W and H are equal throughout the analysis and their values vary from 0.1 μm to 1.6 μm. In order to study the wavelength dependence, modes at 1550 nm, 800 nm, 600 nm, and 400 nm are simulated, in which 1550 nm represents the telecommunication wavelength, 800 nm represents the wavelength of typical pulsed laser, 600 nm and 400 nm represent visible wavelengths. The finite difference method (FDM) solved dispersions of GaN and AlN is shown in Figs. 4-1(b) and 4-1(c).

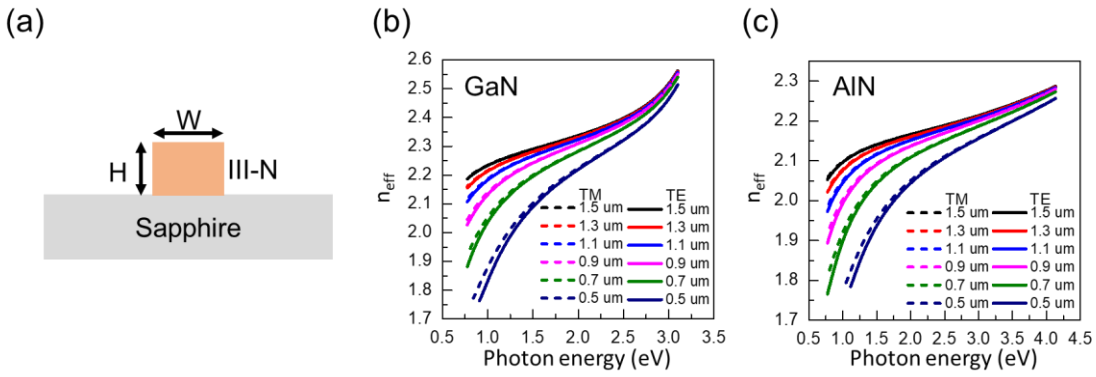

Figure 4-1. (a) Schematic of waveguide cross-section geometry. (b), (c) Effective refractive index of GaN and AlN versus photon energy solved by finite differential method.

It should be noted that high aspect ratio design with cladding layers covered on top of III-N in principle provides reduced scattering loss [81]. While this chapter is aimed at determine the loss mechanisms, therefore the optimizations were not applied.

For the scattering loss, we only considered sidewall roughness and neglected the upper surface roughness. This is because the III-nitride epitaxy layers usually have very smooth surface (e.g., roughness less than 1 nm [82]), while dry etching processes will give rise to surface roughness on the side walls which is typically on the order of several nanometers [83]. This simplification is taken in most of theoretical analysis dealing with sidewall scattering [84]. In this work, we used a widely discussed analytical model for scattering loss estimation, given in [84]. More advanced models utilizing coupled-mode techniques [85] or volume current method [86] will give higher accuracy, the utilization of advanced models will be implemented at the end of this chapter.

For the free carrier loss α_{FC}, we used an equation from Drude model [79]:

$$\alpha_{FC} = \frac{Ne^3}{m_e^{*2} n \varepsilon_0 \omega^2 \mu c} \tag{4-1}$$

where N indicates carrier density, m_e^* is the effective mass of electron, n is the refractive index, ω is the optical frequency, μ is the mobility. e, ε_0, and c are constants that represent elementary charge, vacuum permittivity, and speed of light, respectively.

For the TPA loss α_{TPA}, the following equation was used:

$$\alpha_{TPA} = \beta \frac{P_{in}}{A_{eff}} \tag{4-2}$$

where β is the TPA coefficient, P_{in} is the optical power inside waveguide, and A_{eff} is the mode area. We note here that for calculations on a GaN waveguide, we used β from [38], which involves a fitting parameter. This fitting parameter is a material-independent constant and typically has a larger value for wide bandgap materials such as III-nitrides. More information can be found in [45].

4.2 Experimental setup and fabrication processes

In order to couple light into waveguide, end-fire coupling method was employed. A laser beam from Ti:Sapphire laser in TE polarization was first expanded by free space optics to fully utilize the numerical aperture and then focused by a ×10 objective lens. The beam diameter was estimated to be ~ 2 μm using simple Gaussian optics estimation. Facet of waveguide was tapered to match the beam size of Gaussian laser beam coming out from objective. During testing, the facet of waveguide was positioned at focal point of the objective lens to achieve maximum power injection. The coupling efficiency was calculated to be ~ 30%.

The tapered facet of the GaN waveguide was polished to further enhance coupling efficiency. Before polishing, a SiO_2 layer was deposited to protect the waveguide during polishing. Samples were glued onto a holder and polished by diamond lapping film, after

which the glue and SiO_2 were removed. To test loss of the GaN waveguide, light was guided to propagate inside the waveguide for several millimeters and the scattering light was collected by the microscope and sent to a linear CCD camera. This setup is standard in loss characterization of waveguides and has been widely used. During experiment, gain of CCD camera was dynamically changed in order to avoid saturation of each pixel. By measuring the decay, waveguide optical loss can be extracted. Schematic of testing setup and typical CCD camera captured images are shown in Fig. 4-2.

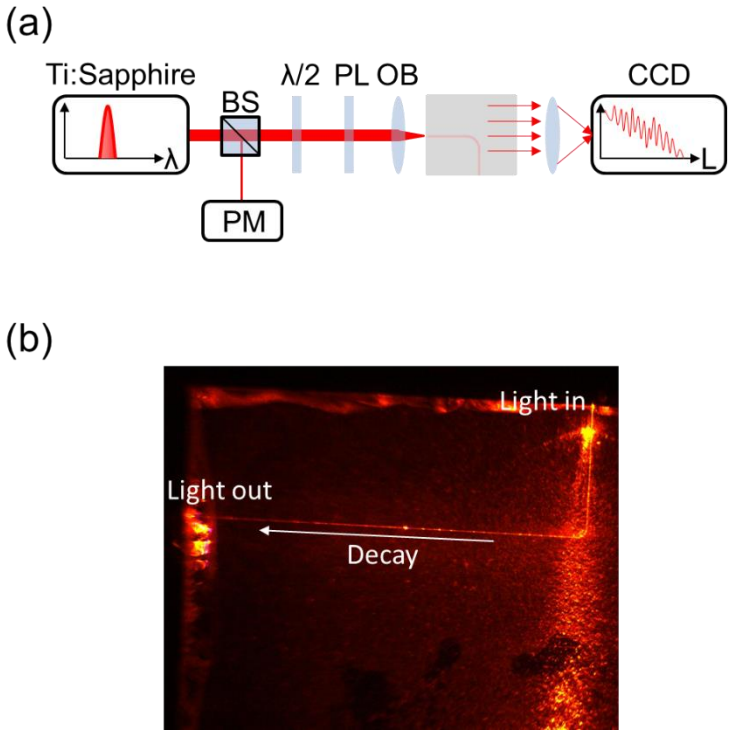

Figure 4-2. (a) Schematic of experimental setup. BS indicates beam splitter, PM indicates power meter, PL indicates polarizer, OB indicates objective lens, λ/2 is the half-wavelength plate. (b) CCD recorded image during measurement.

Details on the fabrication processes for III-N-on-sapphire waveguide developed for this work have been provided in Chapter 3. Therefore, the process is only briefly introduced here. For the fabrication of GaN waveguide, an unintentionally dope (UID) GaN thin film

with 1.5 μm thickness was grown on a sapphire substrate using a standard metal organic chemical vapor deposition (MOCVD) process. The Ga and N sources were trimethylgallium and ammonia, respectively. The carrier gas was hydrogen. 700 nm SiO_2 and 30 nm Cr layers were deposited using plasma-enhanced chemical vapor deposition (PECVD) and thermal evaporation, respectively. The SiO_2 layer was used as hardmask for GaN etching. Cr served as a hardmask and also provided conductivity during exposure in electron beam lithography (EBL).

The samples were then coated with a negative resist (ma-N 2403) from Micro Chem Corporation. Then, patterns were transferred to the samples by EBL, where the exposure was intentionally slightly overdosed to reduce sidewall roughness. After EBL exposure, samples were developed for 35 seconds in ma-D 525 developer, followed by chlorine (Cl_2) and fluorine (F_2) based reactive ion etching (RIE) to define the Cr and SiO2 hardmasks, respectively. The chlorine based RIE was performed under 100 mT chamber pressure and 20 V bias voltage, which produce isotropic etching profile with etching speed of ~ 40 nm/min. Due to the thin Cr thickness, this isotropic etching does not give much undercut but minimize the sidewall damage (roughness) of hardmask. While for the fluorine based RIE, the etching was performed under 20 mT pressure and 520 V bias voltage. Good anisotropy was achieved with etching speed of ~ 40 nm/min. Finally, an inductively coupled plasma (ICP) etching was used to form the waveguide structure. The ICP etching of GaN was also optimized following [71] to minimize side wall roughness with 400 W ICP power, 70W RIE power and 5 mT pressure using 30 sccm Cl_2, 8 sccm BCl_3 and 5 sccm Ar_2. Bias voltage during etching was ~ 160 V and etching speed was ~ 200 nm/min. After

ICP etching, residual SiO_2 was removed by one hour ultra etch 20:1 NP selective wet etching.

The scanning electron microscopy (SEM) images of devices are shown in Figs. 4-3(a) and 4-3(b). By collecting scattering light and measuring the decay, waveguide loss can be extracted. Figure 4-3(c) shows the SEM image of a typical sidewall profile for GaN waveguides with optimized etching process. A smooth sidewall profile was obtained using optimized etching processes, where RIE/ICP power were balanced and bias voltage was sufficiently high. Sidewall angle of the etched surface is estimated to be ~ 70˚ using the vertical and lateral profile obtained by Dektak stylus profiler and SEM images. Surface roughness was measured by atomic force microscope (AFM) and the root mean square (RMS) of height is typically 3.5 nm over 25 μm × 25 μm as shown in Fig. 4-3(d). Fabrication of AlN follows similar process as GaN and the details have been provided in Chapter 3.

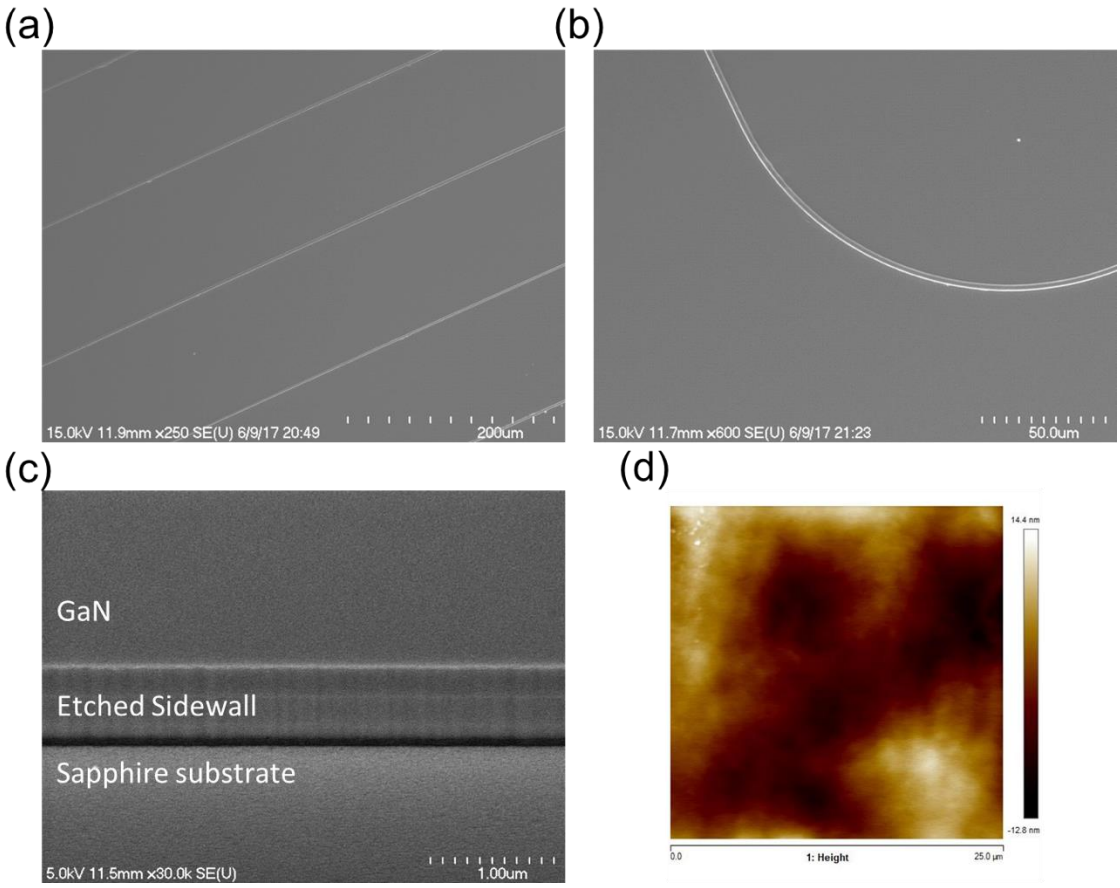

Figure 4-3. (a), (b) Typical SEM images of fabricated GaN waveguide. (c) Side view of etched GaN sidewall. (d) AFM image of GaN as-grown surface.

4.3 Simulated results

Figure 4-4(a) shows calculated sidewall scattering losses vs. wavelengths for the GaN waveguides at the dimensions1.6 µm × 1.6 µm and 0.6 µm × 0.6 µm when sidewall roughness (σ) is normalized at 1 nm, the scattering loss is proportional to the square of σ thus other roughness profiles can be easily obtained by multiplying σ^2. The AlN shares similar trends in respect to scattering loss as the two materials only exhibit different refractive index in this calculation. Different trends were observed for two waveguides

dimensions. For waveguide with 1.6 μm × 1.6 μm dimension (i.e., large waveguide dimension), a peak was observed at the 600 nm wavelength. This is because at very short wavelengths, modes are better confined inside the waveguides and interact less with the surfaces, which leads to lower scattering loss. When the wavelengths increase, the scattering loss increases due to the stronger interaction with surfaces. At very long wavelengths, however, surface roughness becomes less significant compared to the wavelengths, which lowers the scattering loss again. For waveguides at 0.6 μm × 0.6 μm dimension (i.e., small waveguide dimension), modes have more chance to interact with surface due to the relative smaller waveguides dimension. Therefore the scattering loss decreases with increasing wavelengths in this case since shorter wavelengths are more comparable to the roughness. Figure 4-4(b) shows the relationship between the scattering loss and the waveguide dimensions at 400 nm, 600 nm, 800 nm, and 1550 nm wavelengths, which are consistent with the results in Fig. 4-4(a). It was observed that as the dimension of the waveguide decreases, the optical loss increases due to the stronger optical confinement. It is also worth noting that for waveguides with dimensions above the micron scale, scattering loss becomes less significant, while at submicron dimension, scattering loss becomes more significant especially for visible light. Since sidewall roughness is usually attributed to different dry etching speeds at grain boundaries, III-N samples with high material quality are important when manufacturing low loss submicron waveguides.

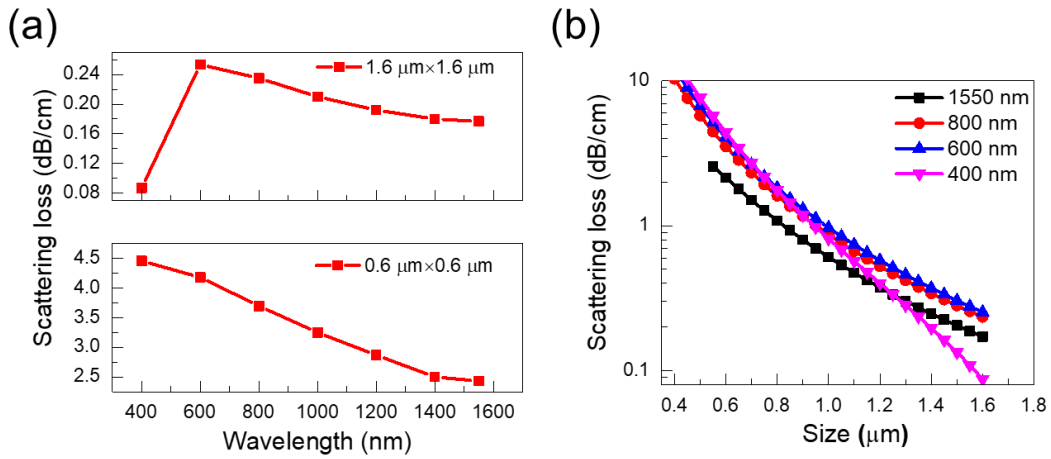

Figure 4-4. (a) Calculated sidewall scattering loss vs. wavelengths for GaN waveguides with dimensions of 1.6 μm×1.6μm and 0.6 μm×0.6 μm. (b) Calculated sidewall scattering loss vs. waveguide with wavelengths at 400, 600, 800 and 1550 nm. Sidewall surface roughness σ used in (a) and (b) is 1 nm which represents the ideal case.

From Eq. (5-1) it can be seen that the free carrier loss is proportional to N/μ, where N is the carrier density and μ is the carrier mobility. Since GaN is intrinsically n-type doped due to the material epitaxy processes (unlike other semiconductor materials such as GaAs, InP, and Si), they typically possess a large amount of n-type free carriers which will contribute to free carrier loss. For example, the n-type carrier density for unintentionally doped GaN is on order of 10^{17} cm^{-3} for GaN epilayers grown on foreign substrates such as sapphire [87], and on order of 10^{15} to 10^{17} cm^{-3} for GaN epi-layers grown on GaN bulk substrate [88,89]. These values are significantly higher than other semiconductors such as Si (10^{10} cm^{-3} [90]), GaAs (10^{6} cm^{-3} [91]), and InP (10^{7} cm^{-3} [92]). Furthermore, due to the limitation of current epitaxy technology, III-nitride materials are typically grown on foreign substrates such as sapphire or SiC, which results in a high dislocation density inside the III-nitride materials. The large amount of dislocations will reduce the carrier mobility, which will further increase the free carrier loss. Figure 3-5 shows calculated intrinsic free

carrier loss vs. wavelengths for GaN waveguides at dimension of 1.6 μm × 1.6 μm. To analyze loss contributed from free carrier absorption, two cases (ideal case and practical case) were studied and compared. The redline shows the ideal case, where the carrier density of GaN is chosen to be $N_0 = 10^{15}$ cm^{-3}, which is a typical number in commercialized bulk GaN substrate [88], the corresponding n-type carrier mobility is chosen to be $\mu = 1800$ cm^2/Vs, which was reported for high quality GaN materials with low dislocation density [93]. While black line indicates a practical case when $N/\mu = 10^3 N_0/\mu_0$, which represents the case of GaN materials grown on sapphire (typically has a high defect density of 10^9 cm^{-2}), where we picked N/μ to be 10^3 times higher than that in ideal case. The electron effective mass used in Eq. (4-1) is $0.2m_e$ [94], where m_e refers to the electron mass. Overall it is observed that for GaN waveguides, the free carrier loss decreases with wavelengths, indicating that the free carrier loss is less significant for GaN wavelengths at short wavelengths such as visible spectral range. In the ideal case, free carrier loss is almost negligible from 400 nm to 1600 nm. In the practical case, free carrier loss becomes larger than 1 dB/cm when the wavelengths are greater than 800 nm. These results show that GaN waveguides are more suitable to work at wavelength that shorter than 1 μm. For AlN, the nitrogen vacancies are located deeply inside bandgap [95], which in turn reduced the n-type conductivity. As a result, the free carrier loss within AlN is several orders of magnitudes lower than GaN and can be neglected in device design.

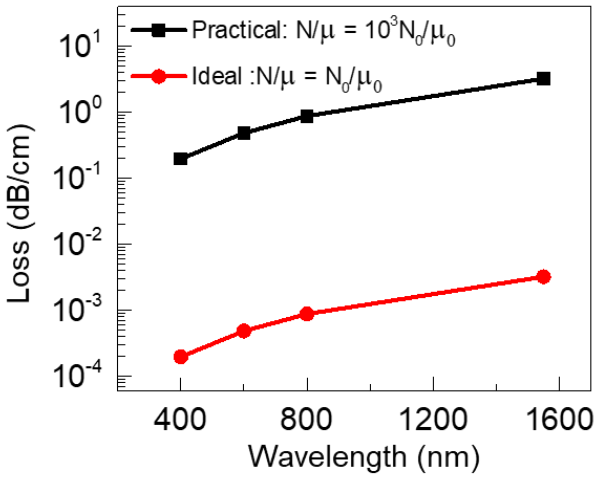

Figure 4-5. Calculated free carrier loss vs. wavelength for GaN waveguides at waveguide dimensions of 1.6 μm × 1.6 μm. The redline shows the ideal case (e.g., GaN on bulk GaN substrate), while black line indicates a practical case (e.g., GaN on sapphire substrate).

Figure 4-6(a) shows calculated TPA loss vs. waveguide dimensions for GaN waveguides at different wavelengths. At a fixed power density (e.g., 1000 mW), the TPA loss will decrease with waveguide dimensions due to increased energy densities. (We also note there that the optical power simulated in Fig. 4-6(a) is very practical in comb generation [32,33] and super continuum generations [44]). Figure 4-6(b) shows calculated TPA loss vs. incident power for GaN waveguides (dimension of 200 nm × 200 nm) at different wavelengths, where the TPA loss shows a linear dependence on the incident power for simulated GaN waveguides. The TPA loss will be < 1dB/cm for when the incident power is < 10 mW, and > 10 dB/cm when the incident power is > 100 mW.

Using the TPA coefficient data, we also estimated the quality factor for the waveguides at different incident power, and the results are shown in Fig. 4-6(c). The calculation is based on incident wavelengths of 710 nm, which locates at the half bandgap

energy of the GaN material. The mode area used in this calculation is 1 μm^2.The results show that quality factor *Q* remains constant when the incident optical power is low (e.g., < 1000 mW), and then drops dramatically when the incident power > 1000 mW. The TPA loss showed the opposite trend. This result implies that, on one hand, for waveguide applications under CW light operation, GaN waveguide-based ring resonators have decent performance since its quality factor drops above 1000 mW. While on the other hand, since a 1000 mW power density is practical for waveguide applications under pulsed light operations, the quality factor drop at high power range could limit GaN-based ring resonators' applications in ultrafast optics where peak power density is usually above 1000 mW.

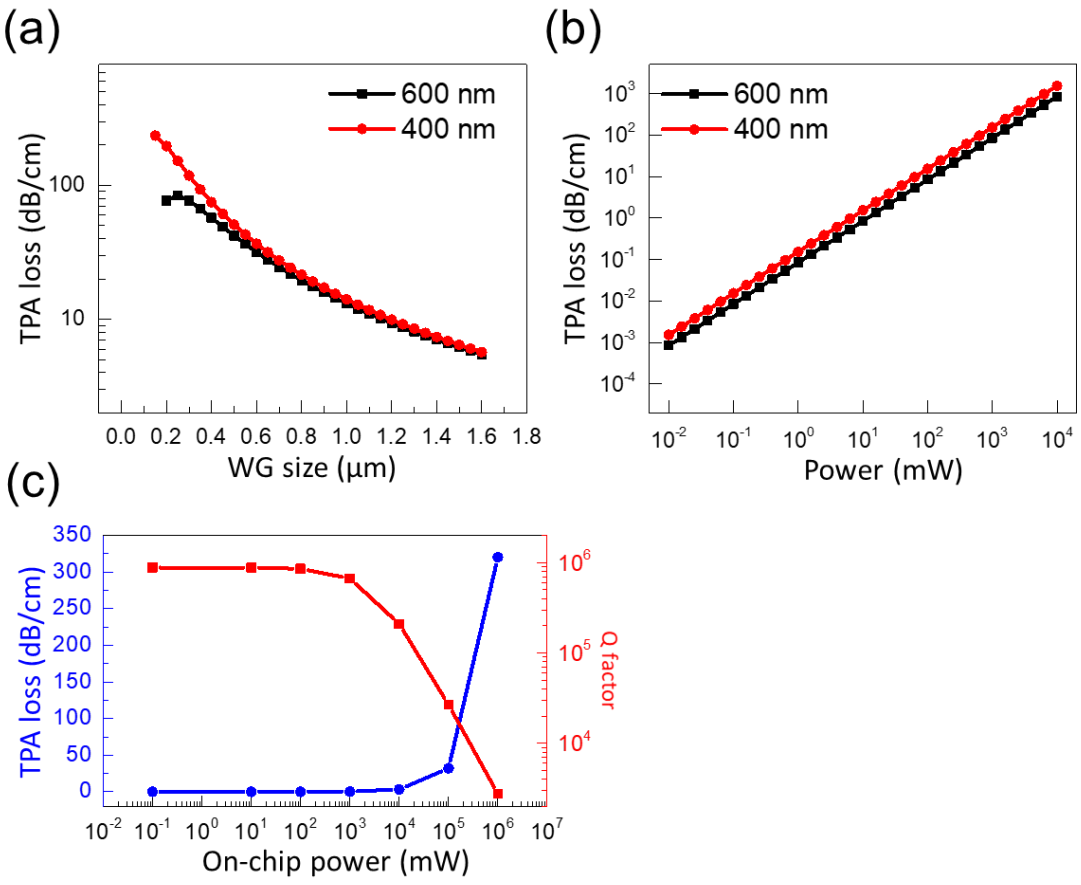

Figure 4-6. (a) Calculated TPA loss vs. waveguide dimensions for GaN waveguides at different wavelengths. (b) Calculated TPA loss vs. incident power for GaN waveguides (dimension of 200 nm × 200 nm) at different wavelengths. (c) Calculated TPA loss (blue curve) and quality factor (red curve) vs. incident power for GaN waveguide using a mode area of 1 μm^2 at a wavelength of 710 nm.

With the calculation results from the previous section, we can further analyze the overall performance of GaN waveguides. At the telecom wavelength (i.e., 1550 nm), the GaN waveguide will have very poor performance mainly due to the large free carrier loss. In contrast, GaN waveguides show much higher performance at the visible wavelength (i.e., 400 – 600 nm). Figure 4-7 shows the calculated loss map of GaN waveguide at 600 nm with a more ideal material quality and low sidewall surface roughness (σ = 0.1 nm). At 600 nm, the total optical loss of GaN waveguide will exceed 10 dB/cm when optical power is larger than 1000 mW. The results indicate that GaN waveguides will perform best for micro waveguide and small power applications such as modulators and inter-chip connections. While for high power applications such as comb generation, second harmonic generation, stimulated Raman scattering, super continuum generation, etc., GaN waveguides can only be implemented below half-bandgap photon energy, i.e., wavelengths > 710 nm, to achieve high performance and low loss.

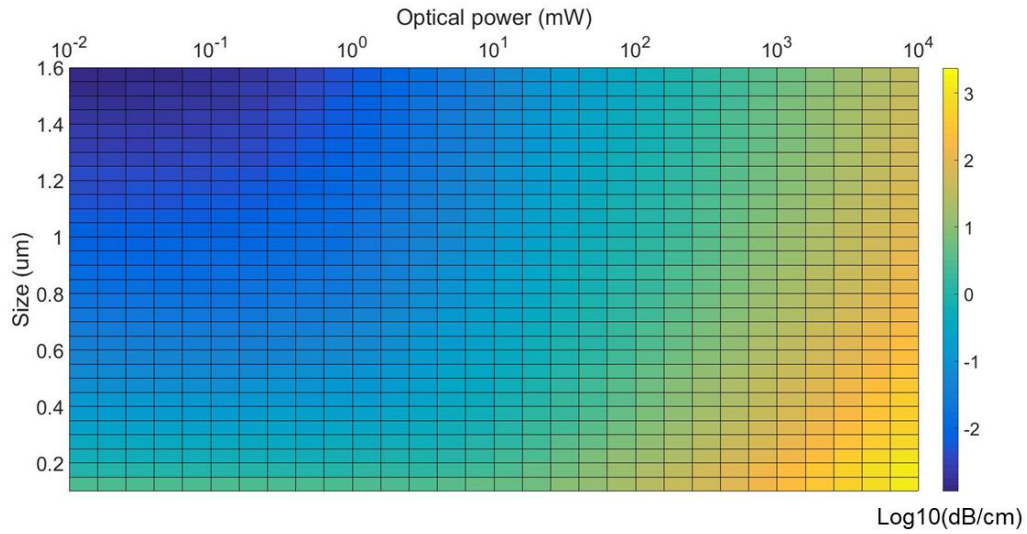

Figure 4-7. Calculated loss map of GaN waveguides at 600 nm in an ideal case, i.e., good material quality (N = 10^{15} cm^{-3}) and small sidewall surface roughness (σ = 0.1 nm). The dashed line in this plot refers to cut off.

We also analyzed a more realistic case for GaN waveguide with moderate material quality $N/\mu=10^3 N_0/\mu_0$, and sidewall roughness σ = 1 nm, and the result is shown in Figs. 4-8(a) and 4-8(b). Due to the n-type conductivity of GaN materials, the free carrier loss dominates at the low incident optical power range, which is very different from Si or InP waveguides where the scattering loss dominates. Therefore, special attention must be paid in controlling the free carrier loss when designing and fabricating GaN waveguides.

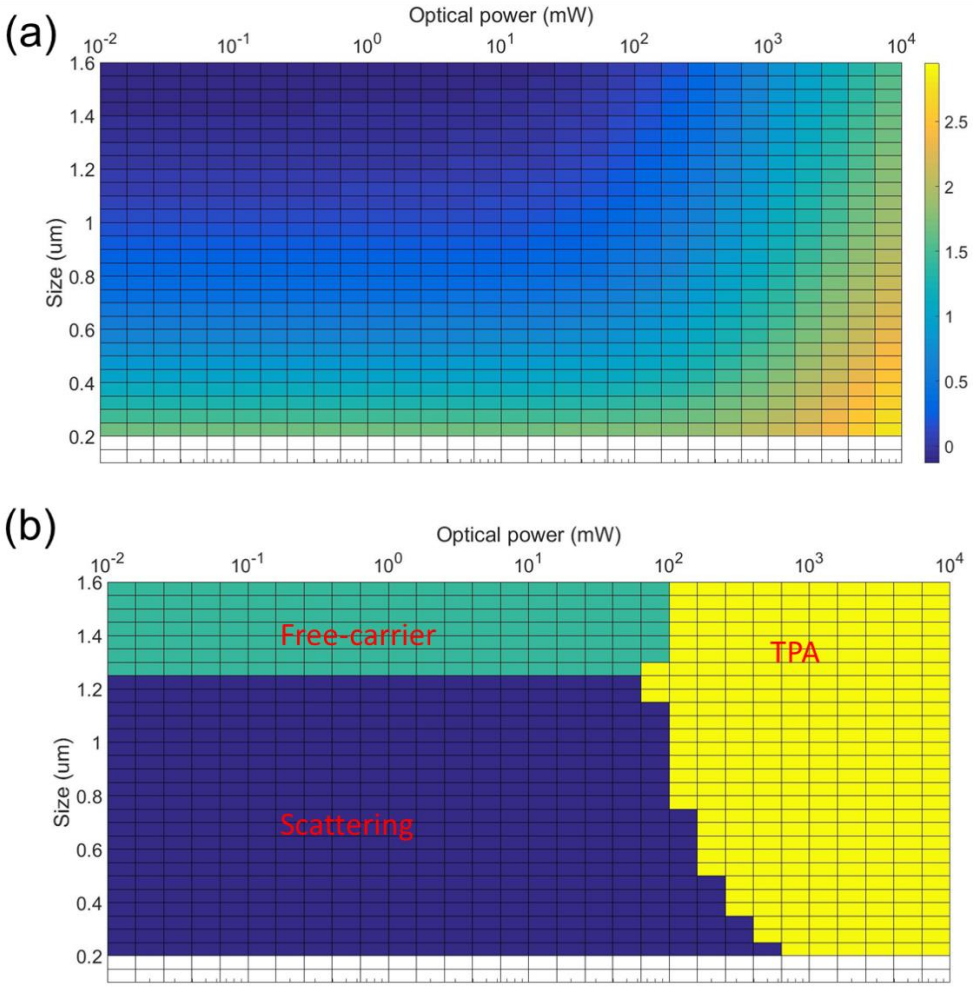

Figure 4-8. (a) Calculated loss map of GaN waveguides at 600 nm in a more realistic case, i.e., moderate material quality ($N/\mu=10^3 N_0/\mu_0$) and sidewall surface roughness $\sigma = 1$ nm. (b) Contributions of different loss mechanisms in this GaN waveguide structure.

The loss map and loss mechanism were also calculated for AlN waveguides as shown in Fig. 4-9. Due to the small concentration of n-type carriers, the free carrier loss is not significant in AlN based waveguide. The results obtained in Figs. 4-8 and 4-9 are supported by experimental results as we shown in the next sections.

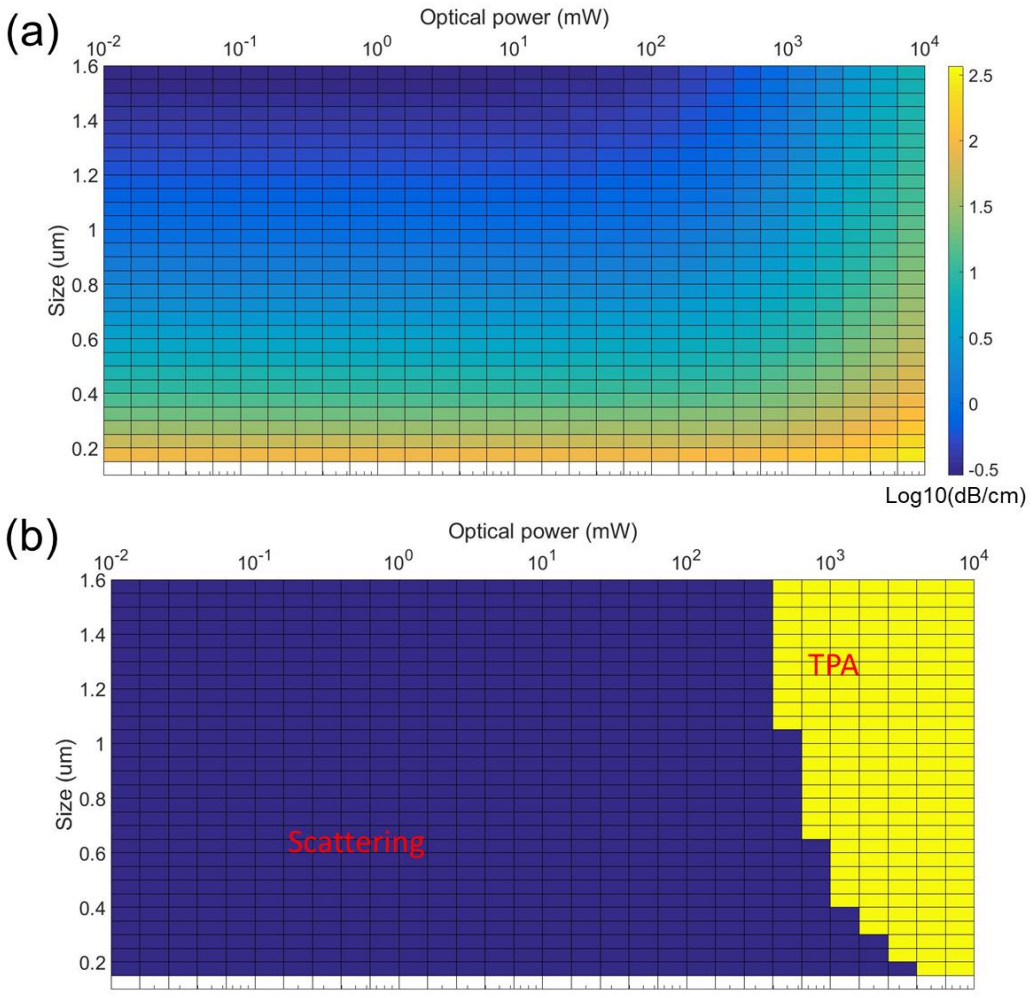

Figure 4-9. (a) Calculated loss map of AlN waveguides at 400 nm in a realistic case, i.e., moderate material quality ($N/\mu=10^3 N_0/\mu_0$) and sidewall surface roughness $\sigma = 1$ nm. (b) Contributions of different loss mechanisms in this AlN waveguide structure.

4.4 Experimental characterizations on III-N waveguides and resonators

Using the process discussed in previous sections, we fabricated the GaN waveguides with 1.5 μm height and width varying from 1.2 μm to 2 μm. The experimental data of waveguides tested in this study with good, decent, and failed performances are shown in Figs. 4-10(a), 4-10 (b), and 4-10 (c), respectively. Testing was performed with 700 nm CW light. For a waveguide with decent performance, only small decay happens

after propagation of millimeters. While for a typical failed waveguide, large decay (> 10 dB/cm) can be observed in less than 1 cm propagation. The low loss waveguide in this study is defined to be waveguides that exhibits < 10 dB/cm loss since such waveguides are widely used in ring resonator fabrications.

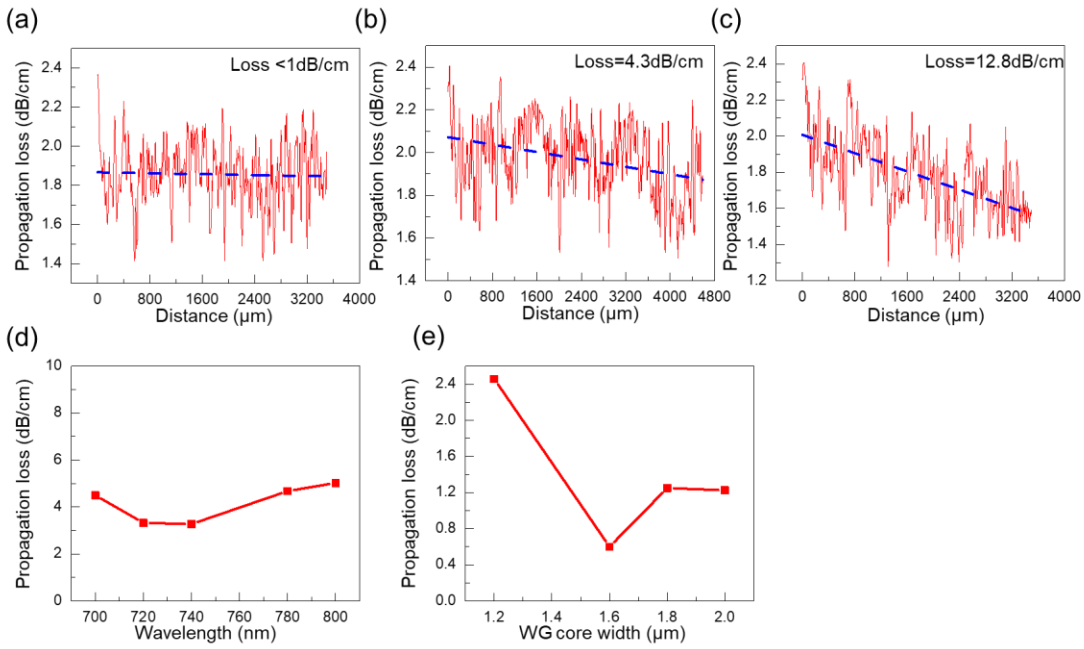

Figure 4-10. (a), (b), and (c) Loss characterization of GaN waveguides with good, decent, and failed performance, respectively. The width for each waveguides are 1.6 μm. (d) Loss vs. wavelengths for the GaN waveguide with 1.6 μm width. (e) Loss vs. waveguide width tested at 700 nm in CW lasing mode.

Figure 4-10(d) shows the waveguide loss as a function of wavelength under CW mode incident light with waveguide width of 1.6 μm. Since the waveguides fabricated in this study are above submicron, they showed very weak wavelength dependence in this wavelength region. The width dependence of optical loss is shown in Fig. 4-10(e), due to the inaccuracy of out scattering characterization method and limited sample length using EBL process, the characterized waveguide loss fluctuates below 2 dB/cm, therefore the

trend is not very clear. In this study, 30 total waveguides were characterized. 70% of the waveguides show optical loss of < 10 dB/cm and 20% exhibit loss of ~ 2 dB/cm. To the best of our knowledge, this value (~ 2dB/cm) is the lowest loss ever reported on GaN-based waveguides [96,97], and are comparable to the performance of state-of-the-art InP and Si waveguides at 1.55 μm. These low loss GaN waveguides are capable to handle various applications such as Mach-Zehnder (MZ) interferometers, MZ modulators, and high-quality ring resonators.

Table 4-1 summarize the optical loss performance of recent studies on GaN waveguides. Overall the reported loss values decreases with decreasing wavelengths, indicating that the dominant loss mechanism for GaN waveguide is the scattering loss, as the free carrier loss will increase with increasing wavelength. Comparing with previous studies [96,97], the GaN waveguides in this work showed the lowest optical loss value (~ 2.5 dB/cm) with comparable waveguide dimensions. Furthermore, the devices in this work was also tested at a shorter wavelength (~ 700 nm). These results clearly show the high potential for GaN waveguides especially for visible and even UV wavelengths, which is currently unattainable for conventional Si or III-V waveguides. Better performance can be expected from GaN waveguides with further optimized material qualities and fabrication processes.

Table 4-1. Previous reports on GaN based waveguides

Loss	Waveguide dimension (Width×Height) in μm	Wavelength (nm)	Ref.
Waveguide loss in channel waveguides			
33.4 dB/cm	3 × 3	1559	Hui et al. (2003) [96]
26, 22 dB/cm	0.73 × 0.625	406, 1550	Sekiya et al. (2015) [98]

20 dB/cm	1 × 0.8	1550	Li et al. (2015) [99]
15.2, 5.9 dB/cm	1 × 0.65	775, 1550	Bruch et al. (2015) [100]
2.5 dB/cm	**1.2 × 1.5**[1]	**700**	**This work**
Waveguide loss in planar or bulk waveguides[2]			
0.61 dB/cm	Bulk	1550	Geiss et al. (2005) [101]
4.2, 0.65 dB/cm	Planar (1.5 μm)	830, 1550	Stolz et al. (2011) [97]
1.9 dB/cm	Planar (1 μm)	632.8	Gromovyi et al. (2014) [102]

1. Waveguide with 2.5 dB/cm loss at 1.2 μm × 1.5 μm dimension is picked in this comparison, lower loss can be obtained at wider width.
2. Thin film thickness is given in the bracket.

The low loss performance from the GaN waveguides can be attributed to the optimized ICP dry etching process that minimizes the sidewall roughness of the devices. The loss variation of the waveguides across the wafer can be attributed to several reasons. Firstly, SiO_2 cracking was observed on some area of the wafer, possibly due to large thermal expansion coefficient difference between SiO_2 and GaN. The cracking of SiO_2 hardmask could result in the damage of waveguide in the device etching steps. Secondly, the mechanical polishing process could cause damage to some waveguides. For the former issue, we can optimize the PECVD deposition process and/or use thinner SiO_2 layers to avoid non-ideality and cracking. For the latter issue, grating couplers can be employed to eliminate the polishing process. Further improvements of the GaN waveguide are expected by optimizing the growth and fabrication process.

In order to verify that TPA loss is the dominated optical loss mechanism for GaN waveguide at the visible spectral range under strong power incidence, we further characterized the waveguide under pulsed laser mode. During the testing, a 100-fs laser pulsed at 82 MHz repetition rate was utilized with operating wavelength of 710 nm. The loss of the GaN waveguide with height of 1.5 μm and width of 2 μm was characterized at

different incident power under both pulsed and CW mode, and the results are shown in Fig. 4-11. Under pulse mode, the optical loss of the waveguide showed a strong dependence on the incident power. In contrast, the optical loss was almost constant under CW model over the measured power range. Since TPA loss is power related, it will increase with increasing incident optical power. In comparison, scattering loss and free carrier loss have less power-dependence. Therefore, under pulsed mode operation, the dominant loss mechanism for GaN waveguide is the TPA loss. While for waveguide under CW mode operation, the peak optical power density is much smaller compared with that in pulsed mode, and we do not observe significant power-dependence.

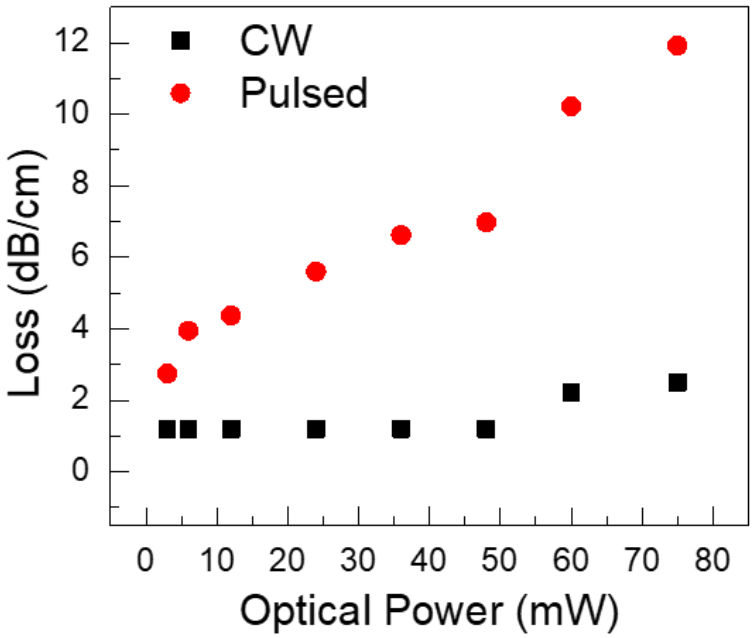

Figure 4-11. Loss vs. incident power for the GaN waveguides when the laser is in CW and pulsed mode.

The propagation loss of AlN waveguides can be identified by similar setup. The characterized results indicate that the propagation loss in the near-visible (~800 nm) is < 2 dB/cm and the loss within visible spectrum is 12 dB/cm. The GaN and AlN based

resonators were also fabricated within ASU and characterized in USC and UCLA. The typical *Q* factor of GaN disk resonators was identified to be 40,000 (loaded *Q*, radius r = 80 μm, height h = 5 μm), and the *Q* factor of AlN ring resonator was measured to be 400,000 (loaded *Q*, W×H = 2.5 μm × 0.52 μm).

In a short conclusion, we performed a comprehensive study on the optical loss mechanisms in III-N waveguides at visible spectral range. The results showed that the free carrier loss dominates for GaN waveguides when under low power operation, which is different from traditional InP or Si waveguides working at 1550 nm where scattering loss dominates, while the AlN exhibit neglectable free carrier loss. Under high power operation, TPA loss starts to dominate for GaN waveguides. A high performance III-N-on-sapphire waveguide was fabricated and characterized, and the experimental results are consistent with the theoretical findings. A low optical loss ~ 2 dB/cm was achieved on the GaN and AlN waveguide. The results and fabrication processes developed in this work pave the way for the development of III-nitride integrated photonics in the visible and potentially ultraviolet spectral range for nonlinear optics and quantum photonics applications.

4.5 Semi-analytical model for impurity induced scattering loss

For traditional WGs working at IR wavelengths, wave propagation losses are mainly contributed by sidewall scattering, and they can be reduced by implementing geometries [103] that minimize the overlap between modes and scattering non-idealities. This design strategy is feasible for most of WG materials such as SiN_x [103]. However, there is another complicating factor for III-N materials grown on foreign substrates such as sapphire: high defect densities. For example, the metalorganic chemical vapor deposition (MOCVD) grown III-N thin films on sapphire exhibit high density of threading

dislocations (TDs) over 10^{19} cm^{-2}, and density of TDs will be even higher for sputtered films. Therefore, for III-N WGs, in addition to the sidewall scattering loss, internal defect induced scattering loss is also be of crucial importance to WG performance. Furthermore, as Rayleigh's law suggests, the scattering cross-section is proportional to λ^{-4}, indicating that small non-idealities (crystalline defects) will cause higher scattering loss in UV-visible wavelengths than in IR wavelengths. Since III-N materials are commonly employed as light-emitting/WG materials in UV-visible spectrum, III-N optical devices are expected to be more vulnerable to defect induced scattering losses.

There are two main types of defect induced WG losses: absorption-related loss and scattering-related loss. Recent studies have revealed different loss mechanisms in III-N optical devices due to crystalline defects including defect absorption [95], anisotropic non-ideal wet etching [104], free carrier absorption [40], and two-photon absorption [38]. However, the internal defect induced scattering loss is still not clear in these devices and demands rigorous investigations due to its significance in III-N WGs. In this work, we propose a semi-analytical method based on the volume current model (VCM) to calculate optical scattering losses from defects in AlN WGs. In comparison with previous models and analysis [105], in which the analysis was made within the scenario of point defects scattering in homogeneous medium, this work considered complex defect geometries and WG optical confinements. The model is ready to be applied to other III-N materials (GaN, AlGaN), if different index settings are utilized accordingly. The obtained results will be compared with other defect related loss mechanisms, and with previous experimental results.

This section is organized as following: firstly the numerical method implemented in this work will be presented. Then, the scattering properties of a single threading dislocation will be shown; additionally, we extent the discussion into the loss properties of a more practical case where threading dislocation arrays will be considered. The TD induced scattering loss will be compared with sidewall scattering loss and discussions will be made. At last, we compare the scattering induced loss with other defect related loss mechanisms, and the limitation of this model will also be discussed.

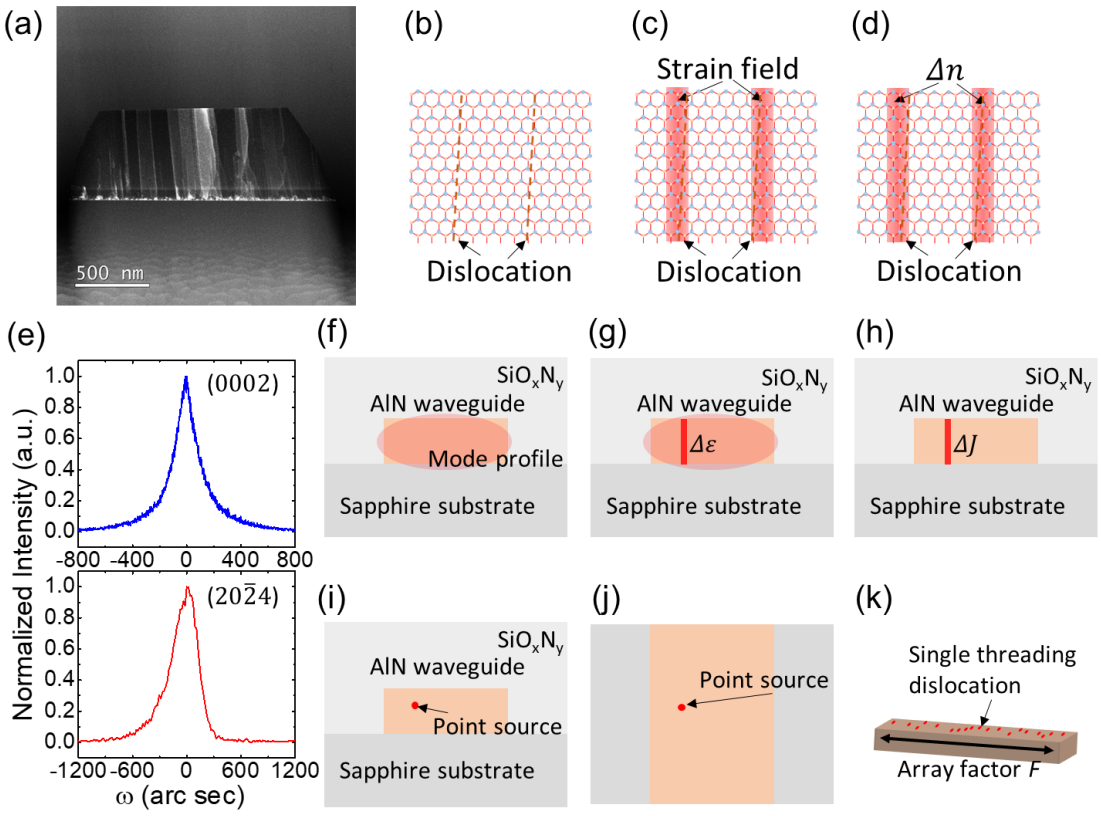

Figure 4-12. (a) TEM cross-section image of AlN WGs. (b)–(d), the dielectric equivalent of threading dislocation for scattering analysis, see main text for detailed description. (e) Typical XRD data of AlN thin film grown on sapphire substrate by MOCVD, the threading dislocation density can be estimated using Eqs. (4-3) and (4-4). (f)–(k), the procedures to obtain the threading dislocation induced optical scattering loss, detailed description can be found in main text.

The transmission electron microscopy (TEM) image and AlN WG is depicted in Figure 4-12(a). The AlN film was grown on sapphire substrates by MOCVD, where trimethylaluminum (TMAl) and ammonia (NH_3) were used as precursors for Al and N, respectively. The details about the fabrication process of AlN WGs can be found elsewhere [106]. High density of TDs along c-axis can be clearly observed in AlN as shown in Fig. 4-12(a). It should be noted that the defect considered in this work is TD due to its large population in III-N. Other types of defects such as point defects and grain boundaries can also be analyzed using the proposed model. In this work, VCM is implemented to analyze the scattering properties [86,103]. A closed form of dyadic Green's function is derived for far-field response of point source excitation inside WG. This dyadic Green's function is implemented together with proper array factor [86] to estimate TD induced scattering loss inside AlN WGs. The model proposed in this research can be easily converted for different types of defects in different material systems. To model TD induced scattering loss properly, the distribution of TDs should be converted into a corresponding dielectric distribution, which in turn determines the scattering objectives. This task can be accomplished by making the following physical approximations. In the vicinity of TDs, the abnormal atom arrangements [Fig. 4-12(b)] result in strain fields near its neighboring sites [Fig. 4-12(c)]. This in turn leads to the photoelastic effect that causes a change of permittivity $\Delta\varepsilon$ and thus Δn as indicated in Fig. 4-12(d). According to [105], $|\Delta\varepsilon| = 2.0$ can be served as a typical order-of-magnitude estimate.

In this work, for simplicity, TDs are modeled by randomly (but with a correlation in between) distributed cylinders that perpendicular c-plane of sapphire substrate. Although the dimensions of TDs' cross-sections are in atomic scale, the strain field can

extend to its neighboring sites, resulting in a lager effective cross-section. In this work, we assume that the radius of each "cylinder" is 0.5 nm [107]. The density of TD with screw (N_S) and edge (N_E) types can be estimated bawd on the X-ray diffraction (XRD) rocking curves (RC) of AlN thin films on (0002) plane and ($20\bar{2}4$) plane using Eqs. (4-3) and (4-4), respectively, where β is the full-width-half-maximum (FWHM), b is the length of Burger's vector [108,109]. A typical XRD RC of AlN thin film grown by MOCVD is shown in Fig. 4-12(e), in which the FWHM of (0002) and ($20\bar{2}4$) RCs are 194.1 and 313.8 arc sec, respectively, corresponding to TD density on order of of ~10^8 cm^{-2}.

$$N_S = \frac{\beta_S^2}{4.35|b_S|^2} \tag{4-3}$$

$$N_E = \frac{\beta_E^2}{4.35|b_E|^2} \tag{4-4}$$

The VCM is utilized to compute scattering loss contributed by TDs, the method is also commonly used in the analysis of sidewall scattering loss in WGs [86,103]. Since the dyadic Green's function associated with VCM derived in this work has a different format compared with previous studies [86,103], the derivation of VCM will be briefly revisited for complicity. To investigate the scattering loss in dB/cm, the first step is to compute modes within optical WG [Fig. 4-12(f)]. More specifically, the WG geometry in this study is AlN grown/sputtered on sapphire, and the cladding layer is SiO_xN_y deposited by plasma-enhanced chemical vapor deposition (PECVD) in order to match the refractive index of sapphire. The index changes consequent from TDs can be considered as a weak perturbation, and the field distribution of modes is assumed to be almost unaltered. To satisfy wave equation, the change in refractive index will contribute a volume current

density at the same location as shown in Figs. 4-12(g) and 4-12(h). According to [20], the amplitude of this volume current density $\vec{J}$ is governed by:

$$\vec{J}(\vec{r}) = -i\omega\Delta\varepsilon(\vec{r})\vec{E}(\vec{r}) \tag{4-5}$$

where ω is the photon angular frequency, $\Delta\varepsilon$ is the change of permittivity, $\vec{E}$ is the field intensity obtained by solving WG modes. The loss from a single TD can be analyzed by calculating the radiated power from this volume current source by dyadic Green's function. The dyadic Green's function in the far-field can be analytically derived by implementing method of stationary phase in two dimensions given by Eqs. (4-6) and (4-7), where intermedium components are given by Eqs. (4-8)–(4-16). $\overline{G}_{21}(\overline{G}_{23})$ indicates the dyadic Green's function when source is located within medium 2 and the field point in medium 1(3). $\overline{G}_{11}$ and $\overline{G}_{13}$ are the dyadic Green's functions when the point source is located at the sidewall, formats of $\overline{G}_{11}$ and $\overline{G}_{13}$ can be found in [86] and [103]. Although Eqs. (5-6) and (5-7) are originally derived in this work, to keep it consistent with previous studies on sidewall scattering, all notations in Eqs. (4-6)–(4-16) are kept the same as [86].

$$\overline{G}_{21}(\vec{r}_c,\vec{r}_c') \approx \frac{e^{i\vec{k}_{1+,0}\cdot(\vec{r}_c-\vec{r}_c')}k_{1zc,0}^2[\bar{C}_M\frac{A^{TE}}{M_2^{TE}}+\bar{C}_{Np}\frac{A^{TM}}{M_2^{TM}}]e^{i(k_{1zc,0}-k_{2zc,0})d_1}}{4\pi(z_c-z_c')k_1|k_{s0}|^2k_{2zc,0}} \tag{4-6}$$

$$\overline{G}_{23}(\vec{r}_c,\vec{r}_c') \approx -\frac{e^{i\vec{k}_{3-,0}\cdot(\vec{r}_c-\vec{r}_c')}k_{3zc,0}^2[\bar{C}_M\frac{B^{TE}}{M_2^{TE}}+\bar{C}_{Nm}\frac{B^{TM}}{M_2^{TM}}]e^{-i(k_{3zc,0}-k_{2zc,0})d_2}}{4\pi(z_c-z_c')k_3|k_{s0}|^2k_{2zc,0}} \tag{4-7}$$

$$A^{TE} = [e^{i(k_{1zc,0}-k_{2zc,0})z_c'} + e^{ik_{2zc,0}(z_c'+2d_2)+ik_{1zc,0}z_c'}\hat{R}_{23}^{TE}]\hat{T}_{21}^{TE} \tag{4-8}$$

$$A^{TM} = \left[e^{i(k_{1zc,0}-k_{2zc,0})z_c'} + e^{ik_{2zc,0}(z_c'+2d_2)+ik_{1zc,0}z_c'}\hat{R}_{23}^{TM}\right]\hat{T}_{21}^{TM} \tag{4-9}$$

$$B^{TE} = [e^{-i(k_{3zc,0}-k_{2zc,0})z_c'} + e^{-ik_{2zc,0}(z_c'+2d_1)-ik_{3zc,0}z_c'}\hat{R}_{21}^{TE}]\hat{T}_{23}^{TE} \tag{4-10}$$

$$B^{TM} = [e^{-i(k_{3zc,0}-k_{2zc,0})z_c'} + e^{-ik_{2zc,0}(z_c'+2d_1)-ik_{3zc,0}z_c'}\hat{R}_{21}^{TM}]\hat{T}_{23}^{TM} \quad (4\text{-}11)$$

$$\bar{C}_{Np} = [\vec{k}_{n+} \times (\vec{k}_s \times \vec{z}_c)/k_n][\vec{k}_{m-} \times (\vec{k}_s \times \vec{z}_c)/k_m] \quad (4\text{-}12)$$

$$\bar{C}_{Nm} = [\vec{k}_{n-} \times (\vec{k}_s \times \vec{z}_c)/k_n][\vec{k}_{m+} \times (\vec{k}_s \times \vec{z}_c)/k_m] \quad (4\text{-}13)$$

$$\bar{C}_M = (\vec{k}_s \times \vec{z}_c)(\vec{k}_s \times \vec{z}_c) \quad (4\text{-}14)$$

$$M_2^{TE} = [1 - R_{23}^{TE}R_{21}^{TE}e^{2ik_{2zc}(d_2-d_1)}]^{-1} \quad (4\text{-}15)$$

$$M_2^{TM} = [1 - R_{23}^{TM}R_{21}^{TM}e^{2ik_{2zc}(d_2-d_1)}]^{-1} \quad (4\text{-}16)$$

The electric field can be computed using Eq. (4-17) when dyadic Green's function is obtained using Eqs. (4-6)–(4-16). The total radiated power can be obtained by integrating the Poynting vector in the far-field, where the ensemble average of Poynting vector in the far-field is given by Eq. (4-18).

$$\vec{E}(\vec{r}_c) = i\omega\mu \iiint \overline{G}(\vec{r}_c, \vec{r}_c') \cdot \vec{J}(\vec{r}_c')\mathrm{d}V' \quad (4\text{-}17)$$

$$P = \oiint \vec{S} \cdot \vec{r}\mathrm{d}A \quad (4\text{-}18)$$

To calculate the ensemble average of far-field Poynting vector, the same array factors can be implemented as [86] given by Eqs. (4-19) and (4-20), where σ is the equivalent roughness, L_c is the correlation length, and Ω is the spatial frequency. The scattering objective is assumed to be locating at the radiation location where average radiated power is obtained. The effective roughness σ^2 can be obtained by multiplying dislocation density (*D.D*) in cm^{-2} with WG width in the unit of μm.

$$\tilde{R}(\Omega) \approx \frac{2\sigma^2 L_c}{1+L_c^2\Omega^2} \quad (4\text{-}19)$$

$$\frac{P_{rad}}{L} = \int_0^{2\pi}\int_0^{\pi}(\vec{S} \cdot \vec{r})\tilde{R}(\beta - k_0 n_{clad}\vec{r} \cdot \vec{z})r^2 sin\theta d\theta d\phi \quad (4\text{-}20)$$

$$\sigma^2 = D.D. \times W \times 10^{-11} \quad (4\text{-}21)$$

The spatial distribution correlation of TDs inside III-N materials have been investigated by different groups, and the correlation length is varied from 50 nm [110] to a few microns [111]. The correlation length has weak influence on the scattering loss when

it's sufficiently large [86]. Therefore, for simplicity, the correlation length used in this work is set as 100 nm.

Prior to the investigations on scattering properties of TDs inside WGs, it is beneficial to initiate the discussion on the scattering properties of TDs inside a homogenous medium. Figure 4-13(a) depicts the coordinate system used in this work, in which the wave is propagating along y-direction and the thin film layer is grown along z-direction. Sidewall of waveguide is supposed to be defined by dry etching processes perpendicular to x-direction. More specifically, the z-direction corresponds to c-axis of AlN (or GaN) and sapphire. Under same excitation condition, the ratio between TD/sidewall scattered power and TE/TM scattered power versus TD location (x-axis) are shown in Fig. 4-13 (b). A noteworthy feature is that TM excitation is intrinsically more radiative than TE excitation, indicating higher scattering loss from TM modes. The maximum scattered power of TDs are ~140 and ~60 times higher than sidewall for TM and TE modes, respectively, as the field intensity decays from the center. The significant difference between TM/TE scattered power can also be verified by their far-field distribution in Fig. 4-13(c), where the far-field pattern can be well understood by combining anisotropic dipole radiation [86] with linear dipole array theory [112].

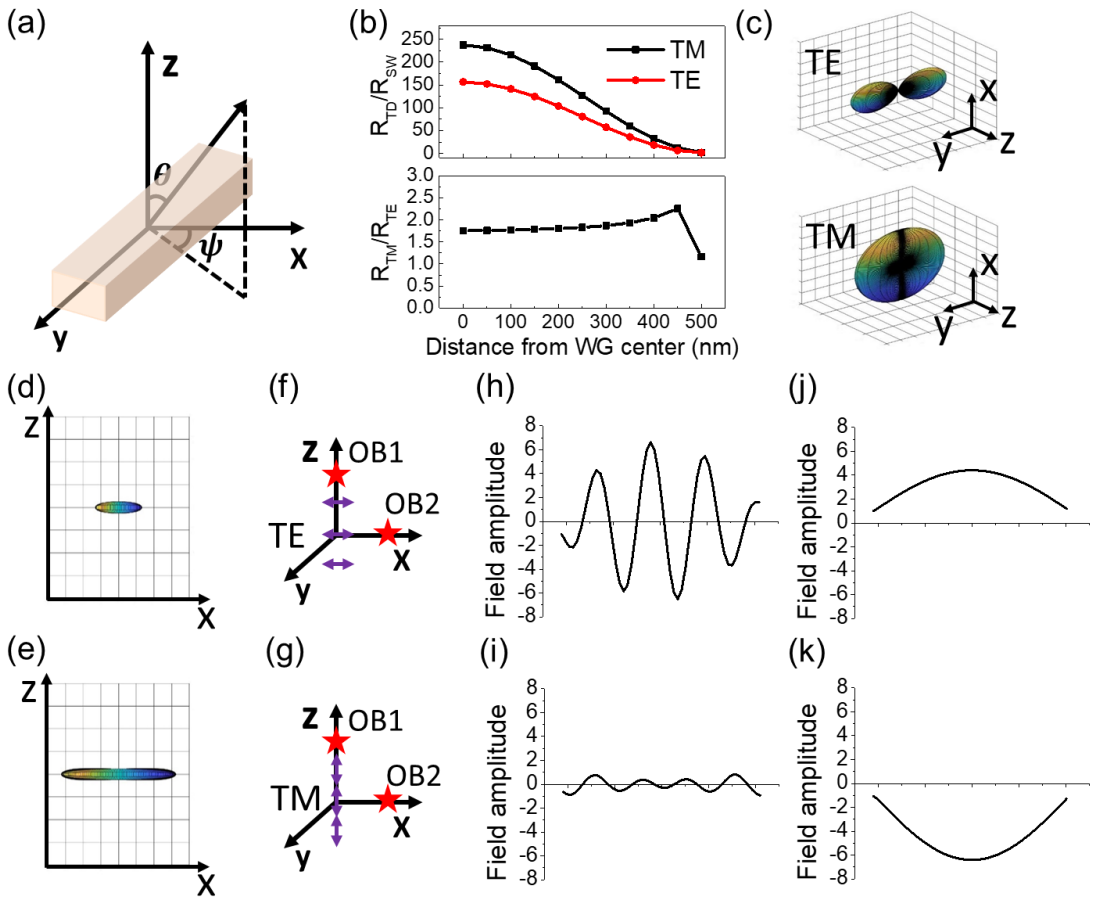

Figure 4-13. (a) Coordinate system implemented in this study. (b) Threading dislocation scattered power versus sidewall non-ideality scattered power R_{TD}/R_{SW} for TE and TM mode, and the scattered power ratio between TM and TE mode R_{TM}/R_{TE}, when no WG confinement is considered. (c) Far-field power distribution of the scattered field for TE and TM excitation. (d), (e) WG cross-section view of scattered power distribution for TE and TM mode, respectively. (f), (g) Schematic for the dipole arrangement and OB points for TE and TM modes, respectively. (h)–(k) Field intensity versus dipole location for TE and TM dipoles at different observation points.

One of the most important features obtained from this configuration is the highly anisotropic scattering property. Figures 4-13(d) and 4-13(e) show the far-field distribution in x-z plane for TE and TM modes, respectively. For TE modes, the radiated power along x-direction is ~5 times higher than that along z-direction for TE mode and for TM mode it is ~15 times higher. To explain this strong anisotropy, two observation (OB) points can be

placed at z-axis and x-axis in the far-field as shown in Figs. 4-13(f) and 4-13(g). Figs. 4-13(h)–4-13(k) show the field amplitude for each individual point source location in TE/TM modes. For OB point at z-axis, field amplitude is oscillating due to the phase difference between dipoles at different locations. Therefore, the total radiated power of "linear array" is minimized as the contribution from individual dipoles canceled each other. While for OB point at x-axis, in the far field, each dipole exhibits nearly identical phase. Therefore, the total radiated power of array is maximized. Noting that the dyadic Green's function only allows the existence of one pair of WG boundaries [86], it's feasible to keep the sidewall and omit the upper and lower boundaries [86], since most of the scattered power interacts with boundaries vertical to x-axis. In the next we will discuss more about this assumption and possible limitations.

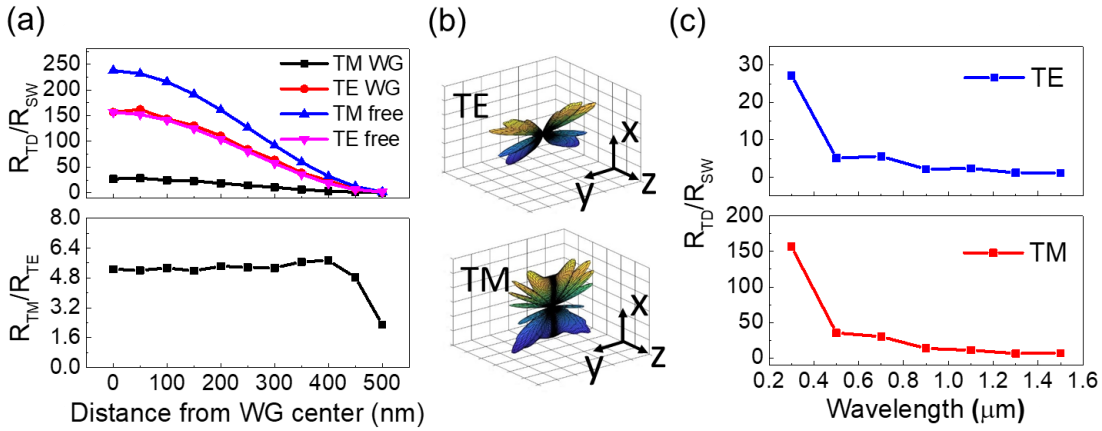

Figure 4-14. (a) Threading dislocation scattered power versus sidewall non-ideality scattered power R_{TD}/R_{SW} for TE and TM mode, and the scattered power ratio between TM and TE mode R_{TM}/R_{TE}, when WG confinement is implemented. (b) The wavelength dependence of scattered power ratio. (c) Far-field power distribution of TE and TM excitation with WG confinement effect.

Figure 4-14 shows the scattering properties with WG confinement of a single TD by activating one pair of boundaries vertical to x-axis. R_{TD}/R_{SW} for TE/TM modes and

power ratio between TE/TM modes for different locations of TDs are shown in Fig. 4-14(a). Due to the waveguiding effect, the scattered power becomes smaller with optical confinement as part of scattered power will be guided within WGs. Scattered power ratio between TM and TE mode is also higher than homogeneous situation in Fig. 4-13(b). This is because most of the TE scattered power is directed towards y-axis in guided mode. On the other hand, for TM mode, significant amount of scattered power travels along x-axis interacting with sidewall, leading to a ~10 times higher scattered power than TE mode at the WG center. Figure 4-14(b) depicts the far-field pattern of scattered power. Compared with Fig. 5-13(c), the field in y direction disappears due to the waveguiding effect, and the amplitude oscillation can be observed along x-axis due to constructive/deconstructive interferences from two WG boundaries. Figure 4-14(c) shows R_{TD}/R_{SW} as a function of wavelength. The ratio decreases with increasing wavelength, indicating that TDs induced scattering loss becomes more significant in short wavelength region.

Results from Fig. 4-14 can provide two important takeaways for real applications. Firstly, for a wide variety of nonlinear optical applications, controlled anomalous dispersion is required. TM mode exhibits better dispersion properties under certain circumstances [113], especially for those applications in highly dispersive region. Since TM modes are more vulnerable to TDs, high material quality is of crucial importance in III-N optical devices, which in turn requires good epitaxial growth by MOCVD. Secondly, for the applications of harmonic generation [30,31], parametric conversion [114], supercontinuum generation [42], and comb generation, the spectrum can be as broad as one or several octaves, which may result in a large optical loss difference between IR and UV-

visible light. This has been supported by many recent studies on AlN based optical devices and will be discussed more in the next.

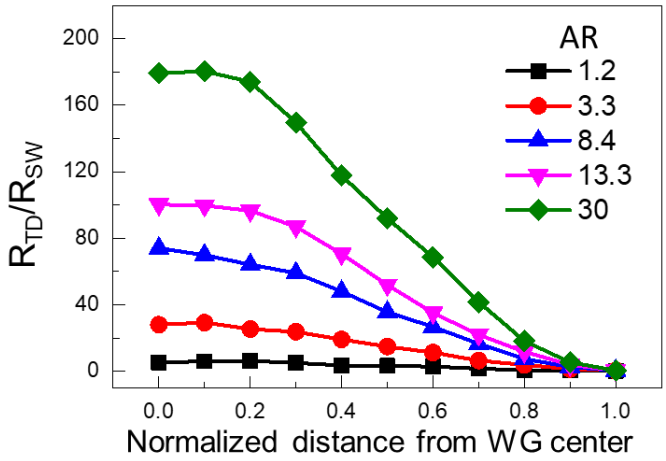

Figure 4-15. The scattered power ratio R_{TD}/R_{SW} for HAR WGs at different aspect ratios.

In addition to normal WG geometries, the "high-aspect-ratio" (HAR) design has recently received growing attentions due to its capability of reducing sidewall scattering loss [103]. HAR design stretches the mode profile in the lateral dimension, which in turn minimizes the interaction between modes and sidewall impurities with single mode properties maintained. Propagation loss as low as 0.1 dB/m has been reported [103] using SiN WGs on SiO_2. For III-N materials, material quality becomes worse with reducing film thickness, which result in poor surface roughness [115]. Although traditional bottom-up approach cannot satisfy the surface roughness requirement to make III-N HAR WGs, it's still possible to tackle this problem by up-bottom approaches using selective wet etching [30]. Figure 4-15 shows the R_{TD}/R_{SW} versus TD location at different aspect ratio. When increasing the aspect ratio (AR) from 1.2 to 30, R_{TD}/R_{SW} increases from ~5.5 to ~650, the increasing R_{TD}/R_{SW} can be well understood by noting that R_{SW} is rapidly reduced by increasing AR, while the TDs are inside WGs thus exhibit weak geometry dependence,

which result in weak dependence of R_{TD} on AR, therefore, R_{TD}/R_{SW} increases rapidly as the AR increases. The result shown in Fig. 4-15 also suggests that the performance of HAR WG exhibits strong material quality dependence.

The loss in dB/cm can be obtained by applying an array factor given in previous section. Figures 4-16(a) and 4-16(b) show the contour plots of optical loss parameters versus waveguide dimensions for TE and TM mode, respectively. The loss in dB/cm can be obtained by multiplying the loss parameters with $\sigma^2 \times \Delta\varepsilon^2$. Higher loss can be observed for TM mode, which is consistent with the conclusion in previous section. The minimum scattering loss is obtained in the HAR region, and the optical loss is reduced by reducing WG height. This is because the enhanced optical confinement in vertical direction squeezes the mode outside WG, and thus reduces the effective current density in TDs and the optical loss. Such observation is similar to the "squeeze out region" defined in [103]. When WG size becomes small in both dimensions (in the bottom-left corner), minimum loss can also be obtained, but the mode is squeezed in both vertical and lateral directions. It is also worth mentioning that TM modes exhibits weaker width dependence comparing with TE modes. The physical mechanism is that when the width increases, more scattered power from TE modes can be guided by WGs, leading to a smaller scattering loss. However, for TM mode, the scattered power is largely directed towards sidewall, and the scattering loss cannot be significantly reduced even with the enhanced waveguiding effect.

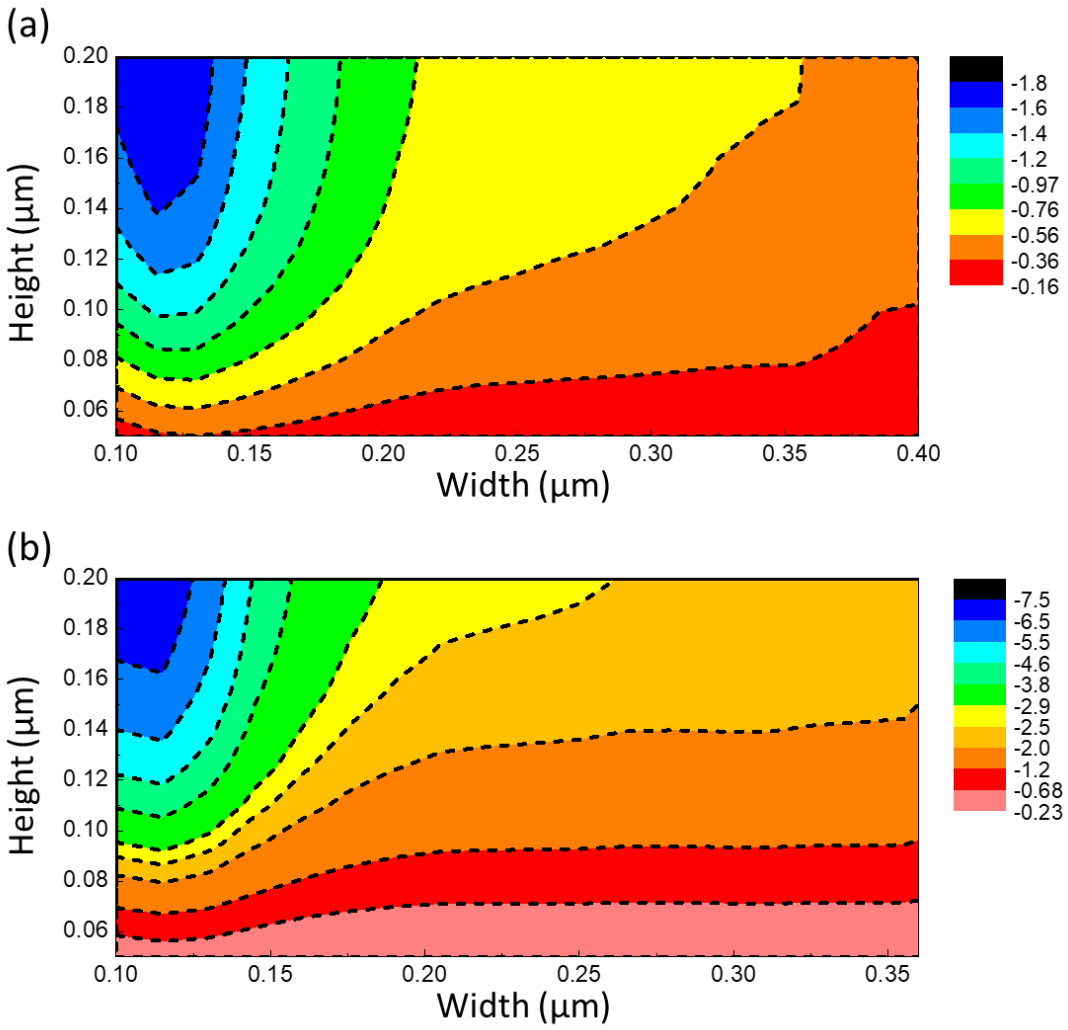

Figure 4-16. (a) The loss map for TD induced scattering loss for TE mode excitation. (b) Same plot for TM mode excitation.

Based on previous discussions, six important WG designs are proposed and compared, whose WG dimensions and typical applications are also summarized in Table 4-2. Figures 4-17(a) and 4-17(b) show the ratio between the TD scattering loss and the total loss, and the total loss in dB/cm for the six cases, respectively. Typical TD densities by different growth methods are provided in Table 4-3. For MOCVD grown devices, TDs contribute to a scattering loss less than 10%, this is supported by recent report on AlN high Q resonator in UV spectrum [27]. When the AlN is sputtered on sapphire substrates with a

subsequent annealing process, a higher TD density can be expected, which can lead to higher TD induced optical losses. The typical annealing temperature for AlN on sapphire is above 1000℃ [116]. These high temperatures are unacceptable especially when WGs are fabricated at the back-end of process flow. The annealing step (or MOCVD re-growth) itself can deteriorate or destroy other electronic or active optical devices. As a result, in some applications, sputtering without annealing is more realistic, where the TD densities are expected to be even higher and the loss is going to be larger. Another noteworthy scenario is the AlN sputtered on SiO_2, which has the potential to be CMOS compatible [117]. However, due to the lack of crystalline arrangement, it's difficult to use TD density to describe the abundancy of defects. As it's reported in [118,119], a brute estimation on TD density is 10^{11}-10^{12} cm^{-2} according to Eqs. (4-3) and (4-4), but one should keep in mind that real defect density will be more excessive, because of the contribution from point defects and grain boundaries. Therefore, the total defect induced scattering losses will be even higher than what we estimated from this model.

Table 4-2. Six notable WG designs and their corresponding geometries.

Case	WG design	Width (μm)	Height (μm)	Typical application
1	Single mode, TE	0.2	0.1	Modulators, interferometers, sensors
2	Single mode, TM	0.2	0.1	
3	High aspect ratio	0.4	0.05	Low loss waveguides, high Q resonators
4	High aspect ratio	0.8	0.025	
5	Large core, TE	1	0.5	Low loss waveguides, high Q resonators
6	Large core, TM	1	0.5	

In short, TM modes are more vulnerable to TD induced loss. Traditional single mode WG geometry shows good tolerance to TDs but the total loss is high in UV region. This means that such geometry might not be a good candidate for real applications, which

are consistent with previous reports from [119]. HAR WGs and large core WGs show better performance in terms of their total losses but also exhibit stronger dependences on TD density. Therefore, for single mode applications in short wavelengths, HAR design is more competitive compared with traditional single mode WG geometry. However, as a trade-off, III-N HAR design would require a top-down approach, which demands complicated fabrication processes. For other high *Q* resonator applications [30] (quantum optics, nonlinear optics), large core multimode WGs are required, in which the WG geometry has the strongest dependence on crystalline quality, and thus requires good MOCVD growth.

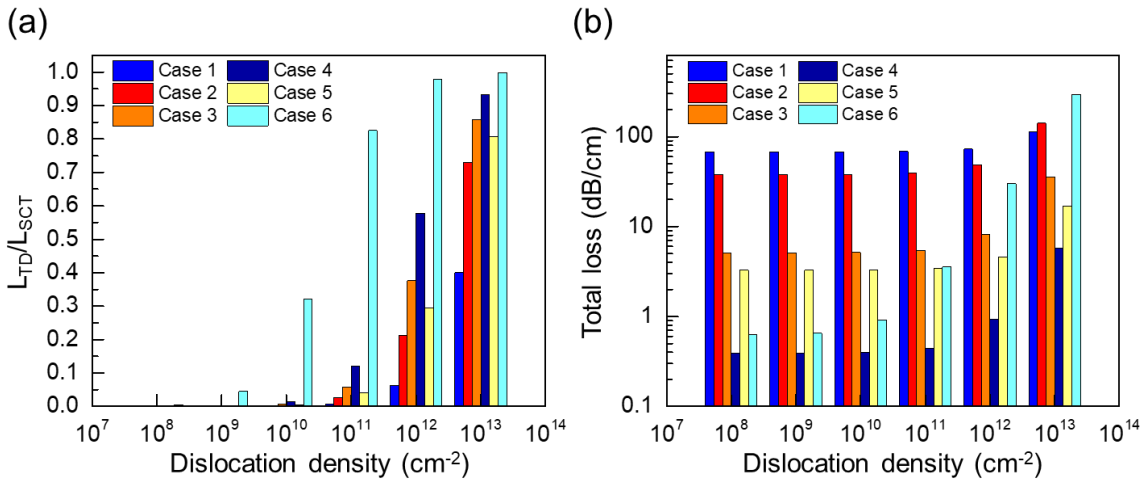

Figure 4-17. (a) The ratio between TD induced scattering loss and total loss versus dislocation density for six noteworthy WG designs. (b) The total loss in dB/cm versus dislocation density.

Table 4-3. Typical dislocation density for AlN thin film grown by different methods

Epi-structure	**Dislocation density (cm^{-2})**
AlN grown on sapphire by MOCVD	10^8-10^9
AlN sputtered on sapphire (w. annealing)	~10^{10}
AlN sputtered on SiO_2 (w. annealing)	~10^{11}-10^{12}
AlN sputtered on SiO_2 (w/o. annealing)	>10^{13}

Since the loss estimation model proposed in this work is based on a scattering approach, active electron transitions (one/two photon absorption loss) are not involved. It's necessary to briefly investigate other loss mechanisms to clarify the applicable realistic scenarios of this model. Loss mechanisms that result in a positive imaginary part of refractive index are related to electron transitions, including free carrier absorption, one photon (defect) absorption, and two photon absorption.

As shown our previous report [40], free carrier loss can be well estimated by the Drude model. In GaN, the abundancy of nitrogen vacancies [120] provide large density of free carriers on order of 10^{18} [40], leading to a free carrier loss on order of 0.1-1 dB/cm depending on material qualities and operating wavelengths. In AlN, the free carrier density is several orders of magnitude lower than in GaN, which result in a negligibly free carrier loss. For defect absorptions, [121] and [95] reported the absorptive detect levels for GaN and AlN, respectively. In GaN, deep energy levels contribute to electron transitions in the yellow spectral region; while for AlN, multiple channels are present at the same time including shallow donors (SD), Al vacancies, and O substitutions.

Then, the dominant defect related loss mechanisms will be discussed in GaN and AlN. In the long wavelength region, propagation loss in GaN is dominated by sidewall scattering and free carrier loss [40]. This observation is supported by numerous reports on GaN disk/ring resonators as their *Q* factors are capped on order of 10^4 [30]. In the short wavelength region, the losses are impacted by both the TD induced scattering loss and the free carrier loss, since a higher TD density is usually accompanied with a strong n-type conductivity [122].

However, free carrier loss is not the major loss mechanism in AlN due to the lack of conductivity. For MOCVD grown AlN WGs, in the short wavelength region, using the geometry parameters in a recent study [123] in UV-visible spectrum wavelength, by assuming L_c = 100 nm, the corresponding sidewall roughness is 3 nm, noting that the state-of-the-art ICP etching process can only provide a minimal roughness in this range, it is convincible to conclude that for MOCVD grown AlN, in the short wavelength, the dominated optical loss mechanism is still sidewall scattering, such conclusion can also be verified by another recent research activity on AlN ring resonator [27] where the *Q* factor can reach 10^5. For sputtered AlN, in the short wavelength, both defect absorption and defect induced scattering loss are important. As a result, the typical loss within this spectrum wavelength is on order of 15 dB/cm.

For MOCVD grown and sputter AlN WGs (or resonators), in the long wavelength region, the small photon energy is insufficient for electron transition between defect states, therefore, the influential mechanism is the TD induced scattering loss. The state-of-the-art MOCVD grown AlN ring resonator in IR exhibits intrinsic *Q* factor above 10^6, while the *Q* factors of sputtered AlN rings are in the range of mid 10^5 due to the large density of defects.

It also worth noting that regarding III-N disk resonators, the anisotropic wet etching during undercut process could lead to additional roughness, while for III-N WGs, the dry etching relies on physical bombardments thus exhibit less defect density dependence.

There are several limitations of this model. Firstly, only one pair of WG boundaries are involved in the scattering loss calculation. When height of WG approaches $\lambda/_{2n}$, the

scattered power towards upper/lower boundaries increase. Consequently, the TD induced loss will be slightly higher than what we computed using this model. Additionally, other types of defects are not involved in this model, which leads to an underestimated optical loss. To improve this model, several advanced computing techniques can be employed. To compute the far-field distribution accurately, finite element method can be implemented, which requires intense computing. Moreover, a recently proposed model [124] allows the decomposition of guided mode and radiative mode, providing the opportunity to obtain the far-field with only near fields computed.

CHAPTER 5

NONLINEAR OPTICAL APPLICATIONS BASED ON III-N PIC PLATFORM

Chip integrated nonlinear optics has enable a wide variety of applications [23,24]. Thanks to the noncentrosymmetric crystalline structure and ultra-wide bandgap of AlN, it possesses moderate nonzero $^{(2)}$ and $^{(3)}$ and allows broadband transparency from UV to IR. In this Chapter, we investigate the possibility of using AlN for coherent generation within UV and visible spectrum, which paves the way towards chip integrated III-N based comb source. The most challenging part in this research is to overcome the huge material dispersion as depicted in Fig. 6-1. Unlike the refractive indexes in IR, the indexes of AlN (same for other semiconductor and dielectric materials) changes dramatically in the visible spectrum due to the large photon energy [Fig. 5-1(a)]. It is this strong material dispersion that hindered the development of frequency comb within visible spectrum, because the generation of Kerr combs usually relies on the creation of anomalous GVD, which cannot be obtained in fundamental TE and TM modes within visible as shown in Fig. 6-1(b).

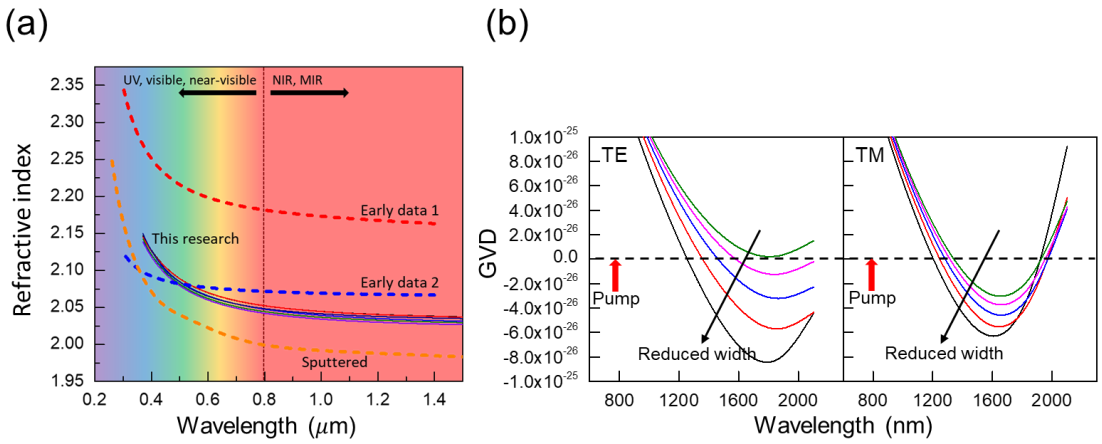

Figure 5-1. (a) Refractive index of AlN characterized within this research and adapted from other references [125-127]. (b) Calculated group velocity dispersion for TE and TM mode, changing the geometries fail to provide anomalous dispersion in near-visible spectrum.

Since the GVD in near-visible spectrum is mostly normal, when pumping the waveguide with fundamental TE/TM modes, self-phase modulation are expected as shown in Fig. 5-2. To overcome this strong material dispersion, novel techniques must be implemented.

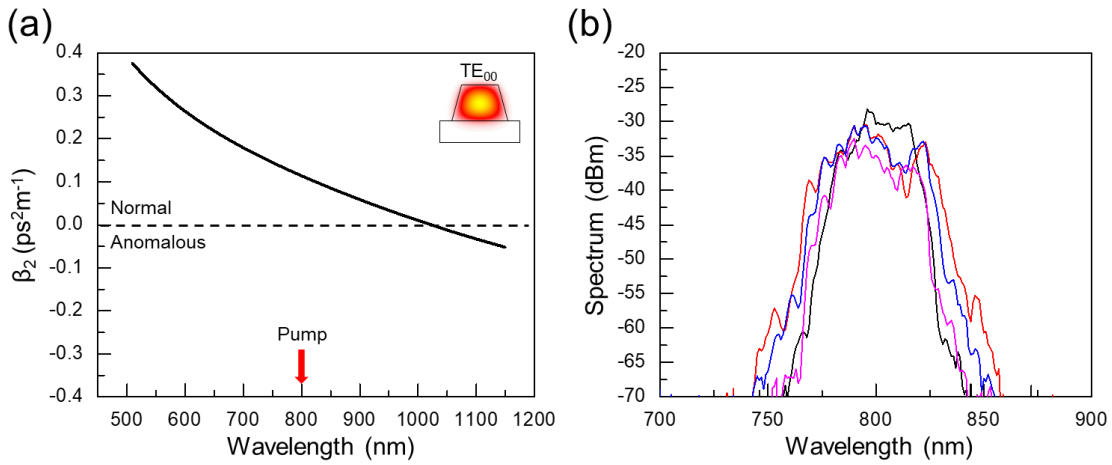

Figure 5-2. (a) Calculated GVD of AlN waveguide. (b) Experimentally measured spectrum when pumping the waveguide in fundamental TE and TM modes. The broadening of spectrum is mainly due to the self-phase modulation.

This Chapter explore the possibilities of achieving coherent generation within UV-visible spectrum utilizing SHG and soliton dynamics. The structure of this Chapter is as followed: firstly we present initial experimental findings when pumping AlN with high pulse energy. Then, we reveal the underlying physics by solving nonlinear Shrodinger's equations (NSE). By properly engineer the waveguide geometry, supercontinuum generation can be obtained continuously from visible to IR spectrum. Further optimizations using periodically pattern waveguide suggests that the spectrum would be further expanded via quasi-phase matching between solitons and dispersive waves.

5.1 Initial experimental results

When pumping the AlN waveguides with femto-second Ti:Sapphire lasers, the obtained spectrums are shown in Fig. 5-3. Several noteworthy features can be obtained from these preliminary results. Strong second harmonic generation from 390 nm to 440 nm can be identified. Due to the phase match requirements on SHG, the UV and near-UV signals only appears at certain wavelengths (phase-matched wavelengths). In addition to the SHG, when the waveguide was pumped at 780 nm, red emission near 600 nm can be observed. This wavelength failed to be neither phase matched to any frequency components or emitted from any defect states. One of the reason for this red emission is due to the soliton fission, in which the solitons are launched in the guided modes and phase matched to the dispersive waves [128]. The soliton fission process requires the presence of anomalous dispersion which is unable to achieve by the fundamental TE and TM modes of AlN waveguides. As a result, other high order modes should be responsible to this fission process. However, it's quite controversial that the high order modes are usually accompanied with strong propagation loss and fail to support the existence of solitons over long travel distance. Further investigations were carried out to explore the possibility of engineering the solitons within high order modes. As we will show in the following sections, for some special circumstance, the soliton within high order guided modes would provide large nonlinear frequency conversion efficiency and can be engineered for the coherent generation within visible or even UV spectrum. Some examples of CCD camera captured images during testing are shown in Fig. 5-4 for better illustration purposes.

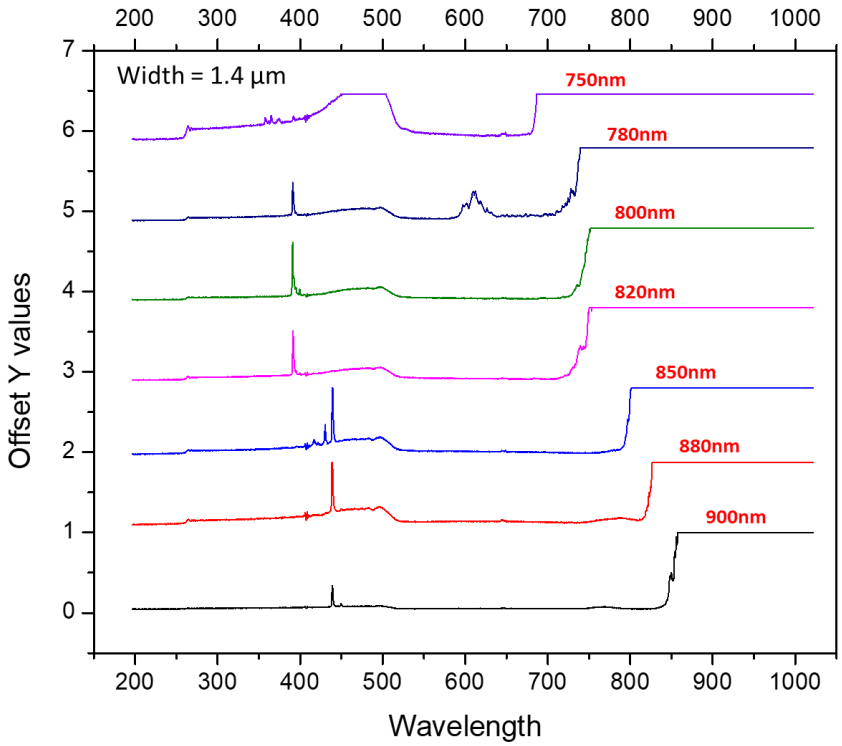

Figure 5-3. Obtained spectrum in the initial stage of this research, the waveguide was TM pumped. The x-axis is in the unit of nm.

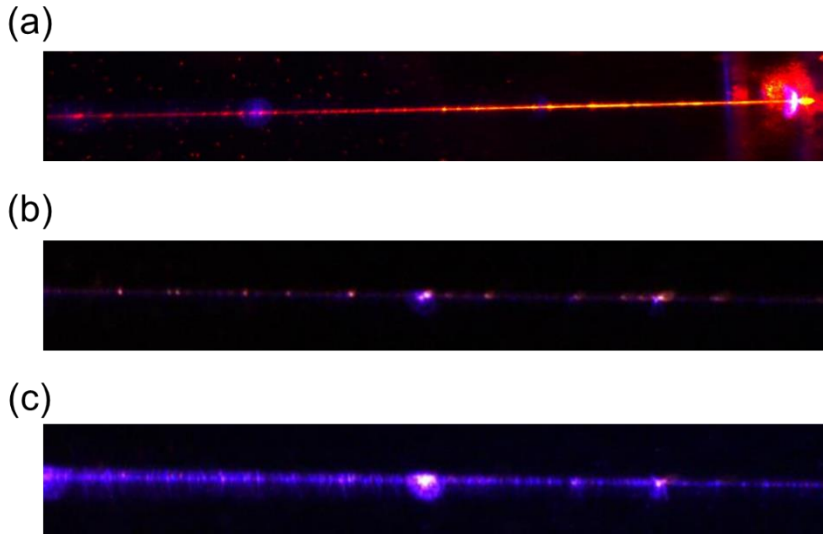

Figure 5-4. Images captured by CCD camera during testing, different physical processes can be identified. The input is from left side. (a) Soliton fission, (b) SHG when waveguide was TE pumped, (c) SHG when waveguide was TM pumped.

5.2 Methods for design

To understand the underlying physics behind the red mission recorded in Fig. 5-1 and Fig. 5-2, NSE was implemented to simulate pulse propagation. The code was in-house developed using split-step Fourier method [128], where the fourth order Runge-Kutta method [129] was also implemented to reduce computational load. The format of the nonlinear Schrodinger's equation was:

$$\frac{\partial A}{\partial z} = -\frac{\alpha}{2}A + i\sum_{k\geq 2} i^k \frac{\beta_k}{k!}\frac{\partial^k A}{\partial t^k} + i\gamma[|A|^2 \mathrm{A} + \frac{i}{\omega_0}\frac{\partial}{\partial t}(|A|^2 A) - T_{\mathrm{R}} A\frac{\partial |A|^2}{\partial t}] \quad (5\text{-}1)$$

where $A(z,t)$ denotes the pulse slow varying amplitude, α is the propagation loss, β_k is the kth order dispersion, γ is the nonlinear parameter, and T_{R} is the Raman response parameter. It should be noted that we keep the most simplified Raman response form in Eq. (5-1), and the T_{R} was set to zero as no significant red-shifted spectrum was observed through this whole study. Dispersion terms were truncated at 6$^{\mathrm{th}}$ order, but it is noteworthy that only third order dispersion plays significant role in modifying the spectrum. To estimate the Kerr refractive index of AlN, the experimental recorded data on n_2 at 1550 nm [69] was utilized, by applying the wavelength dependent fitting model [48], n_2 at 800 nm can be estimated to be 2.5 × 10^{-19} m^2/W, which gives a nonlinear parameter $\gamma \sim 3$ $W^{-1}m^{-1}$ depending on the mode effective area. The initial pulse shape was assumed to be Gaussian type with a full-width-at-half-maximum (FWHM) of 100 fs.

The AlN waveguides were fabricated using the processes described in Chapter 3. The process flow are briefly provided here for completeness. The AlN thin films were coated with a ~ 600 nm SiO_2 layer using plasma enhanced chemical vapor deposition

(PECVD), followed by an 80 nm Cr layer using electron-beam evaporation. The two layers served as hardmasks for the dry etching processes. Photoresist ma-N 2403 was used to perform electron-beam lithography (EBL). The Cr layer was etched away using a user developed (chlorine + argon) reactive ion etching (RIE) process, while the SiO_2 layer was removed by standard anisotropic RIE etching process developed by ASU NanoFab. The AlN waveguide patterns were defined using a user developed inductively coupled plasma (ICP) etching with Cl_2, $BrCl_3$, and Ar chemistries at a bias voltage near 300 V. The waveguides were coated by 2 μm SiO_2 coating layers to reduce scattering loss. After fabrication, samples were cut and polished down to 0.1 μm grade. The fabricated waveguide has ~ 50 to 100 nm width variance due to the isotropic nature of the Cr etching process. This variance was included in numerical simulations. Detailed process flow and scanning electron microscope (SEM) images of the fabricated AlN waveguides can be found in the Chapter 2.

To sufficiently excite high order guided modes, several excitation strategies were implemented. which are illustrated in Figs. 5-5(a)–5-5(d). Figure 5-5(a) shows the evanescent wave coupling method, which is the most widely used mode conversion approach. However, such method usually requires single mode bus waveguide, which has strong propagation losses in the near-visible spectrum. Furthermore, the coupling region designs in this approach varies with changing waveguide geometries, which requires intensive design efforts.

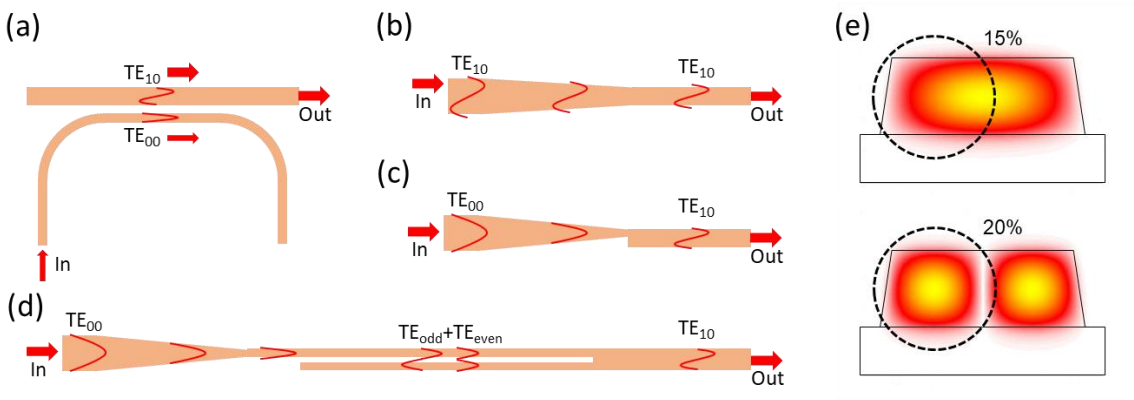

Figure 5-5. Schematic of high order mode excitation strategies. (a)–(d) Several high order mode excitation methods that were considered and utilized in this research (E) Mode profile ($|E_x|$) of the TE_{00} and the TE_{10} at the normal taper facet. The free-space beam profile at the focal point of the optical objective is marked out using black dash circles.

In this work, we used an alternative approach to excite the higher order modes by implementing the normal tapers with carefully designed waveguide structures. This approach is illustrated in Fig. 5-5(b).

Another excitation method that can be used to effectively launch the high order modes inside waveguides is illustrated in Fig. 5-5(d). A trench was intentionally dry etched at the center of waveguide to form "array waveguide". Due to the strong disturbance at the waveguide center, the fundamental TE_{00} mode will no longer exist. Nevertheless, the trench is only a small perturbation onto the TE_{10} mode, whose propagation behavior (e.g., dispersion) is inherited by the TE_{odd} mode. This method was employed in this research as auxiliary experiment to support the conclusion drawn in the manuscript.

Figure 5-5(e) provides excitation efficiency of the TE_{00} and the TE_{10} modes. The excitation location at taper facet is marked out by black dash circle. It should also be noted that the coupling efficiency of TE_{20} mode is 13% at the optimal coupling position for TE_{10}

mode, due to the strong scattering loss, the impact from this mode is neglected. The coupling efficiency of other high order modes are less than 10%.

During the experiment, under low power operation, the beam was first focused at the center of taper, then the position was optimized by slowly varying the nano-stage to move the focal point from the center to the edge of the taper facet. The out-scattered light was monitored by a CMOS camera at the same time. Since the TE_{10} mode has higher scattering loss comparing to the TE_{00} mode, when the out-scattered light reaches its maximum (as recorded by CMOS camera), the excitation efficiency of TE_{10} mode will be near its maximum. At this stage, the location of focusing point is near the edge of taper facet, which can be confirmed by the CMOS camera. An alternative way to excite the TE_{10} mode was to operate the system under higher power (near 30 mW on-chip average pumping power). By slowly varying the focal point from center to the edge of the taper, DWs near 600 nm were generated due to the increasing excitation efficiency of the TE_{10} mode. The red radiation can be directly observed under a microscope, and the excitation efficiency of the TE_{10} mode can be optimized by maximizing the red radiation.

It should also be noted that the high order mode usually exhibits strong propagation loss when comparing with the fundamental modes. To estimate the propagation loss the high order modes, the propagation losses of the TE_{00} modes were experimentally characterized by collecting out-scattered light along the propagation direction using a CMOS camera. The typical scattered optical power versus propagation length is provided in Fig. 5-6. By adopting semi-log plotting, the decay slope is proportional to propagation loss of the TE_{00} mode in dB/cm. The low loss of the TE_{00} mode was further confirmed by measuring the intrinsic quality factor of ring resonators as shown in Chapter 4.

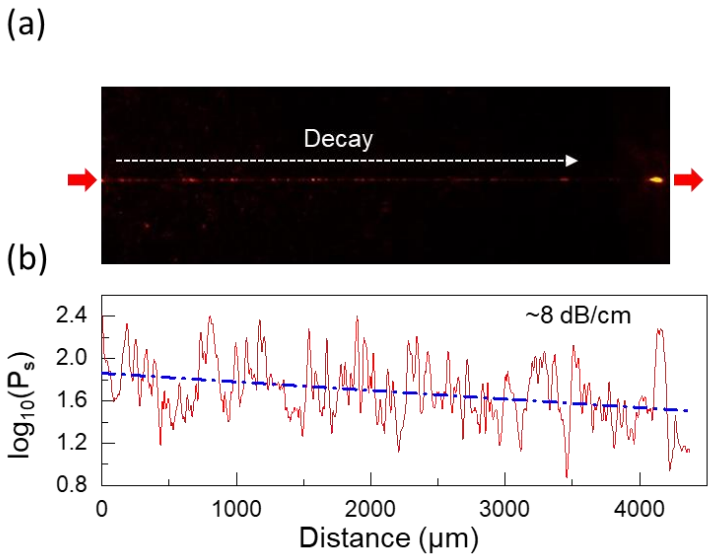

Figure 5-6. Measurement of propagation loss. (a) The representative microscope image of the out scattered light from the waveguide (H = 1.1 μm, W = 1 μm). (b) By plotting the red light intensity at each pixel along the propagation direction (in the semi-log scale), the slope can be used to estimate propagation loss.

The losses of TE_{00} modes with different waveguide widths were fitted by an in-house made dyadic Green's function (DGF) solver to obtain the sidewall roughness. The detailed description on DGF can be found in Chapter 4. DGF fitting gives sidewall roughness around 4 nm, which agrees well with standard optimized ICP etching process. By plugging in TE_{10} mode profile and sidewall roughness, the scattering loss can be estimated.

5.3 On-chip octave-spanning supercontinuum generation

On-chip supercontinuum generation spanning from ultraviolet (UV) through infrared (IR) with low (sub-nJ) powers has been a quest of researchers since the original demonstration of the laser in the 1960's [130,131]. An integrated system would enable research efforts and technology in coherent white light emitters [132,133], frequency metrology [134,135], and imaging [137,138]. While attempts have been made using a wide

range of material systems and nonlinear phenomena [30-37], this goal has so far eluded the research community due to fundamental principles. Namely, the majority of attempts relied on a combination of self-phase modulation (SPM) and soliton fission processes where the solitons were launched deeply inside the anomalous dispersive region [34,35] in fundamental transverse electric (TE) or transverse magnetic (TM) modes. Moreover, solitons that launch deeply within the anomalous dispersive region typically require relatively high pulse energy to maintain the same soliton number [128], which in turn degrades the energy efficiency. As a result, despite success in achieving broadband spectrum, this strategy failed to reach below 500 nm due to limits in material crystallinity and reliance on long wavelength pump sources. One exception is the work based on silica ridge waveguides which successfully stretched into the UV range [36]. However, the low nonlinear parameter of silica required pump energies in excess of ~1 nJ to be used. Therefore, to overcome this limit, a material with a higher nonlinear parameter must be used. One of such material is aluminum nitride (AlN).

In a preliminary study, the high $\chi^{(2)}$ of AlN was used to achieve directional nonlinear energy transfer [37]. This approach enabled supercontinuum generation with a pulse energy of only 0.237 nJ. The spectrum ranged from approximately 650–900 nm with a second spectrum from approximately 350–450 nm. This wavelength range, and discontinuity, is because this system was limited to operation in the normal group velocity dispersion (GVD) regime. Therefore, it is a fundamental limit of the device design and operation.

To achieve coherent broadband supercontinuum generation covering the entire visible spectrum using AlN, several nonlinear optical processes can be employed as the

potential broadening mechanisms for the device design with both advantages and limitations. For example, SPM is the most commonly observed process in the initial stage of spectrum broadening, however it requires extreme high excitation power to further expand the spectrum [128]. Four-wave mixing has also demonstrated broadband frequency generation [32,33]. However, it generally relies on high performance resonating device structures to achieve the high optical intensities required. Additionally, this approach has limited bandwidth due to the requirement of phase-matching. Self-steepening has the potential for broadband directional supercontinuum generation in UV–visible range; however, it requires small and flat dispersion near pumping wavelengths to efficiently build the steep temporal structures [44]. This process is hindered by the strong material dispersion in the near-visible spectrum. Other nonlinear processes such as Raman scattering [128] and modulation instability [128] are usually accompanied by strong phase noise and thus are not favorable.

To solve these barriers, the present work combines several innovations in materials science and optics to develop a broadband transparent AlN platform [Figs. 5-7(a)–(c)] with dispersion engineered waveguides to achieve supercontinuum generation from violet to near IR wavelengths with sub-nJ pulse energy. To overcome the strong material dispersion, a high order waveguide mode (TE_{10}) was excited. A convenient and high efficiency excitation strategy was used to achieve high free-space to on-chip coupling efficiency. Additionally, the solitons were launched near the zero-dispersion wavelengths (ZDW), reducing the required pulse energy. Moreover, the metalorganic chemical vapor deposition (MOCVD) grown single crystalline AlN exhibited low threading dislocation density (less

than 10^9 cm^{-2}), and as a result, low propagation losses were achieved at the pumping wavelengths.

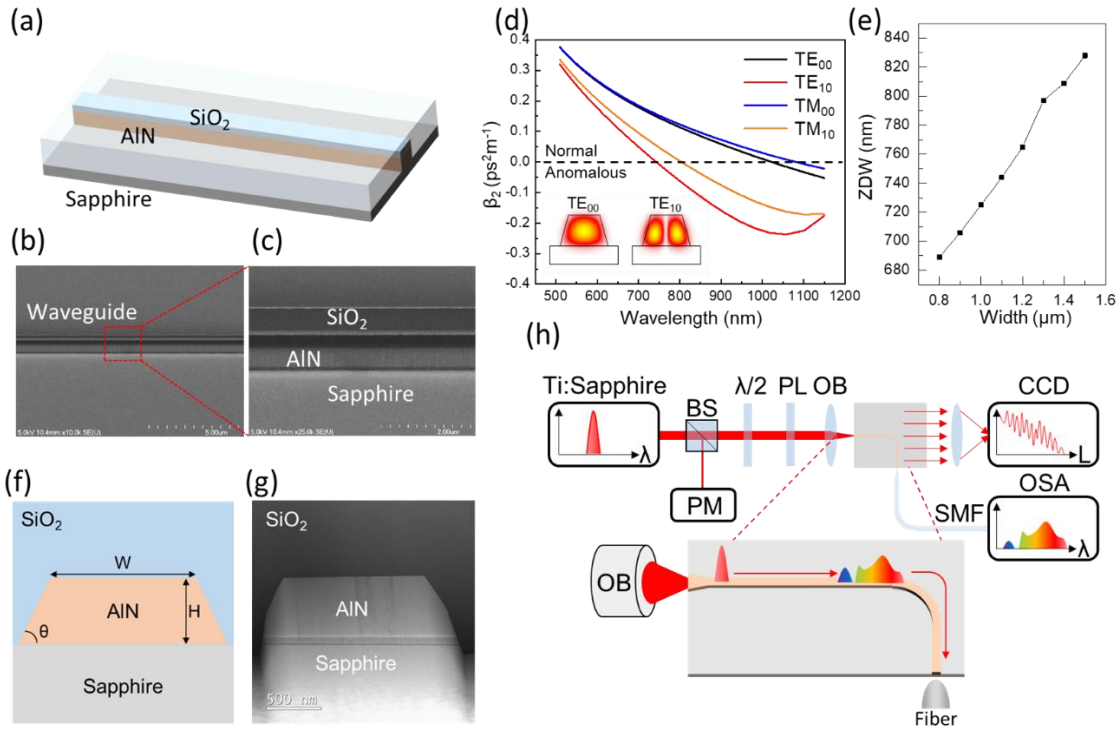

Figure 5-7. Device schematic, working principle, and design of experiment. (a) Three dimensional schematic of the waveguide fabricated in this research. The coating and cladding layer is semi-transparent for illustration purpose. (b) Tilted scanning electron microscope image of the AlN waveguides fabricated in this research, the orientation is similar to (a). Images were token before the deposition of coating layer. (c) Zoomed view of (b). The SiO_2 hardmask remains on top. Smooth sidewalls can be identified from the zoomed image. (d) Calculated GVDs of TE_{00}, TE_{10}, TM_{00}, and TM_{10} modes in a 1.1 μm × 1.2 μm (W × H) AlN waveguide. The inset shows the mode profiles ($|E_x|$) of TE_{00} and TE_{10} modes, which are the modes that are used in this work. (e) The zero-dispersion wavelength increases as the width increases. The height was kept at 1.2 μm. (f) Cross section schematic view of the AlN waveguide, where the waveguide geometries such as width (w), height (h), and sidewall angle (θ) are defined. (g) Transmission electron microscope image of a typical AlN waveguide fabricated in this work. (h) Experimental setup implemented in this work. BS, λ/2, PL, PM, and OB indicate beam splitter, half-wavelength plate, polarizer, power meter, and optical objective lens, respectively.

To optimize the dispersion of the AlN waveguide, the modal dispersion for a series of waveguide geometries was computed from an in-house custom numerical solver based on finite-difference method (FDM) provided in [138]. The computed dispersions were compared with commercial software (Lumerical) to confirm accuracy. These calculations were used to guide the device design and mode selection. For example, the calculated GVD in a 1.1 μm × 1.2 μm (W×H) waveguide is shown in Fig. 5-7(d). Due to the highly dispersive material property, TE_{00} and TM_{00} modes exhibit normal dispersion below 1000 nm while TE_{10} mode shows anomalous dispersion above 740 nm. Anomalous dispersion supports the formation of solitons near the operating wavelengths of Ti:sapphire laser. The ZDW of this TE_{10} mode is widely tunable by varying waveguide widths, as illustrated in Fig. 5-7(e). To simulate the complete spectrum for each mode, the nonlinear Schrodinger's equation (NSE) is solved. Details of the NSE simulation has been given in previous section.

While the theoretical metrics detailed in Figs. 5-7(d) and 5-7(e) provide a general framework, previous experimental device efforts have shown that even nanometer scale roughness can significantly diminish an optical device performance [139]. This decrease impacts the ability of a device to generate sufficient power to support nonlinear phenomenon. As such, the material deposition and fabrication procedures play a critical role in the device performance. To overcome this barrier, single crystalline AlN thin films were epitaxially grown by MOCVD on sapphire substrates. The growth was optimized to create films with a threading dislocation density less than 10^9 cm^{-2} identified by X-ray powder diffraction (XRD), resulting in broadband optical transparency. The surface roughness, as determined by atomic force microscopy (AFM) in a 5 μm × 5 μm scan, had a root mean squared (RMS) roughness of ~ 3 nm. Refractive indexes of the thin films, as

measured by ellipsometry at 800 nm, were 2.05. Original data on the material characterizations (XRD, AFM, ellipsometry) are provided in Chapter 4.

Figure 5-7(f) shows the schematic cross-section of the device structure of the AlN waveguide, where the waveguide geometrical parameters, such as width (W), height (H), and sidewall angle (θ), are defined. SiO_2-clad waveguides were fabricated from 1.2 μm thick films (H) of AlN with widths ranging from 0.8 μm to 1.6 μm and lengths around 0.6 cm. After a propagation length of 0.6 cm, the waveguide was rotated by 90˚ and the light was collected by a lensed fiber. With this design, a large portion of stray light was avoided. Figure 1(g) shows a transmission electron micrograph (TEM) image of a representative cross-section of the AlN waveguide. The crystalline nature of the AlN thin film is clearly evident. Additional material data and waveguide fabrication details are in the Methods section.

The experimental setup is depicted in Fig. 5-7(h). A linearly polarized standard Ti:sapphire laser (Spectra Physics) with 100 fs pulse width (full-width half-maximum) and 82 MHz repetition rate was used. A beam sampler (1:99) and a thermal optical power sensor were utilized to monitor the optical power before chip. The average power in free space was tuned below 150 mW to avoid any damage to the sample. To couple light into the on-chip waveguides from the free-space laser, end-fire coupling was utilized. The out scattered light from the waveguides was collected by a linear CMOS camera (Thorlabs DCC1240) and used to perform propagation loss estimation. A tapered fiber was placed near the output port of waveguides, and the output signal was fed into optical spectrum analyzer (Yokogawa AQ6373B). Coupling strategies to efficiently excite the high order modes are discussed in the Methods section.

A broadband supercontinuum spectrum is shown in Fig. 5-8(a). The main spectrum spans from 490 nm to 1100 nm, which is over one octave. Due to the large second order susceptibility of AlN, a secondary spectrum was observed from 405 nm to 425 nm. The pumping wavelength was slightly tuned near 800 nm, and the best spectrum [Figure 6-8(a)] was recorded at λ = 810 nm. Minor changes were observed when varying the pumping wavelength from 800 nm to 820 nm.

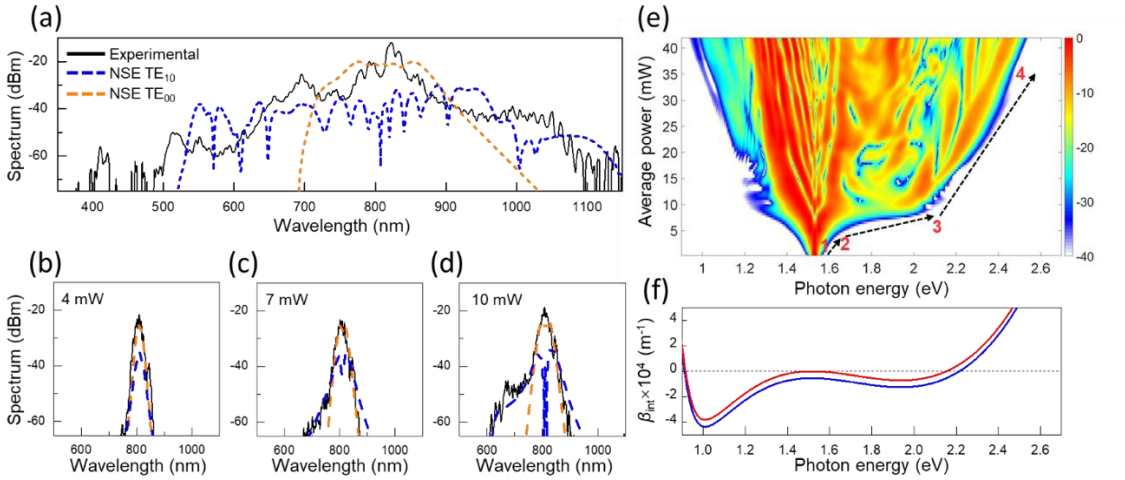

Figure 5-8. Experimental and modeling results of supercontinuum generation. (a) Experimental results of the supercontinuum spectrum (black solid) and the NSE simulated spectrum of TE_{00} (orange dash) and TE_{10} (Blue dash) modes for the AlN waveguide. The spectrum is generated with a pump wavelength of 810 nm at average pump power of 30 mW. (b)-(d) The experimental (black solid) and the NSE simulated results (orange and blue dash) under low power pumping conditions. (e) Spectral evolutions of the AlN waveguide at different average pumping powers from 0.2 mW to 42 mW (within TE_{10} mode) used in the measurements. From point 1–2, 2–3, and 3–4, the broadening mechanism was governed by SPM, DW generation, and optical power dependent phase-matching between soliton and DW. At each average power, the spectrum is normalized to the maximum spectral intensity. (f) The integrated dispersion vs. photon energy at the average pumping power of 30 mW. The red and blue curves indicate the integrated dispersions with (red) and without (blue) the power dependent term.

The broadened spectrum in Fig. 5-8(a) can be identified as the composition of TE_{00} and TE_{10} modes. Due to the ultra-short pulse width and different group velocities, the TE_{00} and TE_{10} modes split in the temporal domain after a propagation length of a few microns. Therefore, throughout this study, the mutual nonlinear coupling between TE_{00} and TE_{10} modes were neglected. According to the numerical simulation using coupled mode theory, the free-space to on-chip coupling efficiencies of TE_{00} and TE_{10} modes are 15% and 20%, respectively. Therefore, the on-chip average power used in Fig. 5-8(a) can be estimated to be ~ 50 mW (TE_{00} + TE_{10}); thus, the average power within TE_{10} mode was estimated to be 30 mW, corresponding to a pulse energy of 0.36 nJ. This pulse energy is among the lowest values when compared with other supercontinuum generation methods at short wavelengths [36,37].

The experimentally measured spectrum can be compared to the pair of spectrum calculated using the NSE [Fig. 5-8(a)]. As predicted in Fig. 5-7(c), the TE_{00} mode was propagating within the normal dispersion region. Therefore, SPM is the major contributor to its broadening mechanism. In contrast, for the TE_{10} mode, the pulse was split into its constituent fundamental solitons, and the solitons were phase matched to DWs in the short wavelengths. As a result, DWs emitted near 500 nm through non-solitonic radiation were achieved, enabling the formation of the broadband supercontinuum only in the TE_{10} mode case.

Under high power excitation, complex physical processes are expected such as thermal effects [140], multi-photon absorption [141], free carrier absorption/dispersion [141], wavelength dependent linear loss [142] and nonlinear parameters [143], and mode avoid-crossing [144]. Under such conditions, although the NSE provides a good estimation

of the spectrum width, it is unable to accurately predict the spectrum shape at all wavelengths. Therefore, to further confirm the non-solitonic radiation process, a series of low excitation power measurements were performed, and the corresponding spectra were recorded [Figures 6-8(b)–6-8(d)]. It should be noted that when the on-chip average power exceeds ~ 100 mW, behaviors indicative of thermal melting or dielectric breakdown began to be observed. Notably, irreversible material damage was occurred, inducing material defects that can be readily identified under the microscope via white light luminescence from defect states [95]. To avoid this irreversible damage, the on-chip power was kept at least two times lower than this value.

When the average pumping power is below 10 mW, the SPM process is responsible for the symmetric broadening as indicated in Figs. 5-8(b) and 5-8(c). When the average pumping power reaches 10 mW which corresponds to a pulse energy of only 0.12 nJ, significant asymmetric broadening starts to initiate as shown in Fig. 6-8(d). The development of supercontinuum spectrum with increasing power from 0.2 mW to 42 mW can be further illustrated using Fig. 5-8(e). The spectral broadening was first initiated symmetrically by SPM (point 1 to 2), and then asymmetrically expanded by DW emission (point 2 to 3). From point 3 to 4, blue shifts of DW can be observed, which is due to the power dependent phase matching condition for DWs [128]:

$$\beta(\omega) = \beta(\omega_s) + \beta_1(\omega - \omega_s) + \frac{1}{2}\gamma P_s \tag{5-2}$$

where β indicates the wavevector. ω_s and ω indicate angular frequency of soliton and DW, respectively. β_1 is equal to $\partial\beta/\partial\omega$. P_s is the power within soliton modes. γ is the nonlinear

parameter that described by $(\omega n_2)/(cA_{\text{eff}})$, where the c and A_{eff} indicate vacuum speed of light and effective modal area, respectively. The blue shifts of DW with increasing power can be attributed to the power dependent term in the Eq. (5-2).

Given the dependence shown in Fig. 5-8(e), it is apparent that, unlike the prior results on supercontinuum generation that rely on fourth order dispersion, the spectrum obtained in this work exhibits strong dependence on the waveguide geometry due to the near ZDW pump wavelength. The phase-matching between DW and soliton can be revealed in Fig. 5-8(f), in which the integrated dispersion [Eq. (5-3)] is employed to identify the spectral component:

$$\beta_{int}(\omega) = \beta(\omega) - \beta(\omega_s) - \beta_1(\omega - \omega_s) - \frac{1}{2}\gamma P_s \tag{5-3}$$

To further investigate this dependence and create a generalizable waveguide design strategy, the GVD (β_2), third order dispersion (β_3), and fourth order dispersion (β_4), curves for AlN waveguides with different widths are calculated [Fig. 5-9(a)]. Based on this graph, it is evident that a waveguide width below 1200 nm is required to support the solitons near the pumping wavelengths used in this work. It is also noteworthy that below a waveguide width of 800 nm, the solitons were launched deep inside anomalous dispersion, which results in higher required pulse energy. Moreover, as is estimated in Fig. 5-9(b), the propagation loss of the TE_{10} mode increases exponentially with reducing waveguide widths, which exceeds 50 dB/cm at a waveguide width of 1000 nm. This strong loss prohibits the formation of fundamental solitons [141], which in turn prevents the DW emission. To

further reveal the geometry dependence, the integrated dispersions at different geometries are given in Fig. 5-9(c).

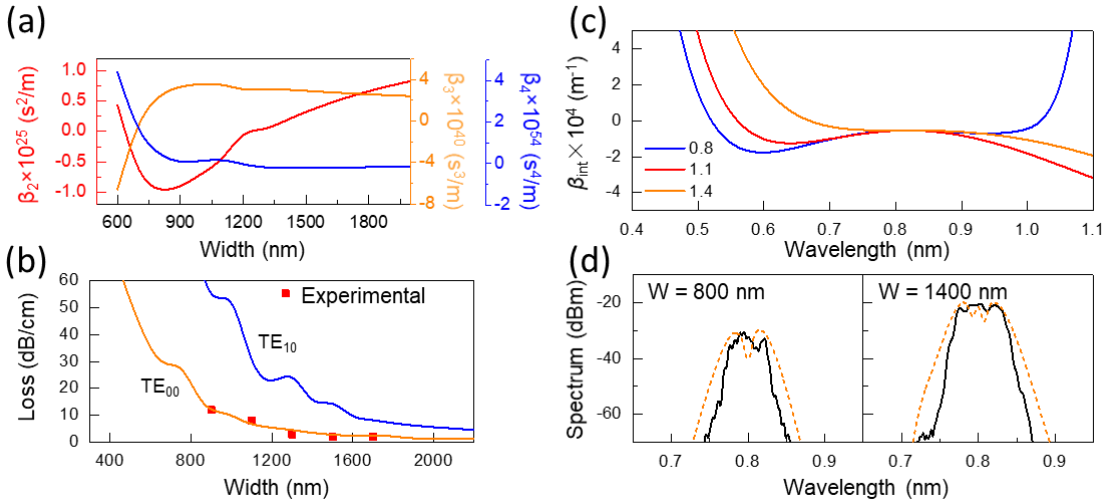

Figure 5-9. Experimental and modeling results of devices with different geometries. (a) The calculated GVD (β_2), third order dispersion (β_3), and fourth order dispersion (β_4) curves for AlN waveguides with different widths, represented by red, orange, and blue curves, respectively. (b) Experimentally measured propagation loss (square points) in dB/cm at the wavelength of 800 nm, and the calculated propagation loss for TE_{00} (orange curve) and TE_{10} (blue curve) modes for AlN waveguides with different widths. (c) The calculated integrated dispersion vs. wavelength for waveguide width at 0.8, 1.1, and 1.4 μm. (d) Measured spectrum (black curve) and NSE simulated pulse spectrum (orange dash curve) for TE_{00} mode in AlN waveguides with widths of 800 nm and 1400 nm. The spectrum was mainly broadened by SPM of the fundamental TE_{00} mode; therefore, the simulated spectra for the TE_{10} mode are not shown here.

Combining the observations in Figs. 5-9(a) and 5-9(b), the width of the AlN waveguide devices for this work is limited between ~ 1000 nm to ~ 1200 nm. To verify these calculations, devices outside of this optimum range were fabricated and characterized. Figure 5-9(c) illustrates the measured spectrum and the NSE simulated pulse spectrum for the TE_{00} mode in AlN waveguides with widths of 800 nm and 1400 nm. The broadening processes in these two waveguide designs can be clearly identified as SPM, and the average

pumping power within the TE_{10} was estimated to be ~ 20 mW, which is two times higher than that in the case of Fig. 5-9(d).

While the generation of the primary spectrum from 490 nm to 1100 nm in the visible spectrum with only 0.36 nJ is remarkable, the simultaneous generation of an even higher energy (lower wavelength) secondary spectrum spanning from 405 to 425 nm further increases the potential impact of this system. To understand the physical mechanism that gives rise to this secondary spectrum, we solve for the mode dispersion near the fundamental and the SHG wavelengths, and the mode profiles of high order modes near SHG wavelengths are depicted in Fig. 5-10(a). Figure 5-10(b) shows the modal dispersion of TE_{00} mode and TE_{10} mode near 800 nm, and the dispersion of several high order modes near 400 nm. By optimizing the waveguide coupling design, modal phase-matching was achieved at 398 nm and 412 nm. Furthermore, Fig. 5-10(b) also shows the dispersion curve of TE_{10} mode in the near-visible region. Since the phase-matching point is far away from 400 nm, and the two phase-matching points have a wavelength difference of over 40 nm, we neglect the SHG effect from the TE_{10} mode.

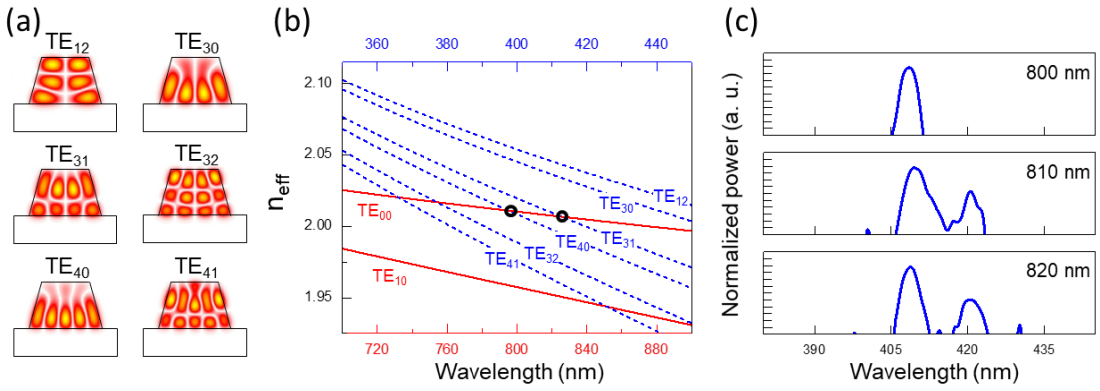

Figure 5-10. Experimental and modeling results showing role of SHG. (a) Mode profile ($|E_x|$) of each high order mode computed at 400 nm

wavelength. (b) The modal dispersion of TE_{00} mode and TE_{10} mode near 800 nm (red curves) and the dispersion of several high order modes near 400 nm (blue dash curves) for the secondary spectrum from 405 to 425 nm in Fig. 2(A). Phase matching wavelengths can be determined at the crossing points of the curves. The two experimentally measured peaks can be identified at the two indicated points. (c) SHG signal near 400 nm at different pumping wavelengths. The locations of the SHG peaks were invariant to pumping wavelengths.

The experimentally-identified second harmonic signals were recorded at 407 nm and 421 nm and are shown in Fig. 5-10(c). The MOCVD growth and the dry etching processes for the AlN waveguides may cause minor geometry discrepancy between the simulation and the experiment, which resulted in the small differences between the simulated and experimentally-recorded phase matching points. Since the phase-matching wavelengths are dependent on the device geometry, the location of SHG signal is invariant to pumping wavelengths, which is evident in Fig. 5-10(c).

The optical coherence of the spectrum can be determined by applying the first-order coherence function [35,36,145]:

$$\left|g_{12}^{(1)}(\lambda)\right| = \left|\frac{\langle E_1^*(\lambda)E_2(\lambda)\rangle}{\sqrt{\langle|E_1(\lambda)|^2\rangle\langle|E_2(\lambda)|^2\rangle}}\right| \tag{6-4}$$

which is the ensemble average of multiple supercontinuum pulses. The simulation took 100 supercontinuum pulses with a standard shot noise at the input spectra, and the noise spectrum is constituted by one photon per spectral bin [146]. The simulated first-order coherence function of TE_{10} supercontinuum is shown in Fig. 5-11(a). In addition to shot noise, to emulate the intensity fluctuation of pump source [147,148], relative intensity noise (RIN) is also involved in respect of intra-pulse (RIN within MHz frequency range) and inter-pulse (RIN within THz frequency range) power fluctuations. For intra-pulse RIN, the

noise is influential to the energy of individual pulse but does not alter the Gaussian temporal profile. While for the case of inter-pulse RIN, the noise is applied to the pulse itself thus the temporal profile is no longer ideal. The obtained coherence functions with the presence of shot noise and RIN are depicted in Figs. 5-11(b) and 5-11(c). The coherence is close to unity from visible to near-infrared when intra-pulse RIN was applied. The close to unity coherence can be attributed to the relative low pulse energy (peak power ~3.7 KW). It's also noteworthy that the inter-pulse RIN is influential to the coherence performance, when the power fluctuation exceeds 0.5%, significant deterioration on the coherence can be observed as shown in Fig. 5-11(c). It should also be noted that in-depth investigation on the noise performance should be done by involving polarization modulation instability [148] as the crystalline structure of AlN is highly anisotropic, in which considerable birefringence is expected [149].

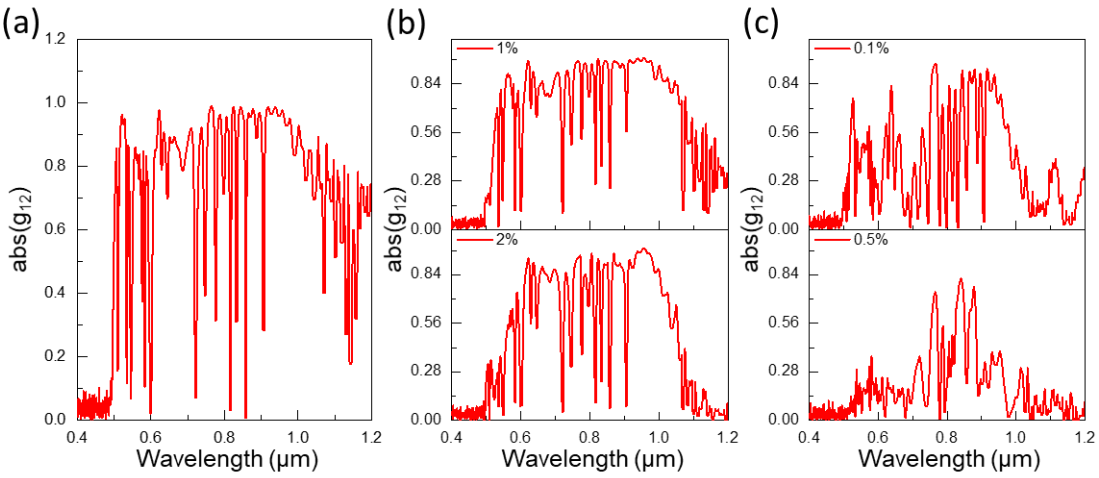

Figure 5-11. The simulated first-order coherence function vs. wavelengths for AlN waveguide with a width of 1.2 μm at different noise conditions. (a) The coherence function with quantum limited shot noise involved. (b) In addition to the shot noise, 1% (top) and 2% (bottom) intra-pulse RIN are involved. (c) The coherence function with the presence of 0.1% (top) and 0.5% (bottom) inter-pulse power fluctuation. The inter-pulse RIN is influential to the coherence performance.

In a short conclusion, we have demonstrated supercontinuum generation using a dispersion engineered AlN waveguide with ultra-low input power. Notably, the main spectrum covers from 490 nm to over 1100 nm with a secondary SHG spectrum from 405 nm to 425 nm. Near-visible pumping was implemented to improve energy efficiency. To overcome the strong material dispersion, the AlN waveguides were designed to support high order modes. The experimental results were compared with the theoretical results from FDM and NSE simulations, which confirmed that DWs were generated from solitons perturbed by third order dispersion, allowing for directional energy transfer. Further investigations on high order dispersion terms and propagation losses reveal that the SF process can only be initiated within a narrow window of waveguide width, which was supported by the experimental findings. The SHG spectrum was investigated by solving modal dispersions near 800 nm and 400 nm, and the corresponding phase-matching wavelengths were determined. Simulations of the first-order coherence function suggest that the spectrum broadening procedure is robust to noise. The outcome of our work demonstrates that the high order modes are experimentally applicable to efficient spectrum broadening and can greatly overcome the large material dispersion within the visible spectrum.

Noting that III-N material system exhibits excellent monolithic integration capability with lasers/detectors (InGaN) and high-speed RF transistors (AlGaN), the demonstration from this work is an important first step towards an on-chip fully integrated broadband supercontinuum source in the visible, which is of high interest in a range of fields including on-chip mode locking, parametric oscillator, and entangled photon generation.

5.4 Supercontinuum generation from QPM techniques

To further expand the spectrum obtained from previous section, one of the technique that would be potentially implemented is the quasi-phase matching (QPM) techniques [150]. The QPM technique has been widely adopted for SHG [151] by periodically poled lithium niobate waveguide. Some recent investigations also suggest that the GaN and AlN can be poled for efficient harmonic generation [152,153]. For the QPM techniques in SHG, the second order susceptibility is periodically changing its sign, which in turn allows continuous growth of harmonically generated optical power. In the scenario of soliton fission, the QPM technology periodically modifies the GVD and high orders of dispersion terms. The basic working principle of quasi-phase matching is shown in Fig. 5-12. When the waveguide is periodically modulated, the nonlinear optical parameters are modulated as well as shown in Fig. 6-12(b). The phase matching condition between soliton and dispersive waves can be described by Eq. (5-5), where subscript λ_s indicates the wavelength of soliton, λ indicates the wavelength of dispersive wave. n is the effective index of the guided mode. Λ is the periodicity of modulation, q is an integer that represents the order number. Due to the periodically modulated dispersion, an extra term $\frac{2\pi q\lambda}{\Lambda}$ is exist.

$$n(\lambda_s) + (\lambda - \lambda_s)\frac{dn}{d\lambda} + \gamma P\lambda_s - \frac{2\pi q\lambda}{\Lambda} = n(\lambda) \tag{5-5}$$

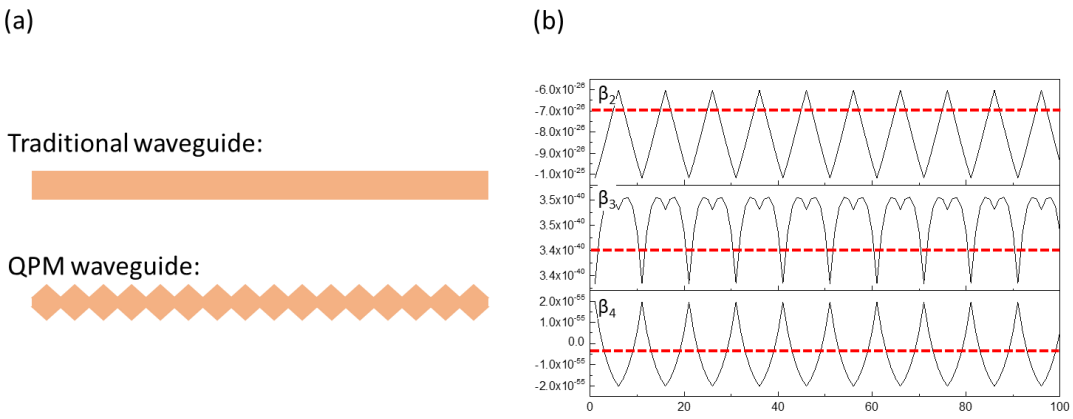

Figure 5-12. The concept of QPM techniques. (a) Waveguide geometries for traditional waveguide and QPM waveguide. (b) The modulated second order, third order, and fourth order dispersions versus propagation distance.

The extra term in Eq. (5-5) splits the dispersion curve into different orders as shown in Fig. 5-13. When q is equal to -1, -2, and -3, the phase matched points extends further into the blue side, this is beneficial for the supercontinuum generation that fully covering UV-visible spectrum. In this investigation, the waveguide geometries that used in previous section is employed (1.2 μm thickness and 1.1 μm waveguide width). The modeling relies on solving the NSE with periodically changing dispersion terms. The loss of waveguides is estimated to be 30 dB/cm. The QPM waveguide has periodicity defined by L and modulation depth defined by W. Therefore, the width of waveguide is ranging from $1.1 \pm W$ μm.

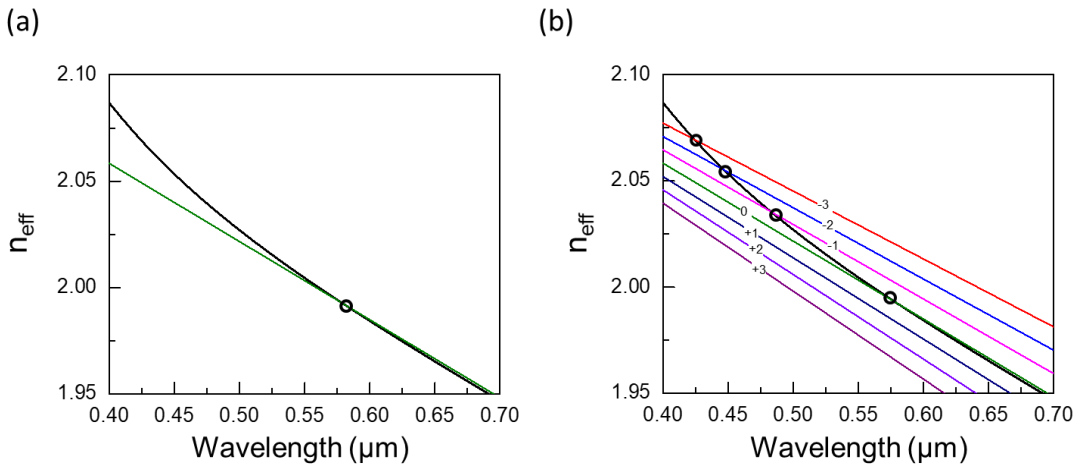

Figure 5-13. The dispersion of soliton and the dispersion of dispersive waves when utilizing QPM techniques. (a) Phase matching point for traditional waveguides, the soliton index is only phase matched to one point with the dispersive wave. (b) When waveguide geometry is modulated, the dispersion of soliton splits into different orders, which lead to the phase matching at different orders.

Finally, the NSE simulated spectrum is shown in Fig. 5-14. When no loss is applied [Figure 6-14(a)], 30 nm of broadening can be observed from 480 nm to 450 nm. While when the loss is applied, QPM generated frequency component is still observable.

It should also be noted that the periodically changing width causes the modal coupling between fundamental and high order modes, which cannot be predicted by NSE. Further experiments are needed to explore the QPM techniques, and the simulation performed here only serves as preliminary results.

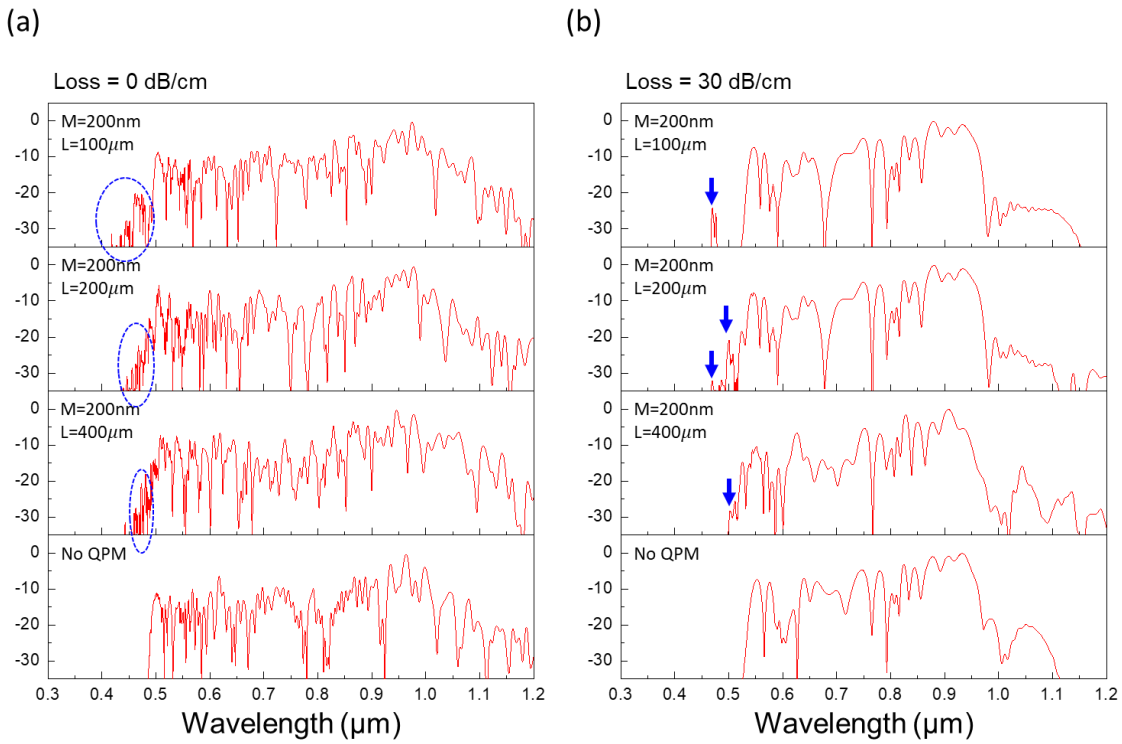

Figure 5-14. The NSE simulated spectrum at different period and modulation depth. (a) The obtained spectrum when loss is not applied. The QPM generated wavelengths are marked by blue dash circles. (b) 30 dB/cm of loss was applied, the QPM signal can still be identified as marked by blue arrows.

In a short conclusion, in this Chapter, we observed the red emission from AlN waveguides under femto-second pumping, the emission is attributed to dispersive wave generation. The dispersive wave is originated from solitons in high order guided mode. By properly engineering the waveguide geometries, the intensity of generated dispersive waves can be further enhanced. Experimental observations further convinced that solitons within high order modes, although accompanied with strong propagation loss, can be utilized for efficient nonlinear optical energy transfer under certain circumstance (near zero GVD pumping). This work paves the way towards fully integrated III-N based UV-visible comb source.

CHAPTER 6

CONCLUSION AND FUTURE WORKS

6.1 Conclusion

In this section, we conclude this work. In Chapter 2, the nonlinear optical properties (TPA coefficient, Kerr nonlinear refractive index) of GaN and β-Ga_2O_3 were identified experimentally, the GaN exhibits larger TPA loss, which can be attributed to its large density of threading dislocations. The experimental results on β-Ga_2O_3 suggest a weaker nonlinear optical response comparing with GaN, which can be attributed to the excellent crystal quality due to the melting growth method. Due to the highly asymmetric crystalline structure of β-Ga_2O_3, the nonlinear optical response exhibits strong polarization dependence. It's noteworthy that the β-Ga_2O_3 possesses low index contrast with sapphire and silica, which can be potentially adopted for ultra-low loss photonic waveguides in visible spectrum. Some research activities are on-going based on this argument [28,154].

In Chapter 3, the fabrication processes for III-N materials were developed. The process adopted e-beam lithography, and the etching of III-N materials relies on Cl_2, BCl_3, and Ar chemistries. Due to the large bonding energy of AlN, the optimal etching bias is ~250 V, while for GaN the optimal bias is ~150 V.

Chapter 4 evaluates the performance of III-N optical waveguide. Theoretical calculation suggests that the free carrier loss is dominated in GaN based waveguide due to its n-type conductivity, while the AlN waveguide exhibit excellent wave guiding performance. High quality factor on order of 10^5 of AlN based micro ring resonator has been achieved, while the Q factor of GaN based micro-disk resonators are on order of 10^4,

this is consistent with the numerical calculations. Moreover, a semi-analytical model is developed for the purpose of threading dislocation induced scattering loss estimation. TM modes exhibit larger scattering loss due to the constructive interference in the far field, while the TE mode exhibit lower loss.

Chapter 5 explores the nonlinear optical applications, specifically on the supercontinuum generation from soliton dynamics. The soliton within high order modes can be utilized for dispersive generation in the visible spectrum, which has the potential for on-chip frequency metrologies.

6.2 Future works

Several future topics can be potentially pursued. First, the nonlinear refractive index and two photon absorption coefficient of AlN in the UV-visible spectrum is still largely unknown, the theoretical calculations rely on the estimation as introduced in Chapter 2. The Z-scan measurement on AlN would be meaningful to the community.

The demonstration of high quality factor UV resonator has attracted increasing research efforts [26,27]. AlN exhibits intrinsic Q factor on order of 10^5 in the UV spectrum [27], lower propagation loss is achieved by Al_2O_3 waveguides [26]. It's worth noting that the β-Ga_2O_3 can be a very strong candidate for high performance UV resonators due to its excellent crystalline quality. The current investigations mainly employs the sputtered β-Ga_2O_3 [154] or MOCVD grown β-Ga_2O_3 on foreign substrate [28]. Those materials are still defectious and far from real single crystalline. Huge potential improvement can be expected if bulk β-Ga_2O_3 can be used. It's also noteworthy that the β-Ga_2O_3 possesses close lattice constant with InGaN lasers. High quality GaN grown on β-Ga_2O_3 has also

been demonstrated [155]. The β-Ga_2O_3 would potentially be an ideal material platform with excellent active integration capabilities in visible spectrum.

Although the β-Ga_2O_3 exhibits promising features for ultra-low loss waveguides in UV-visible spectrum, the weak confinement hindered its further implementation in the nonlinear optical applications, where the AlN would still play an important role. For better waveguiding performance of AlN, the fabrication process has to be improved. The ICP process has a large space for improvement since the sidewall angle is ~70˚. The line-edge roughness can also be further reduced by applied other EBL resists. The polishing process adopted within this research is largely manual, which limited the yield and need to be improved.

The imperfect crystalline quality of GaN hindered its applications when guiding the ultra-fast femtosecond pulses, however, the relative large two photon absorption coefficient can be utilized for on-chip auto-correlators as shown in Fig. 6-1. The pulse is split into two parts and encountered at the center of probing region. The large intensity when two pulse meets causes strong two photon absorption coefficient. By probing the current distribution in space, the temporal profile of pulse can be reconstructed.

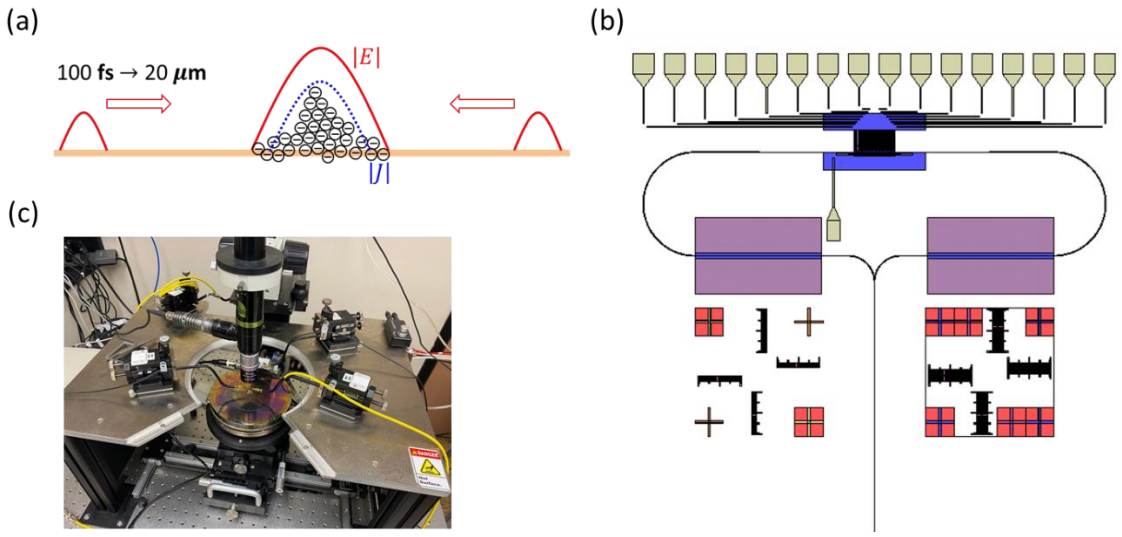

Figure 6-1. The schematic of on-chip auto-correlator. (a) The working principle. (b) Layout (c) The testing setup in ASU.

The system level active integration of GaN lasers, detectors and AlN waveguides can also be potentially explored for the neurophotonics, spectrometers, beam steering devices, on-chip fully integrated entangled photon generators, etc. The active integration relies on regrowth [156] or wafer bonding techniques [157] thus required advanced III-N growth techniques.

REFERENCES

[1] Pimputkar, S., Speck, J.S., DenBaars, S.P. and Nakamura, S., 2009. Prospects for LED lighting. Nature photonics, 3(4), pp.180-182.

[2] Zhao, Y., Tanaka, S., Pan, C.C., Fujito, K., Feezell, D., Speck, J.S., DenBaars, S.P. and Nakamura, S., 2011. High-power blue-violet semipolar (2021) InGaN/GaN light-emitting diodes with low efficiency droop at 200 A/cm2. Applied physics express, 4(8), p.082104.

[3] Mishra, U.K., Shen, L., Kazior, T.E. and Wu, Y.F., 2008. GaN-based RF power devices and amplifiers. Proceedings of the IEEE, 96(2), pp.287-305.

[4] Takagi, S., Enya, Y., Kyono, T., Adachi, M., Yoshizumi, Y., Sumitomo, T., Yamanaka, Y., Kumano, T., Tokuyama, S., Sumiyoshi, K. and Saga, N., 2012. High-power (over 100 mW) green laser diodes on semipolar {2021} GaN substrates operating at wavelengths beyond 530 nm. Applied Physics Express, 5(8), p.082102.

[5] Rigutti, L., Tchernycheva, M., De Luna Bugallo, A., Jacopin, G., Julien, F.H., Zagonel, L.F., March, K., Stephan, O., Kociak, M. and Songmuang, R., 2010. Ultraviolet photodetector based on GaN/AlN quantum disks in a single nanowire. Nano letters, 10(8), pp.2939-2943.

[6] Nakamura, S., 2009. Current status of GaN-based solid-state lighting. MRS bulletin, 34(2), pp.101-107.

[7] Kuzmík, J., 2001. Power electronics on InAlN/(In) GaN: Prospect for a record performance. IEEE Electron Device Letters, 22(11), pp.510-512.

[8] Lu, Z., Tian, P., Chen, H., Baranowski, I., Fu, H., Huang, X., Montes, J., Fan, Y., Wang, H., Liu, X. and Liu, R., 2017. Active tracking system for visible light communication using a GaN-based micro-LED and NRZ-OOK. Optics express, 25(15), pp.17971-17981.

[9] Huang, X., Li, W., Fu, H., Li, D., Zhang, C., Chen, H., Fang, Y., Fu, K., DenBaars, S.P., Nakamura, S. and Goodnick, S.M., 2019. High-Temperature Polarization-Free III-Nitride Solar Cells with Self-Cooling Effects. ACS Photonics, 6(8), pp.2096-2103.

[10] Aharonovich, I., Castelletto, S., Simpson, D.A., Su, C.H., Greentree, A.D. and Prawer, S., 2011. Diamond-based single-photon emitters. Reports on progress in Physics, 74(7), p.076501.

[11] Schroder, T., Schell, A.W., Kewes, G., Aichele, T. and Benson, O., 2011. Fiber-integrated diamond-based single photon source. Nano letters, 11(1), pp.198-202.

[12] Aguilar, J.A., Albert, A., Amram, P., Anghinolfi, M., Anton, G., Anvar, S., Ardellier-Desages, F.E., Aslanides, E., Aubert, J.J., Azoulay, R. and Bailey, D., 2005. Transmission of light in deep sea water at the site of the ANTARES neutrino telescope. Astroparticle Physics, 23(1), pp.131-155.

[13] Segev, E., Reimer, J., Moreaux, L.C., Fowler, T.M., Chi, D., Sacher, W.D., Lo, M., Deisseroth, K., Tolias, A.S., Faraon, A. and Roukes, M.L., 2016. Patterned photostimulation via visible-wavelength photonic probes for deep brain optogenetics. Neurophotonics, 4(1), p.011002.

[14] Schubert, E.F., Gessmann, T. and Kim, J.K., 2000. Light emitting diodes. Kirk-Othmer Encyclopedia of Chemical Technology.

[15] Silveira, E., Freitas, J.A., Schujman, S.B. and Schowalter, L.J., 2008. AlN bandgap temperature dependence from its optical properties. Journal of crystal growth, 310(17), pp.4007-4010.

[16] Hanada, T., 2009. Basic properties of ZnO, GaN, and related materials. In Oxide and nitride semiconductors (pp. 1-19). Springer, Berlin, Heidelberg.

[17] Im, K.S., Ha, J.B., Kim, K.W., Lee, J.S., Kim, D.S., Hahm, S.H. and Lee, J.H., 2010. Normally off GaN MOSFET based on AlGaN/GaN heterostructure with extremely high 2DEG density grown on silicon substrate. IEEE Electron Device Letters, 31(3), pp.192-194.

[18] Ritt, G., Cennini, G., Geckeler, C. and Weitz, M., 2004. Laser frequency offset locking using a side of filter technique. Applied Physics B, 79(3), pp.363-365.

[19] Friederich, F., Schuricht, G., Deninger, A., Lison, F., Spickermann, G., Bolívar, P.H. and Roskos, H.G., 2010. Phase-locking of the beat signal of two distributed-feedback diode lasers to oscillators working in the MHz to THz range. Optics express, 18(8), pp.8621-8629.

[20] Muneeb, M., Vasiliev, A., Ruocco, A., Malik, A., Chen, H., Nedeljkovic, M., Penades, J.S., Cerutti, L., Rodriguez, J.B., Mashanovich, G.Z. and Smit, M.K.,

2016. III-V-on-silicon integrated micro-spectrometer for the 3 μm wavelength range. Optics express, 24(9), pp.9465-9472.

[21] Stern, B., Ji, X., Dutt, A. and Lipson, M., 2017. Compact narrow-linewidth integrated laser based on a low-loss silicon nitride ring resonator. Optics letters, 42(21), pp.4541-4544.

[22] Xu, Q., Schmidt, B., Pradhan, S. and Lipson, M., 2005. Micrometre-scale silicon electro-optic modulator. nature, 435(7040), pp.325-327.

[23] Pfeifle, J., Brasch, V., Lauermann, M., Yu, Y., Wegner, D., Herr, T., Hartinger, K., Schindler, P., Li, J., Hillerkuss, D. and Schmogrow, R., 2014. Coherent terabit communications with microresonator Kerr frequency combs. Nature photonics, 8(5), pp.375-380.

[24] Reimer, C., Kues, M., Roztocki, P., Wetzel, B., Grazioso, F., Little, B.E., Chu, S.T., Johnston, T., Bromberg, Y., Caspani, L. and Moss, D.J., 2016. Generation of multiphoton entangled quantum states by means of integrated frequency combs. Science, 351(6278), pp.1176-1180.

[25] Sacher, W.D., Luo, X., Yang, Y., Chen, F.D., Lordello, T., Mak, J.C., Liu, X., Hu, T., Xue, T., Lo, P.G.Q. and Roukes, M.L., 2019. Visible-light silicon nitride waveguide devices and implantable neurophotonic probes on thinned 200 mm silicon wafers. Optics Express, 27(26), pp.37400-37418.

[26] Aslan, M.M., Webster, N.A., Byard, C.L., Pereira, M.B., Hayes, C.M., Wiederkehr, R.S. and Mendes, S.B., 2010. Low-loss optical waveguides for the near ultra-violet and visible spectral regions with Al2O3 thin films from atomic layer deposition. Thin Solid Films, 518(17), pp.4935-4940.

[27] Liu, X., Bruch, A.W., Gong, Z., Lu, J., Surya, J.B., Zhang, L., Wang, J., Yan, J. and Tang, H.X., 2018. Ultra-high-Q UV microring resonators based on a single-crystalline AlN platform. Optica, 5(10), pp.1279-1282.

[28] Zhou, J., Chen, H., Fu, H., Fu, K., Deng, X., Huang, X., Yang, T.H., Montes, J.A., Yang, C., Qi, X. and Zhang, B., 2019. Demonstration of low loss β-Ga2O3 optical waveguides in the UV–NIR spectra. Applied Physics Letters, 115(25), p.251108.

[29] Neutens, P., Rutowska, M., Van Roy, W., Jansen, R., Buja, F. and Van Dorpe, P., 2018. Mitigation of UV-Induced Propagation Loss in PECVD Silicon Nitride Photonic Waveguides. ACS Photonics, 5(6), pp.2145-2150.

[30] Xiong, C., Pernice, W., Ryu, K.K., Schuck, C., Fong, K.Y., Palacios, T. and Tang, H.X., 2011. Integrated GaN photonic circuits on silicon (100) for second harmonic generation. Optics express, 19(11), pp.10462-10470.

[31] Pernice, W.H.P., Xiong, C., Schuck, C. and Tang, H.X., 2012. Second harmonic generation in phase matched aluminum nitride waveguides and micro-ring resonators. Applied Physics Letters, 100(22), p.223501.

[32] Jung, H., Stoll, R., Guo, X., Fischer, D. and Tang, H.X., 2014. Green, red, and IR frequency comb line generation from single IR pump in AlN microring resonator. Optica, 1(6), pp.396-399.

[33] Miller, S., Luke, K., Okawachi, Y., Cardenas, J., Gaeta, A.L. and Lipson, M., 2014. On-chip frequency comb generation at visible wavelengths via simultaneous second-and third-order optical nonlinearities. Optics Express, 22(22), pp.26517-26525.

[34] Singh, N., Xin, M., Vermeulen, D., Shtyrkova, K., Li, N., Callahan, P.T., Magden, E.S., Ruocco, A., Fahrenkopf, N., Baiocco, C. and Kuo, B.P., 2018. Octave-spanning coherent supercontinuum generation in silicon on insulator from 1.06 μm to beyond 2.4 μm. Light: Science & Applications, 7(1), pp.17131-17131.

[35] Guo, H., Herkommer, C., Billat, A., Grassani, D., Zhang, C., Pfeiffer, M.H., Weng, W., Brès, C.S. and Kippenberg, T.J., 2018. Mid-infrared frequency comb via coherent dispersive wave generation in silicon nitride nanophotonic waveguides. Nature Photonics, 12(6), pp.330-335.

[36] Oh, D.Y., Yang, K.Y., Fredrick, C., Ycas, G., Diddams, S.A. and Vahala, K.J., 2017. Coherent ultra-violet to near-infrared generation in silica ridge waveguides. Nature communications, 8(1), pp.1-7.

[37] Liu, X., Bruch, A.W., Lu, J., Gong, Z., Surya, J.B., Zhang, L., Wang, J., Yan, J. and Tang, H.X., 2019. Beyond 100 THz-spanning ultraviolet frequency combs in a non-centrosymmetric crystalline waveguide. Nature communications, 10(1), pp.1-8.

[38] Chen, H., Huang, X., Fu, H., Lu, Z., Zhang, X., Montes, J.A. and Zhao, Y., 2017. Characterizations of nonlinear optical properties on GaN crystals in polar, nonpolar, and semipolar orientations. Applied Physics Letters, 110(18), p.181110.

[39] Chen, H., Fu, H., Huang, X., Montes, J.A., Yang, T.H., Baranowski, I. and Zhao, Y., 2018. Characterizations of the nonlinear optical properties for (010) and (2^{-}01) beta-phase gallium oxide. Optics express, 26(4), pp.3938-3946.

[40] Chen, H., Fu, H., Huang, X., Zhang, X., Yang, T.H., Montes, J.A., Baranowski, I. and Zhao, Y., 2017. Low loss GaN waveguides at the visible spectral wavelengths for integrated photonics applications. Optics express, 25(25), pp.31758-31773.

[41] Chen, H., Fu, H., Zhou, J., Huang, X., Yang, T.H., Fu, K., Yang, C., Montes, J.A. and Zhao, Y., 2019. Study of crystalline defect induced optical scattering loss inside photonic waveguides in UV–visible spectral wavelengths using volume current method. Optics express, 27(12), pp.17262-17273.

[42] Chen, H., Zhou, J., Li, D., Chen, D., Vinod, A.K., Fu, H., Huang, X., Yang, T.H., Montes, J.A., Fu, K. and Yang, C., 2019. On-chip directional octave-spanning supercontinuum generation from high order mode in near ultraviolet to infrared spectrum using AlN waveguides. arXiv preprint arXiv:1908.04719.

[43] Griffith, A.G., Lau, R.K., Cardenas, J., Okawachi, Y., Mohanty, A., Fain, R., Lee, Y.H.D., Yu, M., Phare, C.T., Poitras, C.B. and Gaeta, A.L., 2015. Silicon-chip mid-infrared frequency comb generation. Nature communications, 6, p.6299.

[44] Zhang, L., Yan, Y., Yue, Y., Lin, Q., Painter, O., Beausoleil, R.G. and Willner, A.E., 2011. On-chip two-octave supercontinuum generation by enhancing self-steepening of optical pulses. Optics express, 19(12), pp.11584-11590.

[45] Sheik-Bahae, M., Said, A.A., Wei, T.H., Hagan, D.J. and Van Stryland, E.W., 1990. Sensitive measurement of optical nonlinearities using a single beam. IEEE journal of quantum electronics, 26(4), pp.760-769.

[46] Gu, B., Fan, Y.X., Chen, J., Wang, H.T., He, J. and Ji, W., 2007. Z-scan theory of two-photon absorption saturation and experimental evidence. Journal of Applied Physics, 102(8), p.083101.

[47] Wang, J., Gu, B., Ni, X.W. and Wang, H.T., 2012. Z-scan theory with simultaneous two-and three-photon absorption saturation. Optics & Laser Technology, 44(2), pp.390-393.

[48] Sheik-Bahae, M., Hutchings, D.C., Hagan, D.J. and Van Stryland, E.W., 1991. Dispersion of bound electron nonlinear refraction in solids. IEEE Journal of quantum electronics, 27(6), pp.1296-1309.

[49] Soltani, M., Soref, R., Palacios, T. and Englund, D., 2016. AlGaN/AlN integrated photonics platform for the ultraviolet and visible spectral range. Optics express, 24(22), pp.25415-25423.

[50] Sun, C.K., Liang, J.C., Wang, J.C., Kao, F.J., Keller, S., Mack, M.P., Mishra, U. and DenBaars, S.P., 2000. Two-photon absorption study of GaN. Applied Physics Letters, 76(4), pp.439-441.

[51] Pačebutas, V., Stalnionis, A., Krotkus, A., Suski, T., Perlin, P. and Leszczynski, M., 2001. Picosecond Z-scan measurements on bulk GaN crystals. Applied Physics Letters, 78(26), pp.4118-4120.

[52] Petit, S., Guennani, D., Gilliot, P., Hirlimann, C., Hönerlage, B., Briot, O. and Aulombard, R.L., 1997. Luminescence and absorption of GaN films under high excitation. Materials Science and Engineering: B, 43(1-3), pp.196-200.

[53] Fang, Y., Xiao, Z., Wu, X., Zhou, F., Yang, J., Yang, Y. and Song, Y., 2015. Optical nonlinearities and ultrafast all-optical switching of m-plane GaN in the near-infrared. Applied Physics Letters, 106(25), p.251903.

[54] Funato, M., Ueda, M., Kawakami, Y., Narukawa, Y., Kosugi, T., Takahashi, M. and Mukai, T., 2006. Blue, green, and amber InGaN/GaN light-emitting diodes on semipolar {11-22} GaN bulk substrates. Japanese Journal of Applied Physics, 45(7L), p.L659.

[55] Tsai, C.Y., Tsai, C.Y., Chen, C.H., Sung, T.L., Wu, T.Y. and Shih, F.P., 1998. Theoretical model for intravalley and intervalley free-carrier absorption in semiconductor lasers: Beyond the classical Drude model. IEEE journal of quantum electronics, 34(3), pp.552-559.

[56] Huang, Y.L., Sun, C.K., Liang, J.C., Keller, S., Mack, M.P., Mishra, U.K. and DenBaars, S.P., 1999. Femtosecond Z-scan measurement of GaN. Applied physics letters, 75(22), pp.3524-3526.

[57] Martínez, A., Blasco, J., Sanchis, P., Galán, J.V., García-Rupérez, J., Jordana, E., Gautier, P., Lebour, Y., Hernández, S., Spano, R. and Guider, R., 2010. Ultrafast all-optical switching in a silicon-nanocrystal-based silicon slot waveguide at telecom wavelengths. Nano letters, 10(4), pp.1506-1511.

[58] Stepanov, S., Nikolaev, V., Bougrov, V. and Romanov, A., 2016. Gallium OXIDE: Properties and applica 498 a review. Rev. Adv. Mater. Sci, 44, pp.63-86.

[59] Wuu, D.S., Ou, S.L., Horng, R.H., Ravadgar, P., Wang, T.Y. and Lee, H.Y., 2012, February. Growth and characterization of Ga2O3 on sapphire substrates for UV sensor applications. In Oxide-based Materials and Devices III (Vol. 8263, p. 826317). International Society for Optics and Photonics.

[60] Limb, J.B., Yoo, D., Ryou, J.H., Lee, W., Shen, S.C., Dupuis, R.D., Reed, M.L., Collins, C.J., Wraback, M., Hanser, D. and Preble, E., 2006. GaN ultraviolet avalanche photodiodes with optical gain greater than 1000 grown on GaN substrates by metal-organic chemical vapor deposition. Applied physics letters, 89(1), p.011112.

[61] Janowitz, C., Scherer, V., Mohamed, M., Krapf, A., Dwelk, H., Manzke, R., Galazka, Z., Uecker, R., Irmscher, K., Fornari, R. and Michling, M., 2011. Experimental electronic structure of In2O3 and Ga2O3. New Journal of Physics, 13(8), p.085014.

[62] Galazka, Z., Irmscher, K., Uecker, R., Bertram, R., Pietsch, M., Kwasniewski, A., Naumann, M., Schulz, T., Schewski, R., Klimm, D. and Bickermann, M., 2014. On the bulk β-Ga2O3 single crystals grown by the Czochralski method. Journal of Crystal Growth, 404, pp.184-191.

[63] Bhaumik, I., Bhatt, R., Ganesamoorthy, S., Saxena, A., Karnal, A.K., Gupta, P.K., Sinha, A.K. and Deb, S.K., 2011. Temperature-dependent index of refraction of monoclinic Ga 2 O 3 single crystal. Applied optics, 50(31), pp.6006-6010.

[64] He, H., Orlando, R., Blanco, M.A., Pandey, R., Amzallag, E., Baraille, I. and Rérat, M., 2006. First-principles study of the structural, electronic, and optical properties of Ga 2 O 3 in its monoclinic and hexagonal phases. Physical Review B, 74(19), p.195123.

[65] Guo, Z., Verma, A., Wu, X., Sun, F., Hickman, A., Masui, T., Kuramata, A., Higashiwaki, M., Jena, D. and Luo, T., 2015. Anisotropic thermal conductivity in single crystal β-gallium oxide. Applied Physics Letters, 106(11), p.111909.

[66] Yariv, A., 2002. Critical coupling and its control in optical waveguide-ring resonator systems. IEEE Photonics Technology Letters, 14(4), pp.483-485.

[67] Koynov, K., Mitev, P., Buchvarov, I. and Saltiel, S., 1996. Calculation of third-order non-linear optical susceptibility of metal-oxide crystals. Pure and Applied Optics: Journal of the European Optical Society Part A, 5(1), p.89.

[68] Zhao, M., Xu, C.H., Hu, W.J., Wang, W.J., Guo, L.W. and Chen, X.L., 2016. Observation of two-photon absorption and nonlinear refraction in AlN. Chinese Physics Letters, 33(10), p.104201.

[69] Jung, H., Xiong, C., Fong, K.Y., Zhang, X. and Tang, H.X., 2013. Optical frequency comb generation from aluminum nitride microring resonator. Optics letters, 38(15), pp.2810-2813.

[70] Song, J., Lu, W., Flynn, J.S. and Brandes, G.R., 2005. AlGaN/GaN Schottky diode hydrogen sensor performance at high temperatures with different catalytic metals. Solid-state electronics, 49(8), pp.1330-1334.

[71] Li, W., Ji, D., Tanaka, R., Mandal, S., Laurent, M. and Chowdhury, S., 2017. Demonstration of GaN static induction transistor (SIT) using self-aligned process. IEEE Journal of the Electron Devices Society, 5(6), pp.485-490.

[72] Talwar, D.N., Sofranko, D., Mooney, C. and Tallo, S., 2002. Elastic, structural, bonding, and defect properties of zinc-blende BN, AlN, GaN, InN and their alloys. Materials Science and Engineering: B, 90(3), pp.269-277.

[73] McPeak, K.M., Jayanti, S.V., Kress, S.J., Meyer, S., Iotti, S., Rossinelli, A. and Norris, D.J., 2015. Plasmonic films can easily be better: rules and recipes. ACS photonics, 2(3), pp.326-333.

[74] Busch, K., Lölkes, S., Wehrspohn, R.B. and Föll, H. eds., 2006. Photonic crystals: advances in design, fabrication, and characterization. John Wiley & Sons.

[75] Liu, A., Liao, L., Rubin, D., Nguyen, H., Ciftcioglu, B., Chetrit, Y., Izhaky, N. and Paniccia, M., 2007. High-speed optical modulation based on carrier depletion in a silicon waveguide. Optics Express, 15(2), pp.660-668.

[76] Green, W.M., Rooks, M.J., Sekaric, L. and Vlasov, Y.A., 2007. Ultra-compact, low RF power, 10 Gb/s silicon Mach-Zehnder modulator. Optics express, 15(25), pp.17106-17113.

[77] Long, D.A. and Long, D.A., 1977. Raman spectroscopy (Vol. 276). New York: McGraw-Hill.

[78] Doylend, J.K., Heck, M.J.R., Bovington, J.T., Peters, J.D., Coldren, L.A. and Bowers, J.E., 2011. Two-dimensional free-space beam steering with an optical phased array on silicon-on-insulator. Optics express, 19(22), pp.21595-21604.

[79] Soref, R.I.C.H.A.R.D.A. and Bennett, B.R.I.A.N.R., 1987. Electrooptical effects in silicon. IEEE journal of quantum electronics, 23(1), pp.123-129.

[80] Chen, H., Fu, H., Lu, Z., Huang, X. and Zhao, Y., 2016. Optical properties of highly polarized InGaN light-emitting diodes modified by plasmonic metallic grating. Optics express, 24(10), pp.A856-A867.

[81] Ciminelli, C., Passaro, V.M., Dell'Olio, F. and Armenise, M.N., 2009. Three-dimensional modelling of scattering loss in InGaAsP/InP and silica-on-silicon bent waveguides. Journal of the European Optical Society-Rapid publications, 4.

[82] Keller, S., Parish, G., Fini, P.T., Heikman, S., Chen, C.H., Zhang, N., DenBaars, S.P., Mishra, U.K. and Wu, Y.F., 1999. Metalorganic chemical vapor deposition of high mobility AlGaN/GaN heterostructures. Journal of applied physics, 86(10), pp.5850-5857.

[83] Shul, R.J., McClellan, G.B., Casalnuovo, S.A., Rieger, D.J., Pearton, S.J., Constantine, C., Barratt, C., Karlicek Jr, R.F., Tran, C. and Schurman, M., 1996. Inductively coupled plasma etching of GaN. Applied physics letters, 69(8), pp.1119-1121.

[84] Lacey, J.P.R. and Payne, F.P., 1990. Radiation loss from planar waveguides with random wall imperfections. IEE Proceedings J-Optoelectronics, 137(4), pp.282-288.

[85] Poulton, C.G., Koos, C., Fujii, M., Pfrang, A., Schimmel, T., Leuthold, J. and Freude, W., 2006. Radiation modes and roughness loss in high index-contrast waveguides. IEEE Journal of selected topics in quantum electronics, 12(6), pp.1306-1321.

[86] Barwicz, T. and Haus, H.A., 2005. Three-dimensional analysis of scattering losses due to sidewall roughness in microphotonic waveguides. Journal of Lightwave Technology, 23(9), p.2719.

[87] Gupta, C., Enatsu, Y., Gupta, G., Keller, S. and Mishra, U.K., 2016. High breakdown voltage p–n diodes on GaN on sapphire by MOCVD. physica status solidi (a), 213(4), pp.878-882.

[88] Kelly, M.K., Vaudo, R.P., Phanse, V.M., Görgens, L., Ambacher, O. and Stutzmann, M., 1999. Large free-standing GaN substrates by hydride vapor phase epitaxy and laser-induced liftoff. Japanese journal of applied physics, 38(3A), p.L217.

[89] Funato, M., Ueda, M., Kawakami, Y., Narukawa, Y., Kosugi, T., Takahashi, M. and Mukai, T., 2006. Blue, green, and amber InGaN/GaN light-emitting diodes on semipolar {11-22} GaN bulk substrates. Japanese Journal of Applied Physics, 45(7L), p.L659.

[90] K. Misiakos, D. and Tsamakis, “Accurate measurements of the silicon intrinsic carrier density from 78 to 340 K,” J. Appl. Phys. 74(5), 3293-3297 (1993).

[91] S.M. Sze, and K.K. Ng, “Physics of semiconductor devices.” John wiley & sons (2006).

[92] K. Kainosho, H. Shimakura, H. Yamamoto, and O. Oda, “Undoped semi-insulating InP by high-pressure annealing,” Appl. Phys. Lett. 59(8), pp.932-934 (1991).

[93] Malyk, O., 2012. Charge carrier mobility in gallium nitride. Diamond and related materials, 23, pp.23-27.

[94] Levinshtein, M.E., Rumyantsev, S.L. and Shur, M.S. eds., 2001. Properties of Advanced Semiconductor Materials: GaN, AIN, InN, BN, SiC, SiGe. John Wiley & Sons.

[95] Liu, G., Yan, C., Zhou, G., Wen, J., Qin, Z., Zhou, Q., Li, B., Zheng, R., Wu, H. and Sun, Z., 2018. Broadband white-light emission from alumina nitride bulk single crystals. ACS Photonics, 5(10), pp.4009-4013.

[96] Hui, R., Taherion, S., Wan, Y., Li, J., Jin, S.X., Lin, J.Y. and Jiang, H.X., 2003. GaN-based waveguide devices for long-wavelength optical communications. Applied physics letters, 82(9), pp.1326-1328.

[97] Stolz, A., Cho, E., Dogheche, E., Androussi, Y., Troadec, D., Pavlidis, D. and Decoster, D., 2011. Optical waveguide loss minimized into gallium nitride based structures grown by metal organic vapor phase epitaxy. Applied Physics Letters, 98(16), p.161903.

[98] Sekiya, T., Sasaki, T. and Hane, K., 2015. Design, fabrication, and optical characteristics of freestanding GaN waveguides on silicon substrate. Journal of Vacuum Science & Technology B, Nanotechnology and Microelectronics: Materials, Processing, Measurement, and Phenomena, 33(3), p.031207.

[99] Li, W., Luo, Y., Xiong, B., Sun, C., Wang, L., Wang, J., Han, Y., Yan, J., Wei, T. and Lu, H., 2015. Fabrication of GaN-based ridge waveguides with very smooth and vertical sidewalls by combined plasma dry etching and wet chemical etching. physica status solidi (a), 212(10), pp.2341-2344.

[100] Bruch, A.W., Xiong, C., Leung, B., Poot, M., Han, J. and Tang, H.X., 2015. Broadband nanophotonic waveguides and resonators based on epitaxial GaN thin films. Applied Physics Letters, 107(14), p.141113.

[101] Geiss, R., Chowdhury, A., Staus, C.M., Ng, H.M., Park, S.S. and Han, J.Y., 2005. Low loss GaN at 1550 nm. Applied Physics Letters, 87(13), p.132107.

[102] Gromovyi, M., Semond, F., Duboz, J.Y., Feullet, G. and de Micheli, M., 2014. Low loss GaN waveguides for visible light on Si substrates.

[103] Bauters, J.F., Heck, M.J., John, D., Dai, D., Tien, M.C., Barton, J.S., Leinse, A., Heideman, R.G., Blumenthal, D.J. and Bowers, J.E., 2011. Ultra-low-loss high-aspect-ratio Si 3 N 4 waveguides. Optics express, 19(4), pp.3163-3174.

[104] Pearton, S.J., Shul, R.J. and Ren, F., 2000. A review of dry etching of GaN and related materials. Materials Research Society Internet Journal of Nitride Semiconductor Research, 5(1).

[105] Mills, D.L., 1980. Light scattering by point defects in insulating crystals. Journal of Applied Physics, 51(11), pp.5864-5867.

[106] Stegmaier, M., Ebert, J., Meckbach, J.M., Ilin, K., Siegel, M. and Pernice, W.H.P., 2014. Aluminum nitride nanophotonic circuits operating at ultraviolet wavelengths. Applied Physics Letters, 104(9), p.091108.

[107] Tokumoto, Y., Amma, S.I., Shibata, N., Mizoguchi, T., Edagawa, K., Yamamoto, T. and Ikuhara, Y., 2009. Fabrication of electrically conductive nanowires using high-density dislocations in AlN thin films. Journal of Applied Physics, 106(12), p.124307.

[108] Huang, X., Fu, H., Chen, H., Lu, Z., Baranowski, I., Montes, J., Yang, T.H., Gunning, B.P., Koleske, D. and Zhao, Y., 2017. Reliability analysis of InGaN/GaN multi-quantum-well solar cells under thermal stress. Applied Physics Letters, 111(23), p.233511.

[109] H. Fu, I. Baranowski, X. Huang, H. Chen, Z. Lu, J. Montes, X. Zhang, and Y. Zhao, "Demonstration of AlN Schottky barrier diodes with blocking voltage over 1 Kv," IEEE Electron Device Lett. 38(9), 1286-1289 (2017).

[110] Kaganer, V.M. and Sabelfeld, K.K., 2010. X-ray diffraction peaks from correlated dislocations: Monte Carlo study of dislocation screening. Acta Crystallographica Section A: Foundations of Crystallography, 66(6), pp.703-716.

[111] Kopp, V.S., Kaganer, V.M., Baidakova, M.V., Lundin, W.V., Nikolaev, A.E., Verkhovtceva, E.V., Yagovkina, M.A. and Cherkashin, N., 2014. X-ray determination of threading dislocation densities in GaN/Al2O3 (0001) films grown by metalorganic vapor phase epitaxy. Journal of Applied Physics, 115(7), p.073507.

[112] Constantine, A.B., 2005. Antenna theory: analysis and design. Wiley-Interscience.

[113] Majkić, A., Franke, A., Kirste, R., Schlesser, R., Collazo, R., Sitar, Z. and Zgonik, M., 2017. Optical nonlinear and electro-optical coefficients in bulk aluminium nitride single crystals. physica status solidi (b), 254(9), p.1700077.

[114] Guo, X., Zou, C.L., Schuck, C., Jung, H., Cheng, R. and Tang, H.X., 2017. Parametric down-conversion photon-pair source on a nanophotonic chip. Light: Science & Applications, 6(5), pp.e16249-e16249.

[115] Thapa, S.B., Kirchner, C., Scholz, F., Prinz, G.M., Thonke, K., Sauer, R., Chuvilin, A., Biskupek, J., Kaiser, U. and Hofstetter, D., 2007. Structural and spectroscopic properties of AlN layers grown by MOVPE. Journal of crystal growth, 298, pp.383-386.

[116] Miyake, H., Lin, C.H., Tokoro, K. and Hiramatsu, K., 2016. Preparation of high-quality AlN on sapphire by high-temperature face-to-face annealing. Journal of Crystal Growth, 456, pp.155-159.

[117] Levy, J.S., Gondarenko, A., Foster, M.A., Turner-Foster, A.C., Gaeta, A.L. and Lipson, M., 2010. CMOS-compatible multiple-wavelength oscillator for on-chip optical interconnects. Nature photonics, 4(1), pp.37-40.

[118] Jung, H. and Tang, H.X., 2016. Aluminum nitride as nonlinear optical material for on-chip frequency comb generation and frequency conversion. Nanophotonics, 5(2), pp.263-271.

[119] Liu, X., Sun, C., Xiong, B., Wang, L., Wang, J., Han, Y., Hao, Z., Li, H., Luo, Y., Yan, J. and Wei, T., 2018. Integrated high-Q crystalline AlN microresonators for broadband Kerr and Raman frequency combs. ACS Photonics, 5(5), pp.1943-1950.

[120] Neugebauer, J. and Van de Walle, C.G., 1994. Atomic geometry and electronic structure of native defects in GaN. Physical Review B, 50(11), p.8067.

[121] Ogino, T. and Aoki, M., 1980. Mechanism of yellow luminescence in GaN. Japanese Journal of Applied Physics, 19(12), p.2395.

[122] Gupta, C., Enatsu, Y., Gupta, G., Keller, S. and Mishra, U.K., 2016. High breakdown voltage p–n diodes on GaN on sapphire by MOCVD. physica status solidi (a), 213(4), pp.878-882.

[123] Lu, T.J., Fanto, M., Choi, H., Thomas, P., Steidle, J., Mouradian, S., Kong, W., Zhu, D., Moon, H., Berggren, K. and Kim, J., 2018. Aluminum nitride integrated

photonics platform for the ultraviolet to visible spectrum. Optics express, 26(9), pp.11147-11160.

[124] Yang, J., Hugonin, J.P. and Lalanne, P., 2016. Near-to-far field transformations for radiative and guided waves. ACS photonics, 3(3), pp.395-402.

[125] Pastrňák, J. and Roskovcová, L., 1966. Refraction index measurements on AlN single crystals. physica status solidi (b), 14(1), pp.K5-K8.

[126] Demiryont, H., Thompson, L.R. and Collins, G.J., 1986. Optical properties of aluminum oxynitrides deposited by laser-assisted CVD. Applied optics, 25(8), pp.1311-1318.

[127] Panda, P., Ramaseshan, R., Sundari, S.T. and Suematsu, H., 2018. Anisotropic optical properties of a-axis AlN films: a spectroscopic ellipsometry study. OSA Continuum, 1(4), pp.1241-1250.

[128] Agrawal, G.P., 2000. Nonlinear fiber optics. In Nonlinear Science at the Dawn of the 21st Century (pp. 195-211). Springer, Berlin, Heidelberg.

[129] Hult, J., 2007. A fourth-order Runge–Kutta in the interaction picture method for simulating supercontinuum generation in optical fibers. Journal of Lightwave Technology, 25(12), pp.3770-3775.

[130] Schawlow, A.L. and Townes, C.H., 1958. Infrared and optical masers. Physical Review, 112(6), p.1940.

[131] Maiman, T.H., 1960. Stimulated optical radiation in ruby. nature, 187(4736), pp.493-494.

[132] Fan, F., Turkdogan, S., Liu, Z.C., Shelhammer, D. and Ning, C.Z., 2015. A monolithic white laser Nat. Nanotechnology, 10.

[133] Rosemann, N.W., Eußner, J.P., Beyer, A., Koch, S.W., Volz, K., Dehnen, S. and Chatterjee, S., 2016. A highly efficient directional molecular white-light emitter driven by a continuous-wave laser diode. Science, 352(6291), pp.1301-1304.

[134] Udem, T., Holzwarth, R. and Hänsch, T.W., 2002. Optical frequency metrology. Nature, 416(6877), pp.233-237.

[135] Rosenband, T., Hume, D.B., Schmidt, P.O., Chou, C.W., Brusch, A., Lorini, L., Oskay, W.H., Drullinger, R.E., Fortier, T.M., Stalnaker, J.E. and Diddams, S.A.,

2008. Frequency ratio of Al+ and Hg+ single-ion optical clocks; metrology at the 17th decimal place. Science, 319(5871), pp.1808-1812.

[136] H. Tu, S. A. Boppart, Coherent fiber supercontinuum for biophotonics. Laser Photonics Rev. 7, 628-645 (2013).

[137] Humbert, G., Wadsworth, W.J., Leon-Saval, S.G., Knight, J.C., Birks, T.A., Russell, P.S.J., Lederer, M.J., Kopf, D., Wiesauer, K., Breuer, E.I. and Stifter, D., 2006. Supercontinuum generation system for optical coherence tomography based on tapered photonic crystal fibre. Optics express, 14(4), pp.1596-1603.

[138] Fallahkhair, A.B., Li, K.S. and Murphy, T.E., 2008. Vector finite difference modesolver for anisotropic dielectric waveguides. Journal of Lightwave Technology, 26(11), pp.1423-1431.

[139] Ji, X., Barbosa, F.A., Roberts, S.P., Dutt, A., Cardenas, J., Okawachi, Y., Bryant, A., Gaeta, A.L. and Lipson, M., 2017. Ultra-low-loss on-chip resonators with sub-milliwatt parametric oscillation threshold. Optica, 4(6), pp.619-624.

[140] Watanabe, N., Kimoto, T. and Suda, J., 2012. Thermo-optic coefficients of 4H-SiC, GaN, and AlN for ultraviolet to infrared regions up to 500° C. Japanese Journal of Applied Physics, 51(11R), p.112101.

[141] Ciret, C., Gorza, S.P., Husko, C., Roelkens, G., Kuyken, B. and Leo, F., 2018. Physical origin of higher-order soliton fission in nanophotonic semiconductor waveguides. Scientific reports, 8(1), pp.1-11.

[142] Foster, M.A., Dudley, J.M., Kibler, B., Cao, Q., Lee, D., Trebino, R. and Gaeta, A.L., 2005. Nonlinear pulse propagation and supercontinuum generation in photonic nanowires: experiment and simulation. Applied Physics B, 81(2-3), pp.363-367.

[143] Kibler, B., Dudley, J.M. and Coen, S., 2005. Supercontinuum generation and nonlinear pulse propagation in photonic crystal fiber: influence of the frequency-dependent effective mode area. Applied Physics B, 81(2-3), pp.337-342.

[144] Yang, Q.F., Yi, X., Yang, K.Y. and Vahala, K., 2016. Spatial-mode-interaction-induced dispersive waves and their active tuning in microresonators. Optica, 3(10), pp.1132-1135.

[145] D. D. Hickstein, H. Jung, D. R. Carlson, A. Lind, I. Coddington, K. Srinivasan, G. G. Ycas, D. C. Cole, A. Kowligy, C. Fredrick, S. Droste, Ultrabroadband

supercontinuum generation and frequency-comb stabilization using on-chip waveguides with both cubic and quadratic nonlinearities. Phys. Rev. Appl. 8, 014025 (2017).

[146] Dudley, J.M. and Coen, S., 2002. Numerical simulations and coherence properties of supercontinuum generation in photonic crystal and tapered optical fibers. IEEE Journal of selected topics in quantum electronics, 8(3), pp.651-659.

[147] DS, S.R., Engelsholm, R.D., Gonzalo, I.B., Zhou, B., Bowen, P., Moselund, P.M., Bang, O. and Bache, M., 2019. Ultra-low-noise supercontinuum generation with a flat near-zero normal dispersion fiber. Optics letters, 44(9), pp.2216-2219.

[148] Gonzalo, I.B., Engelsholm, R.D., Sørensen, M.P. and Bang, O., 2018. Polarization noise places severe constraints on coherence of all-normal dispersion femtosecond supercontinuum generation. Scientific reports, 8(1), pp.1-13.

[149] Rigler, M., Buh, J., Hoffmann, M.P., Kirste, R., Bobea, M., Mita, S., Gerhold, M.D., Collazo, R., Sitar, Z. and Zgonik, M., 2015. Optical characterization of Al-and N-polar AlN waveguides for integrated optics. Applied Physics Express, 8(4), p.042603.

[150] Hickstein, D.D., Kerber, G.C., Carlson, D.R., Chang, L., Westly, D., Srinivasan, K., Kowligy, A., Bowers, J.E., Diddams, S.A. and Papp, S.B., 2018. Quasi-phase-matched supercontinuum generation in photonic waveguides. Physical review letters, 120(5), p.053903.

[151] Miller, G.D., Batchko, R.G., Tulloch, W.M., Weise, D.R., Fejer, M.M. and Byer, R.L., 1997. 42%-efficient single-pass cw second-harmonic generation in periodically poled lithium niobate. Optics letters, 22(24), pp.1834-1836.

[152] Chowdhury, A., Ng, H.M., Bhardwaj, M. and Weimann, N.G., 2003. Second-harmonic generation in periodically poled GaN. Applied physics letters, 83(6), pp.1077-1079.

[153] Alden, D., Troha, T., Kirste, R., Mita, S., Guo, Q., Hoffmann, A., Zgonik, M., Collazo, R. and Sitar, Z., 2019. Quasi-phase-matched second harmonic generation of UV light using AlN waveguides. Applied Physics Letters, 114(10), p.103504.

[154] Tan, S., Deng, H., Urbanek, K.E., Miao, Y., Zhao, Z., Harris, J.S. and Byer, R.L., 2020. Low-loss GaO x-core/SiO 2-cladding planar waveguides on Si substrate. Optics Express, 28(8), pp.12475-12486.

[155] Awan, K.M., Muhammad, M.M., Sivan, M., Bonca, S., Roqan, I.S. and Dolgaleva, K., 2018. Fabrication and optical characterization of GaN waveguides on (− 201)-oriented β-Ga 2 O 3. Optical Materials Express, 8(1), pp.88-96.

[156] Fu, K., Fu, H., Huang, X., Yang, T.H., Cheng, C.Y., Peri, P.R., Chen, H., Montes, J., Yang, C., Zhou, J. and Deng, X., 2020. Reverse Leakage Analysis for As-Grown and Regrown Vertical GaN-on-GaN Schottky Barrier Diodes. IEEE Journal of the Electron Devices Society, 8, pp.74-83.

[157] Wuu, D.S., Hsu, S.C., Huang, S.H., Wu, C.C., Lee, C.E. and Horng, R.H., 2004. GaN/mirror/Si light-emitting diodes for vertical current injection by laser lift-off and wafer bonding techniques. Japanese journal of applied physics, 43(8R), p.5239.

APPENDIX A

EXAMPLE OF CODES FOR THE CALCULATION OF SCATTERING LOSS

In this section the codes used for scattering loss simulation are provides. Only the basic version is provided for better illustration purpose. One can easily modify the codes and reproduce the results shown in Chapter 4. The codes is Matlab based. Since the code would cost a very large number of pages to print, all functions are packaged and can be downloaded from the following link, only the most important notes when using the codes are attached here: https://github.com/hchen170/Waveguide-sidewall-scattering-loss-evaluation-in-3D.

It should be pointed out that the mode solver is based on other researcher's FDM solver, the reference link is provided in README file. The code can only run correctly when the FDM solver is correctly referred.

"README" file:

Run "loss_in_dB.m" to compute sidewall scattering (can also be used for defect scattering). Other ".m" files are functions that needed.

Computing the sidewall scattering loss of photonic waveguides using volume current method. Most importantly, to run this code on matlab, you should download a FDM solver from: https://www.photonics.umd.edu/software/wgmodes/

Credit & Citation for the FDM solver:

Fallahkhair, Arman B., Kai S. Li, and Thomas E. Murphy. "Vector finite difference modesolver for anisotropic dielectric waveguides." Journal of Lightwave Technology 26.11 (2008): 1423-1431.

We will call several functions from "wgmodes": wgmodes.m, postprocess.m, contourmode.m

Alternatively, you can use your own FDM or FEM solver to compute the mode profile.

The obtained mode profile serves as the input for dyadic Green's function

Some other useful references are:

1. Chen, Hong, et al. "Study of crystalline defect induced optical scattering loss inside photonic waveguides in UV–visible spectral wavelengths using volume current method." Optics Express 27.12 (2019): 17262-17273.
2. Bauters, Jared F., et al. "Ultra-low-loss high-aspect-ratio Si 3 N 4 waveguides." Optics express 19.4 (2011): 3163-3174.
3. Barwicz, Tymon, and Hermann A. Haus. "Three-dimensional analysis of scattering losses due to sidewall roughness in microphotonic waveguides." Journal of Lightwave Technology 23.9 (2005): 2719.

The code is simplified for the purpose of better interpretation, alternatively, one can use it to compute scattering loss from threading dislocations as well, simply by removing some commented lines.

Running the code, you will obtain several plots:

Figure 1: Mode profile (Ex, Ey, Ez)

Figure 2: "Volume current" at the sidewall, whose radiation is resonsible for the scattering loss

Figure 3: Distributaion of Poynting vector in the far field in polar plot. Coordinate is defined in Ref. 1

The n_{eff} indicates the effective index for the computed mode.

APPENDIX B

EXAMPLE OF CODE USED FOR THE NUMERICAL SIMULATION ON NONLINEAR SHRODINGER'S EUQATION

In this section we provide the codes used for NSE simulation. Only the basic version is provided for the purpose of easy interpretation. One can easily modify the codes and reproduce any NSE simulated plots obtained within this work. The code is Matlab based.

“README” file:

Solving nonlinear Schrodinger's equation using split step Fourier method with 4th order R-K. This solver considered 2 to 6 orders of dispersions, Kerr effects, self-steepening, loss, and Raman effect. The code took AlN waveguide pumped near 800 nm with a series of 100 fs pulse as an example. Dispersion is anomalous near 800 nm.

All parameters are straight forward and physical.

NSE codes (basic version):

```
% The algorithm includes Runge-Kutta method in its fourth order.
% Self-steepening and Raman scattering are involved, by giving proper
% estimation of Tr and taus

%---Specify input parameters
clear all; %
distance = 0.006; % in meter
loss_dB = -0; % in dB/cm
P_r=10^(loss_dB/10);
loss = -log(P_r)*100/2;
beta2 = -70*10^(-27); % in s2/m
beta3 = 3.6*10^(-40); % in s3/m, note that delta3=beta3/(6*beta2*T0)
beta4 = -11*10^(-56); % in s4/m
%beta5 = -0.3*10^(-69);
%beta6 = 4.1*10^(-84);
```

```
beta5=0;
beta6=0;


Aeff=0.96;
lambda=810*10^(-9);
gamma = 2*pi*23*10^(-20)/(lambda*Aeff*10^(-12)) % in 1/(w*m), this is the typical value in optical fiber
chirp0 = 0; % input pulse chirp (default value)
T0 = 100*10^(-15); % pulse width
V0=1/T0;
P0=3000; %in wat
N=sqrt(abs(gamma*P0*T0*T0/beta2/1.665/1.665))
Ld=abs(T0*T0/beta2)/1.665/1.665
Lnl=1/(gamma*P0)
L_fission=Ld/N
dleta_w=0.86*1/(T0/1.665)*gamma*P0*distance
f=3*10^(8)/lambda;
omega0=f*2*pi;
c=3*10^(8);
Tr=0*10^(-15);
taus=1/omega0;
%---set simulation parameters
nt = 256*2048/2; Tmax = 2*128*T0/2; % FFT points and window size
step_num = 4096/4; % No. of z steps
deltaz = distance/step_num; % step size in z
dtau = (2*Tmax)/nt; % step size in tau
%---Specify outer loop simulation paramters
nout=100;
dz=round(step_num/nout);
outer_count=1;
Map_t=zeros(nout-1,nt);
Map_f=zeros(nout-1,nt);
```

```
%---tau and omega arrays
tau = (-nt/2:nt/2-1)*dtau; % temporal grid
omega = (pi/Tmax) * [(0:nt/2-1) (-nt/2:-1)]; % frequency grid
%---Input Field profile
uu = sqrt(P0)*exp(-1.39*(tau/T0).^2); %Gaussian shape
%---Plot input pulse shape and spectrum
temp = fftshift(ifft(uu)).*(nt*dtau)/sqrt(2*pi); % spectrum
figure; subplot(2,1,1);
plot (tau, abs(uu).^2, '--k'); hold on;
axis([-20*T0 20*T0 0 inf]);
xlabel('Time');
ylabel('Power');
title('Input and Output Pulse Shape and Spectrum');
subplot(2,1,2);
plot (c./(fftshift(omega)/(2*pi)+f)*10^(6), 10*log10(abs(temp).^2)-
max(10*log10(abs(temp).^2)), '--k'); hold on;
axis([0.3,1.2 -40 5]);
%subplot(2,1,2);
%plot ((fftshift(omega)/(2*pi)+f)*10^(-12), 10*log10(abs(temp).^2)-
max(10*log10(abs(temp).^2)), '--k'); hold on;
%axis([300,500 -30 5]);
xlabel('Frequency');
ylabel('Spectral Power');
%---Store dispersive phase shifts to speedup code
dispersion = exp(-
0.5*loss*deltaz/2+0.5i*beta2*omega.^2*deltaz/2+1i*beta3/6*omega.^3*deltaz/2+1i*bet
a4/24*omega.^4*deltaz/2+1i*beta5/120*omega.^5*deltaz/2+1i*beta6/720*omega.^6*del
taz/2); % 1/2 phase factor
%hhz = 1i*gamma*deltaz/2; % 1/2 nonlinear phase factor
% ********* [ Beginning of MAIN Loop] **********
% scheme: 4th order RK method
for n=1:step_num
ui=fft(ifft(uu).*dispersion);
```

```
%==========================================================================
diff1=1j*gamma*taus*gradient(abs(uu).^2.*uu)/dtau;
diff2=-gamma*Tr*uu.*gradient(abs(uu).^2)/dtau;
k1=1j*fft(ifft(gamma*abs(uu).*abs(uu).*uu+diff1+diff2).*dispersion);
%==========================================================================
uk2=ui+deltaz/2*k1;
diff3=1j*gamma*taus*gradient(abs(uk2).^2.*uk2)/dtau;
diff4=-gamma*Tr*uk2.*gradient(abs(uk2).^2)/dtau;
k2=1j*(gamma*abs(uk2).^2.*(uk2)+diff3+diff4);
%==========================================================================
uk3=ui+deltaz/2*k2;
diff5=1j*gamma*taus*gradient(abs(uk3).^2.*uk3)/dtau;
diff6=-gamma*Tr*uk3.*gradient(abs(uk3).^2)/dtau;
k3=1j*(gamma*abs(uk3).^2.*(uk3)+diff5+diff6);
%==========================================================================
uk4=fft(ifft(ui+deltaz*k3).*dispersion);
diff7=1j*gamma*taus*gradient(abs(uk4).^2.*uk4)/dtau;
diff8=-gamma*Tr*uk4.*gradient(abs(uk4).^2)/dtau;
k4=1j*(gamma*abs(uk4).^2.*(uk4)+diff7+diff8);
%==========================================================================
uu=fft(ifft(ui+k1*deltaz/6+k2*deltaz/3+k3*deltaz/3).*dispersion)+k4*deltaz/6;
temp = fftshift(ifft(uu)).* (nt*dtau)/sqrt(2*pi);
if n==outer_count*dz
   Map_t(outer_count,:)=abs(uu).^2;
   Map_f(outer_count,:)=10*log10(abs(temp).^2)-max(10*log10(abs(temp).^2));
   %Map_f(outer_count,:)=temp;
   outer_count=outer_count+1;
end
```

```
end
temp = fftshift(ifft(uu)).* (nt*dtau)/sqrt(2*pi); % Final spectrum
% *************** [ End of MAIN Loop ] **************
%----Plot output pulse shape and spectrum
subplot(2,1,1)
plot (tau, abs(uu).^2, '-k')
subplot(2,1,2)
plot(c./(fftshift(omega)/(2*pi)+f)*10^(6), 10*log10(abs(temp).^2)-
max(10*log10(abs(temp).^2)), '-k')
%plot(c./(fftshift(omega)/(2*pi)+f)*10^(6), 10*log10(abs(temp).^2), '-k')
%subplot(2,1,2)
%plot((fftshift(omega)/(2*pi)+f)*10^(-12), 10*log10(abs(temp).^2)-
max(10*log10(abs(temp).^2)), '-k')
output=10*log10(abs(temp).^2)-max(10*log10(abs(temp).^2));
output=output';
output_x=c./(fftshift(omega)/(2*pi)+f)*10^(6);
output_x=output_x';
%----Image Plot
hbar=1.055*10^(-34);
q=1.6*10^(-19);
shift_omega=fftshift(omega);
figure;
image([shift_omega(1)*hbar/q+1.24/(lambda*10^(6)),shift_omega(size(shift_omega))*h
bar/q+1.24/(lambda*10^(6))],[distance,0],Map_f,'CDataMapping','scaled')
caxis([-40 0])
xlim([1,3])
figure;
image([-nt/2*dtau,(nt/2-1)*dtau],[0,distance],Map_t,'CDataMapping','scaled')
xlim([-20*T0,20*T0])
caxis([0,3000])
```